**Defense Threat Reduction Agency**
**8725 John J. Kingman Road, MS**
**6201 Fort Belvoir, VA 22060-6201**

**TECHNICAL REPORT**

# Integrated Modeling and Experimental Studies at the Meso-Scale for Advanced Reactive Materials

July 2016

D. Scott Stewart et al.

Prepared by:
University of Illinois
1206 West Green Street
Urbana, IL 61801

# REPORT DOCUMENTATION PAGE

| 1. REPORT DATE (DD-MM-YYYY) | 2. REPORT TYPE | 3. DATES COVERED (From - To) |
|---|---|---|
| 00-07-2016 | Final Technical Report | 6-15-2010 to 10-01-2015 |

**4. TITLE AND SUBTITLE**
Integrated Modeling and Experimental Studies at the Meso-Scale for Advanced Reactive Materials

**5a. CONTRACT NUMBER**

**5b. GRANT NUMBER**
HDTRA1-10-1-0020

**5c. PROGRAM ELEMENT NUMBER**

**6. AUTHOR(S)**
D. Scott Stewart (PI)
Nick Glumac (Co-PI)
John B. Bdzil (Co-PI)
Joseph C. Foster (Co-PI)

**5d. PROJECT NUMBER**

**5e. TASK NUMBER**

**5f. WORK UNIT NUMBER**

**7. PERFORMING ORGANIZATION NAME(S) AND ADDRESS(ES)**
University of Illinois
1206 West Green Street
Urbana, IL 61801

**8. PERFORMING ORGANIZATION REPORT NUMBER**

**9. SPONSORING/MONITORING AGENCY NAME(S) AND ADDRESS(ES)**
Defense Threat Reduction Agency
8725 John J. Kingman Road
Fort Belvoir, VA 22060-6201

**10. SPONSOR/MONITOR'S ACRONYM(S)**
DTRA

**11. SPONSOR/MONITOR'S REPORT NUMBER(S)**
DTRA-TR-16-76

**12. DISTRIBUTION/AVAILABILITY STATEMENT**
Distribution Statement A. Approved for public release; distribution is unlimited.

**13. SUPPLEMENTARY NOTES**

**14. ABSTRACT**
The modeling and simulation work in this grant was directed by Prof. D. Scott Stewart, (the Stewart-Group) and the experimental work and data collection was directed by Prof. Nick Glumac (the Glumac-group). Professors Stewart and Glumac and Drs. John Bdzil and Joseph C. Foster, collaborated on experimental designs, that benefited from the concurrent theoretical and computational modeling. The effort described in this report, fully integrated modeling and experiments to study the energy release processes that thermitic and/or exothermic intermetallic reactive materials experience when they are subjected to sustained shock loading.

**15. SUBJECT TERMS**
shock; meso-scale;thermitic; exothermic

| 16. SECURITY CLASSIFICATION OF: | | | 17. LIMITATION OF ABSTRACT | 18. NUMBER OF PAGES | 19a. NAME OF RESPONSIBLE PERSON |
|---|---|---|---|---|---|
| a. REPORT | b. ABSTRACT | c. THIS PAGE | | | Allen Dalton |
| U | U | U | SAR | 60 | 19b. TELEPHONE NUMBER (Include area code) 703-767-4663 |

# UNIT CONVERSION TABLE
## U.S. customary units to and from international units of measurement[*]

| U.S. Customary Units | Multiply by → | Divide by† ← | International Units |
|---|---|---|---|
| **Length/Area/Volume** | | | |
| inch (in) | 2.54 | $\times 10^{-2}$ | meter (m) |
| foot (ft) | 3.048 | $\times 10^{-1}$ | meter (m) |
| yard (yd) | 9.144 | $\times 10^{-1}$ | meter (m) |
| mile (mi, international) | 1.609 344 | $\times 10^{3}$ | meter (m) |
| mile (nmi, nautical, U.S.) | 1.852 | $\times 10^{3}$ | meter (m) |
| barn (b) | 1 | $\times 10^{-28}$ | square meter ($m^2$) |
| gallon (gal, U.S. liquid) | 3.785 412 | $\times 10^{-3}$ | cubic meter ($m^3$) |
| cubic foot ($ft^3$) | 2.831 685 | $\times 10^{-2}$ | cubic meter ($m^3$) |
| **Mass/Density** | | | |
| pound (lb) | 4.535 924 | $\times 10^{-1}$ | kilogram (kg) |
| unified atomic mass unit (amu) | 1.660 539 | $\times 10^{-27}$ | kilogram (kg) |
| pound-mass per cubic foot (lb $ft^{-3}$) | 1.601 846 | $\times 10^{1}$ | kilogram per cubic meter (kg $m^{-3}$) |
| pound-force (lbf avoirdupois) | 4.448 222 | | newton (N) |
| **Energy/Work/Power** | | | |
| electron volt (eV) | 1.602 177 | $\times 10^{-19}$ | joule (J) |
| erg | 1 | $\times 10^{-7}$ | joule (J) |
| kiloton (kt) (TNT equivalent) | 4.184 | $\times 10^{12}$ | joule (J) |
| British thermal unit (Btu) (thermochemical) | 1.054 350 | $\times 10^{3}$ | joule (J) |
| foot-pound-force (ft lbf) | 1.355 818 | | joule (J) |
| calorie (cal) (thermochemical) | 4.184 | | joule (J) |
| **Pressure** | | | |
| atmosphere (atm) | 1.013 250 | $\times 10^{5}$ | pascal (Pa) |
| pound force per square inch (psi) | 6.984 757 | $\times 10^{3}$ | pascal (Pa) |
| **Temperature** | | | |
| degree Fahrenheit ($^{o}F$) | $[T(^{o}F) - 32]/1.8$ | | degree Celsius ($^{o}C$) |
| degree Fahrenheit ($^{o}F$) | $[T(^{o}F) + 459.67]/1.8$ | | kelvin (K) |
| **Radiation** | | | |
| curie (Ci) [activity of radionuclides] | 3.7 | $\times 10^{10}$ | per second ($s^{-1}$) [becquerel (Bq)] |
| roentgen (R) [air exposure] | 2.579 760 | $\times 10^{-4}$ | coulomb per kilogram (C $kg^{-1}$) |
| rad [absorbed dose] | 1 | $\times 10^{-2}$ | joule per kilogram (J $kg^{-1}$) [gray (Gy)] |
| rem [equivalent and effective dose] | 1 | $\times 10^{-2}$ | joule per kilogram (J $kg^{-1}$) [sievert (Sv)] |

[*]Specific details regarding the implementation of SI units may be viewed at http://www.bipm.org/en/si/.

†Multiply the U.S. customary unit by the factor to get the international unit. Divide the international unit by the factor to get the U.S. customary unit.

2015-11-16

## Abstract

The modeling and simulation work in this grant was directed by Prof. D. Scott Stewart, (the Stewart-Group) and the experimental work and data collection was directed by Prof. Nick Glumac (the Glumac-group). Professors Stewart and Glumac and Drs. John Bdzil and Joseph C. Foster, collaborated on experimental designs, that benefited from the concurrent theoretical and computational modeling. The effort described in this report fully integrated modeling and experiments to study the energy release processes that thermitic and/or exothermic intermetallic reactive materials experience when they are subjected to sustained shock loading.

# Table of Contents

## I. Objectives

An objective of this grant was to integrate modeling and experiments to develop an increased scientific understanding of the condensed phase energy release processes in the microstructure, that thermitic and/or exothermic intermetallic materials experience when they are subjected to sustained shock loading. Data from highly spatially and temporally resolved experiments, supported by our modeling and simulation efforts were directed at building and validating a model that describes the basic physical processes, including solid state, multi-phase transport and reaction/diffusion mechanisms. Such experimentally validated models are invaluable for the design of the intended applications. Our efforts provided a unique, multi-disciplinary research experience for graduate students and young scientists affiliated with and supported by this effort.

### *I.1 Background*

The Department of Defense (DoD) and the Defense Threat Reduction Agency (DTRA) has had a long- standing interests in designing reactive material (RM) whose energy release is triggered by shock/shear stimulus and which contributes to long duration, high-thermal pulse. A main application of thermitic reactive materials is the defeat of biological agents that must be destroyed with an extremely high temperature deflagration, that is highly contained in localized area. There is a need to avoid wide-scale dispersal of the biological threat agent and thermal destruction is a preferred mechanism. Materials that lie in a group of intermetallic, and thermitic mixtures are promising because when the unreacted (solid) materials are combined to make products materials, they often have very high (enthalpic) energy release and often make make mainly solid products so that gas generation is somewhat minimized. Our original proposal identified a number of target systems of interest that included, the Titanium-Boron system (metal/intermetallic), the aluminum copper oxide, (metal/metal oxide) system as well as a number of similar combinations with metal/metal oxide/intermetallic components.

## II. Approach

In design applications, the RM's are typically manufactured composites, layered or particulate, and the reactants are not molecularly pre-mixed. Therefore a distinct microstructure comprised of regions of separated reactants, is inherited from the constituents and fabrication. Reaction of the initial constituents must take place at interfaces between molecularly pure materials. The initial shock passage serves as a trigger that concentrates energy by collapse/compaction and yield of nominally solid materials, that surely experience temperature rise through dissipative yield mechanisms. But immediately and subsequently the overall stress level drops to near ambient conditions of the larger surroundings, while high temperature remain in localized regions at the interfaces between materials,  The post-shock energy release that is related to chemical reaction is

controlled entirely by anerobic, condensed phase processes in the RM. The project scope was based on a scenario from application, where a shock is driven into RM by a high explosive, and the subsequent reaction/combustion of the materials is observed and modeled. Below Figure 6. from the original proposal provides an excellent conceptual schematic of this effort
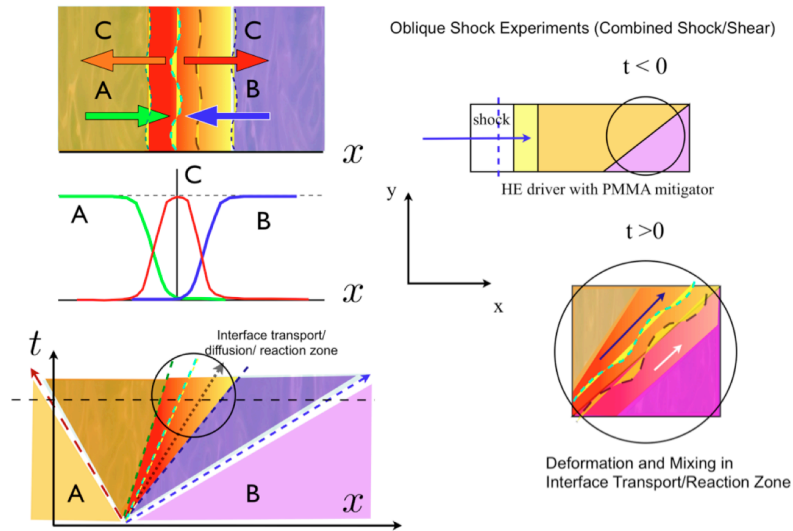


**Figure 6.** A schematic depiction of the normal shock loading and shear loading experiments described in Subsection A) and B), respectively. The bottom of the figure shows a sequence in an x,t-space, with two reactant materials A and B subjected to a driving shock that passes through material A and then transmits the shock into B, with a reflected shock traveling back through material A. If the materials are pure reactant constituents, then reaction first starts at the material interface. If the reaction A + B -> C proceeds and is sustained, then diffusion of A and B into the diffuse region of product C maintains the reaction near the interface. This simple diffusion-reaction model is a stand in for the more realistic thermite and intermetallic reactions.

**Figure. 1**. A reproduction of Fig. 6 from the original proposal that describes the basic scenario and premise.

At the time of the inception of this proposal (2009) even to the time of this summary report (2015), with a few exceptions that include work done by our combined groups, there have been few high-resolution experiments that attempt to resolve the energy release processes in the microstructure and few models of the condensed phase processes that are truly predictive. While experiments are limited by optical issues, modeling and simulation issues have been limited by the necessary requirements to simultaneously model deformation, reaction and diffusion in condensed materials. Our efforts focused on exactly these issues.

Two major sets of accomplishments were made during our efforts. 1) On the experimental side, the Glumac group executed a set of experiments, [25] on shock compaction of RM that was able to visualize the characters of ignition and propagation of reaction in thermite and intermetallic systems. 2) On the

experimental side, the Stewart-group was able to develop new models, (e.g. the Gibbs formulation [18]) that is fundamentally based on the concept of stress and temperature equilibrium at the smallest continuum scales at all points in materials mixtures. Hence stress and temperature are fundamental state variables, that define Gibbs potentials for the materials. This new approach allowed our group to develop new, material models for reaction and diffusion and deformation in condensed phase reactants. Both of these main accomplishments have been (or are currently being) documented in archival publications by the members of our combined group, [15,16,17,18,19,20,21,24] These upcoming and planned archival publications will cite DTRA support, [25,26,27,28]

What follows below is a brief overview description of the "Striker experiment" carried out in the Glumac lab, and a summary collection of the experimental results obtained so far. This is followed by a brief description of some of the key modeling and simulation results. These are the main achievements of this grant. A complete description of this work and its chronological development is found in Section VII, which is a concatenation of our annual reports.

## III. Synopis of Work Accomplished

### *III.1 Experimental Work*

The first experimental task was to define an representative experiment, that would capture key features of the ignition of a reactive material (RM) that was subjected to shock and rapid compression. Our entire team of senior investigators, experimentalists Glumac and Foster, and modelers Stewart and Bdzil, worked together to come up with a conceptual design we called the "Striker experiment". In this experiment a fabricated RM sample that was approximately a 3/8 inch cube, was inserted into a steel confinement cell. On either side, steel slider "striker bars" were inserted and tamped against the RM sample. Then on each striker bar, detonators (such as Reynolds RP-80 detonators) were placed on the striker bar in order to generate a shock wave and push the striker bars into the sample. A PMMA window for optical viewing was placed on one side of the confinement cell. On firing of the detonators, reactive events at the boundary of the RM and the viewing window were imaged in a 1 cm square view area by means of high magnification lenses, with very high speed cameras. Different classes of RM materials were subjected to this experiment. Figures 1 and 2 (this report) shows an overview of the experiment, the basic setup (circa 2012), and the imaging setup up for the second generation experiments.

# Overview of the Experiment
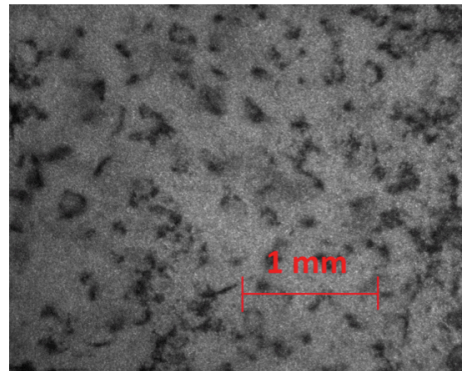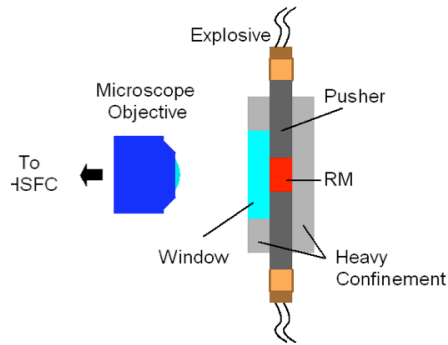


- Explosively driven pushers into RM sample. Watch with HSC,

- Can achieve grain scale spatial resolution and sub-us time resolution

**Figure 1.** Overview of the Striker experiment. Striker bars driven by detonators drive compression bars into the RM sample and direct imaging of burning events is made through an optical window.
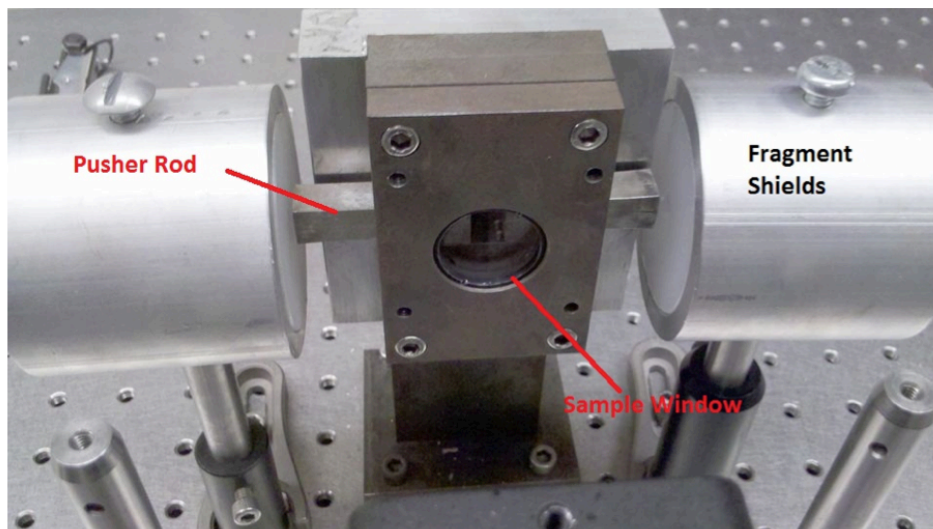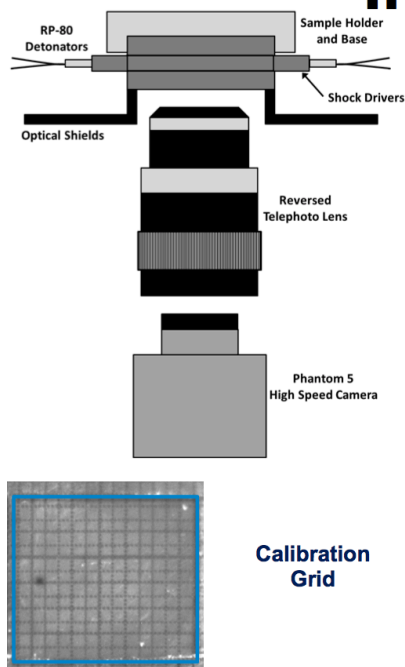
# Basic Setup



**Figure 2.** Basic set up of the Striker experiment. The detonators are embedded in fragments shields to prevent excessive damage to the confinement cell, that was used in multiple experiments.

# Experimental Methods: Imaging



- Reactive sample is imaged using 80-200 mm reversed telephoto lens

- Optical shields reduce intense emission from detonators

- Phantom camera records images at 10,000 or 19,000 fps

- Full sample and magnified field of view tested for each material

- Spatial calibration accomplished using calibration grid

**Figure 3.** Basic imaging set up of the Striker experiment. A reversed telephoto lense, with intensity filters and high-speed phantom camera were key features of the imaging system.

Tests were carried out on a suite of RMs that were manufactured in the Glumac-lab. The basic materials were made from mixtures of metal and metal oxide powders (such as aluminum and copper oxide) to make a thermite RM or a metal and intermetallic materials (such as titanium and silicon) to make a metal/intermetallic RM. These were combined and pressed to about 80 % of their theoretical maximum density. Titanium/Boron RMs were also tested but were found hard to ignite in the Striker experiement. However they were fired with mulitple detonators, in project funded by a grant funded supported by the Air Force Research Laboratory for bio-cidal experiments, [9,14].

Figures 4 and 5 show representative imaging results obtained from the Striker experiment, for a stoichiometric thermite mixture of aluminum and copper oxide.

# Results: Stoichiometric Al/CuO Thermite

- Imaging and video sequences show progression of the reaction
- Initial densification can be observed
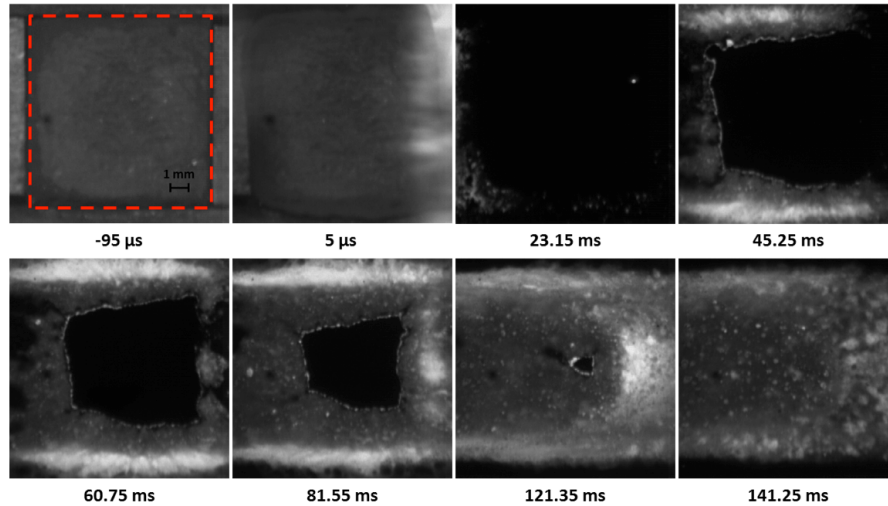- Propagation and flame speed can be examined



**Figure 4.** Images from the Al/CuO experiment, with a 80 % TMD, stoichiometric mixture.
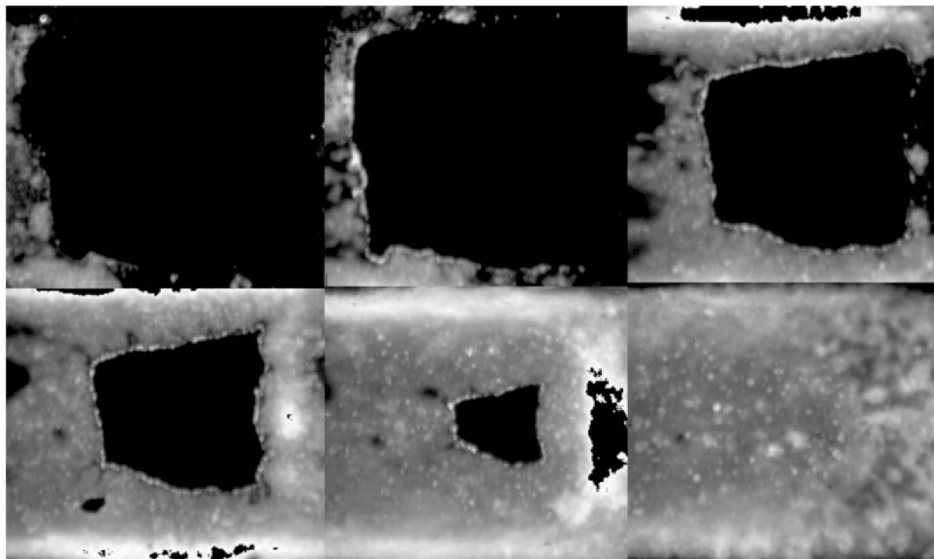


**Figure 5.** Close up images, for the same experiment shown in Fig 4., (with times not marked). Images show evidence of a front that follows compaction density contours, and secondary and tertiary reaction.

In addition to the Striker experiments shown above, another series of experiment that used a pure (fuzed) quartz, cylindrical confinement cell was used. This allowed greater optical access than the steel confinement cell. But the confinement was inadequate, when the same detonator and (cylindrical rod) striker bars were used. The confinment came apart prematurely. So this set of experiments while promising were only partly successful. This redesign was attractive from a modeling and simulation point of view. But a revised version of this experiment was not attempted.

### III.2 Modeling and Simulation Work

#### Simulations that Supported Experimental Design

The first efforts of our group were to provide basic support for the experiments in the Glumac lab. Simulation of the compaction events were carried out with the multimaterial hydrocode, ALE3D (distributed by Lawrence Livermore National Laboratory). Two and three dimensional simulations of shock/compaction event were carried out in representative experimental geometries in order to estimate timing and to evaluate the effects of mixing between particle during the compaction effects.

A major conclusions was that the effect of shock compaction is to increase the area where reaction can take place at the interfaces between the initially separated reactants. Also we found that one _must_ include material strength in the shock actuated mixing, since otherwise excessive reaction surface is created in the material simulations that is not physical.

Another major conclusion was that the light/dark boundaries observed in the Striker experiment follows contours of densification (compaction). The densification process is endothermic where mechanical energy is concentrated into small region of the microstructure and where mechanical dissipation there results in large amount of localized heating. The compaction process is realized by the propagation of a front and the observed light/dark front propagates in a sequenced manner that follows the compaction front. Hence we found significant evidence that burning takes place at the separated reactants boundaries, and that the ignition of the RM enabled by the compaction processes.

#### Development of a Multi-Component Reaction Diffusion Model Framework

One of the main tasks, outlined in the original proposal was to model multi-component reaction diffusion flames in condensed media. This led to an effort to identify thermodynamically consistent approaches and revisit the literature. Significant efforts were made based on earlier work of Stewart, and later revised to generate/invent what we now refer to as the Gibbs formulation, [18]. A single stress tensor, and a single temperature is assumed for the mixture with specified Gibbs potentials for all relevant species, and interaction energies. This work was of a fundamental nature, within non-equilibrium continuum thermodynamics.

The Gibbs formulation model enjoyed additional support through grants from the Office of Naval Research and the Air Force Office of Scientific Research.
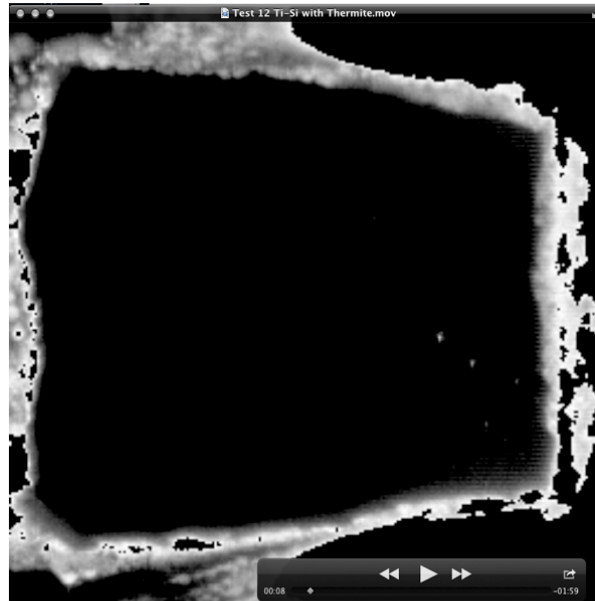


**Figure 7:** Shows a video frame from a stoichiometric Ti/Si experiment
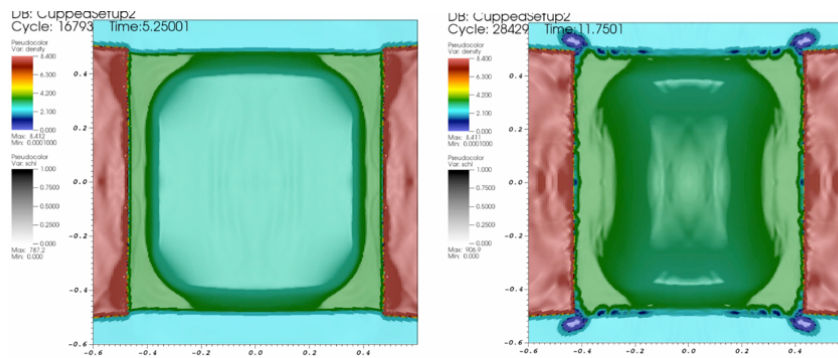


**Figure 8** Simulation results that show "square" shapes apparent in the color densification contours superimposed with a Schlieren image, of the Ti/B mixture simulations the shape of the initial compaction front contours and the shape of the flame front in the experiment.

**Figure 6.** Figures 7 and 8 extracted from the 2013 annual report that show a qualitative comparison of the  shape of the initial compaction  front contours from simulation and and the shape of  the flame front in the experiment.   This comparison strongly suggests that in the experiments, the lead reaction front propagates along the compaction front contours.

### Modeling Titanium Boron Condensed Phase Diffusion Flames

Because of interest in biocides, the original proposal discussed in detail the Titanium/Boron system. So our initial examples of reactive flow modeling considered Titanium/Boron as a representative (but significant) example. We note that subsequently we found in the experimental program that Ti/B RM mixtures were fairly hard to ignite and that systems like Al/CuO or Ti/Si were more reactive and thus provided lots of data in the Striker experiment setups. Nonetheless, we note another advantage of the choice of the Ti/B system for fundamental study, is that the basic overall reaction is simple with Ti + 2 B -> $TiB_2$. Thus only three components were needed for our earliest models and first treatments of condensed phase diffusion flames. A version of the Gibbs formulation was used that took advantage of a simplifying assumption that the components were fluid-like, and that a steady diffusion flame that situated itself in two opposed stream of separated reactants, was studied in detail and recently published [17].
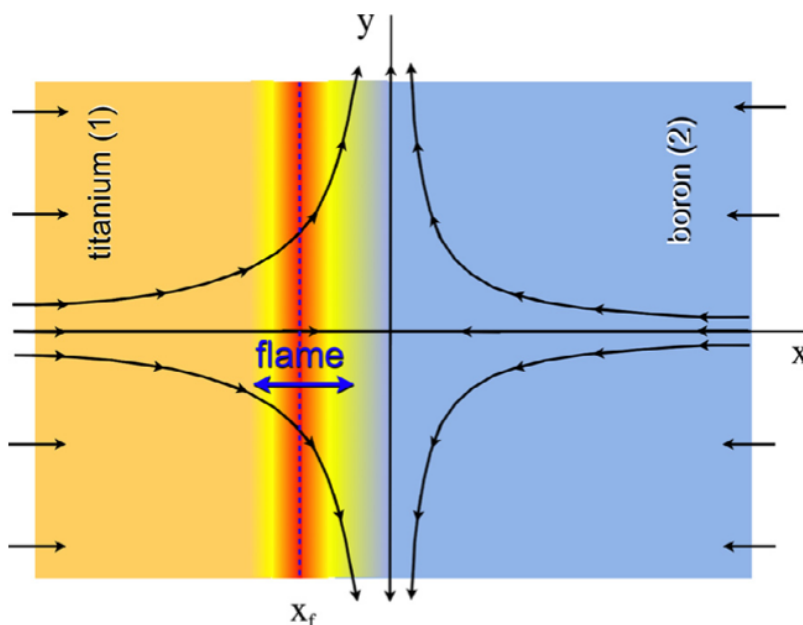


**Fig. 1.** Schematic of the condensed phase counterflow diffusion flame, with titanium entering from the left and boron from the right. The color shades clearly delineate the planar mixing region and reaction zone.

**Figure 7.** Figure 1 extracted from a recently published paper (in press), " Diffusion flames in condensed-phase energetic materials: Application to Titanium–Boron combustion", Combustion and Flame (2015) http://dx.doi.org/10.1016/j.combustflame.2015.08.023

## Modeling of the Ignition of an Aluminum Copper Oxide Thermite

The Glumac experiments on aluminum/copper oxide thermite showed ignition and extinction behavior. Evidence suggested that this takes place at the interface between the initially separated reactants.
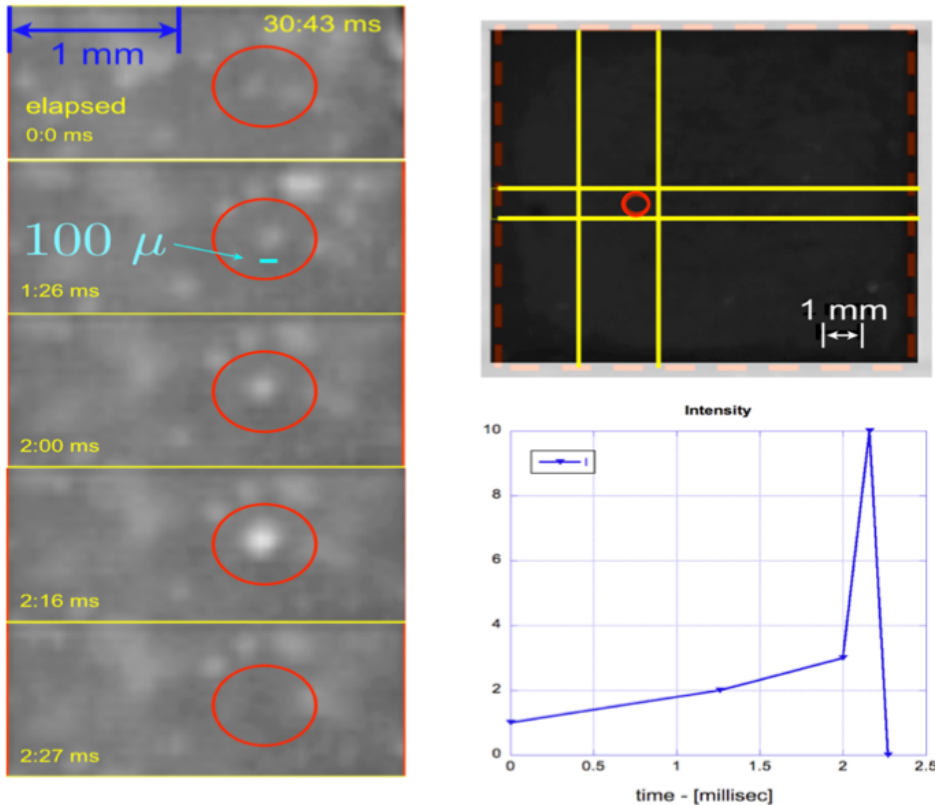


**FIGURE 1.** The entire domain from the viewing window (right-top) of the Glumac experiment. The cutout of image shows ignition/extinction event in the red circle(left), image intensity of bright spot(right-bottom)

**Figure 8.** Figure 1 extracted from a recent APS proceeding paper, that captures a sub-millisecond ignition/extintion event that takes place at the scale of the microstructure of the aluminum copper oxide thermite.

Efforts in the Stewart-group expanded the Gibbs formulation to model the features of ignition shown in Fig. 8. This modeling effort considered of the basic processes of a thermite, and included no less than eight components, and the melting of solid phases to liquid. This substantially expanded the analysis of multi-component diffusion. The component considered included, minimally Al-solid and liquid, CuO-solid and liquid, Cu-solid and liquid and $Al_2O_3$ -liquid and solid, [21,25,27].

## IV. Papers, Proceeding published, and Works in Progress

Here we provide a list of _all_ the papers, proceedings published, and works in progress of the Stewart-group and key publications of the Glumac-group, that were carried out during the execution of the grant. An astrick is used to mark papers that were principally funded by this DTRA grant. We note that both our groups have multiple ongoing efforts, funded by the Department of Defense and funding provided by DTRA is synergistics as it provides our larger efforts with a core base of funding. Hence we list all relevant publication of interest to DTRA that were generated in the time frame of this grant. Note the first years of the effort were devoted to _entirely new experiments and entirely new theory_, so that our DTRA cited publication appear in the later years of the grant and some are still in the process of being completed.

### Publications
(*- that cite DTRA Support)

### 2011

1. Yoo, S., D. Scott Stewart, D. E. Lambert, M. A. Lieber, and M. J. Szuck, "Modeling solid state detonation and reactive materials," ***Proceedings of the 14th International Detonation Symposium***, Office of Naval Research publication number 351-10-18, pp 211-218 (2011).

2. Bdzil, J. B., B. Lieberthal, and D. S. Stewart, "Mesoscale Modeling of Metal-loaded High Explosives," ***Proceedings of the 14th (International) Detonation Symposium***, Office of Naval Research publication number 351-10-18, pp. 1343-1352 (2011).

### 2012

3. Yoo, S., D. S. Stewart, S. Choi, and D. E. Lambert, "Modeling Kinetics for the Reaction of Aluminum and Teflon and the Simulation of Its Energetic Flow Motion," ***Proceedings of the Conference of the American Physical Society Topical Group on Shock Compression of Condensed Matter***, APS Conf. Proc. 1426, pp. 351-354 (2012).

4. Foster, J. C., N. Glumac, and D. S. Stewart, "Analysis of the Requirements on Modern Energetics and Their Impact on Materials Design," ***Proceedings of the Conference of the American Physical Society Topical Group on Shock Compression of Condensed Matter***, APS Conf. Proc. 1426, pp. 649-652 (2012).

5. Lieber, M., J. C. Foster Jr., and D. S. Stewart, A Study of Energy Partitioning Using A Set of Related Explosive Formulations,": ***Proceedings of the Conference of the American Physical Society Topical Group on Shock***

***Compression of Condensed Matter***, APS Conf. Proc. 1426, pp. 645-648 (2012).

6.  Stewart, D. S., M. Szuck, and L. E. Fried, "Detonation Theory for Condensed Phase Explosives with Anisotropic Properties," ***Proceedings of the Conference of the American Physical Society Topical Group on Shock Compression of Condensed Matter***, APS Conf. Proc. 1426, pp. 263-266 (2012).

7.  Saenz, J. A, B. D. Taylor, and D. S. Stewart, "Asymptotic Calculation of the Dynamics of Self-sustained Detonations in Condensed Phase Explosives," ***Journal of Fluid Mechanics***, Vol.710, pp 166-194 (2012).

8.  J. Bdzil and Stewart, D.S., "Theory of Detonation Shock Dynamics," <u>*Shock Waves Science and Technology Library*</u>, (80 pages), Chapter 7, Vol. 6 Shock Wave Science and Technology Reference Library Volume 6, (2012), pp 373-453

9.  **\*-**M. Clemenson, H. Krier, and N. Glumac, Blast Enhancement Effects of Various Forms of the Ti/2B Energetic System, Proceeding of the Spring Technical Meeting of the Combustion Institute, April (2012)

## 2013

10. Hernandez, A. M, J. B. Bdzil, and D. S. Stewart, "A MPI parallel level set algorithm for propagating front curvature dependent detonation shock fronts in complex geometries," ***Combustion Theory and Modelling***, Volume 17, Number 1, pp. 109-141(33), (2013).

11. Ling, Y., A. Haselbacher, S. Balachandar , F. M. Najjar, D. S. Stewart,  Shock Interaction with a Deformable Particle: Direct Numerical Simulation and Point-Particle Modeling,  ***J. Appl. Phys.*** 113, 013504 (2013).

12. D. Scott Stewart, N. Glumac, F. M. Najjar\*, M. J. Szuck , Hydrodynamics Computation of Jet Formation and Penetration for Micro- Shaped Charges, ***Procedia Engineering*** 58 (2013) 39 – 47

## 2014

13. Lieberthal, B., J. Bdzil, D.S. Stewart, "Modeling detonation of heterogeneous explosive with embedded particle using detonation shock dynamics: Normal and divergent propagation in regular and simplified microstructure," ***Combustion Theory and Modelling***, Volume 18, Issue 2, (2014), pages 204-241

14. **\*-**Michael D. Clemenson,  Stephanie Johnson,  Herman Krier,  and Nick Glumac ,Explosive Initiation of Various Forms of Ti/2B Reactive Materials, **Propellants Explos. Pyrotech**. (2014), 39, 454 – 462

## 2015

15. **\*-**Asay, B., John Bdzil, Joseph Foster, Alberto Hernandez, David Lambert and D. Scott Stewart, "A Multi-component Detonation Reaction Zone Model for Blast Explosives", ***Proceedings of the 15th International Detonation Symposium***, Office of Naval Research publication number 43-280-15, pp 445-455 (2015)

16. **\*-**S. Choi, D. Scott Stewart and Sunhee Yoo, Modeling of the Quenching of Blast Products from Energetic Materials by Expansion into Vacuum, ***Journal of Computational Physics***, 296 (2015) 158–183

17. **\*-**S. Koundinyan , M. Matalon , D. S. Stewart and Bdzil, J. B. Diffusion flames in condensed-phase energetic materials:  Application to Titanium-Boron combustion, in press ***Combustion and Flame*** (2015), doi:10.1016/j.combustflame.2015.08.023

18. **\*-**D. Scott Stewart, A Gibbs Formulation for Reactive Materials with Phase Change, to appear Proceedings of the Conference of the American Physical Society Topical Group on Shock Compression of Condensed Matter (2015)

19. **\*-**S. Koundinyan, M. Matalon, D. S. Stewart, J. B. Bdzil. Modeling reaction fronts of separated condensed phase reactants, to appear Proceedings of the Conference of the American Physical Society Topical Group on Shock Compression of Condensed Matter (2015)

20. **\*-**D. Scott Stewart, Santanu Chaudhuri, Kaushik Joshi. Kiabek Lee. Mirrored continuum and molecular scale simulations of the ignition of gamma phase RDX, to appear Proceedings of the Conference of the American Physical Society Topical Group on Shock Compression of Condensed Matter (2015)

21. **\*-**K. Lee, D. S. Stewart, M. Clemenson, N. Glumac, C. Murzyn, Modeling the Shock Ignition of a Copper Oxide Aluminum Thermite, to appear Proceedings of the Conference of the American Physical Society Topical Group on Shock Compression of Condensed Matter (2015)

22. Lieberthal, Brandon, D. Scott Stewart and John B. Bdzil, "Embedded Particle size distribution and its effect on detonation in composite explosives", submitted to ***Combustion Theory and Modeling (2015)***

23. D. Scott Stewart, Alberto Hernandez, and Kibaek Lee, Modeling Reaction Histories to Study Chemical Pathways in Condensed Phase Detonation, submitted to *J. Applied Physics (2015)*

24. **\*-**Kiabek Lee, Kaushik Joshi, Santanu Chaudhuri and D. Scott Stewart, Mirrored continuum and molecular scale simulations of the ignition of gamma phase RDX, submitted to J*. Chem. Physics (2015)*

## Papers in preparation to be submitted to archival journals

25. **\*-**Nick Glumac, D. Scott Stewart, John B. Bdzil, Joseph C. Foster, Michael Clemenson, Sushil Koundinyan, Shock Actuated Burning of Thermitic and Inter-Metallic Reactive Composite Materials, to be submitted to *Combustion and Flame*

26. **\*-**S. Koundinyan, M. Matalon, D. S. Stewart, Effect of density variations in axis-symmetric counterflow diffusion flames, to be submitted *to Combustion and Flame*

27. **\*-**K. Lee, D. S. Stewart, M. Clemenson, N. Glumac, C. Murzyn**,** Modeling the Shock Ignition of a Copper Oxide Aluminum Thermite, in preparation

28. **\*-**A Gibbs Formulation for Reactive Materials with Phase Change, D. Scott Stewart and students, to be submitted to *Journal of Chemical Physics*

## Masters Theses

29. **\*-**On the simulation and modeling for the reaction mechanism and solid state detonation in non-conventional explosives, Sungjin Choi, M.S., Theoretical and Applied Mechanics, Nov 2012.

## V. Students Supported and Graduated

(**\*** - wholly or partially supported by DTRA funds)

### Stewart-Group

| | |
|---|---|
| **\*- Sushilkumar P. Koundinyan** | **(PhD. Dec 2016)** |
| Alberto Hernandez | (PhD. May 2017) |
| **\*- Brandon Lieberthal** | **(PhD. Dec 2015)** |
| **\*- Kibaek Lee** | **(PhD. May 2017)** |
| **\*- Sunjin Choi** | **(MS. 2012)** |
| Lana Stekovic | (PhD. May 2018) |

### Glumac-Group

| | |
|---|---|
| **\*- Drew Coverdill** | **(MS. 2012)** |
| **\*- Michael Clemenson** | **(PhD. 2015)** |

### Undergraduate Students

**\*-Thomas Sanstrom**
**\*-Cameron Stewart**
**\*-Christopher Murzyn**

## VI. Senior Scientists

(**\*** - wholly or partially supported by DTRA funds)

| | |
|---|---|
| **\*-Prof. D. Scott Stewart** | **(PI)** |
| **\*-Prof. Nick Glumac** | **(PI)** |
| **\*-Dr. John B. Bdzil** | **(co-PI)** |
| **\*-Dr. Joseph C. Foster** | **(co-PI)** |

Dr. Sunhee Yoo        (research programmer)
Dr. Blaine Asay, Senior Research Scientist
**\*-Prof. Moshe Matalon**

## VII. Some Recent Publications that cite DTRA support

# Diffusion flames in condensed-phase energetic materials: Application to Titanium–Boron combustion

CrossMark

Sushilkumar P. Koundinyan, John B. Bdzil, Moshe Matalon, D. Scott Stewart*

*Mechanical Science and Engineering, University of Illinois, Urbana, IL, United States*

## ABSTRACT

The characteristics of a steady diffusion flame that arises at the interfaces of two condensed phase reactant streams that form an opposed counterflow are discussed. We assume that the flow is due to deformation from compaction or local heating and thermal expansion processes in the microscale environment of composite energetic materials. As a representative example of high temperature combustion of metal/intermetallic reactants, the overall reaction of titanium and boron to create titanium diboride products is considered under near isobaric conditions. The multi-component diffusion description uses a generalized Fick formulation with coefficients related to the binary diffusivities defined in the Maxwell–Stefan relations. A fairly simple depletion form with Arrhenius temperature dependent coefficients is used to describe the reaction rate. Several types of analyses are carried out at increasing levels of complexities: an asymptotic analysis valid in the limit of low strain rates (high residence time in the reaction zone), a constant mixture density assumption that simplifies the flow description, diffusion models with equal and unequal molecular weights for the various species, and a full numerical study for finite rate chemistry, composition-dependent density and strain rates extending from low to moderate values. All are found to agree remarkably well in describing the flame structure, the flame temperature and the degree of incomplete combustion. Of particular importance is the determination of a critical strain rate beyond which steady burning may no longer be observed. The analysis has a general character and can be applied to other condensed phase energetic material systems, where reaction and diffusion occur in the presence of flow and material deformation.

© 2015 The Combustion Institute. Published by Elsevier Inc. All rights reserved.

## 1. Introduction

Energetic materials are a broad class of manufactured materials that traditionally comprise both propellants and explosives, but include thermite and intermetallic/metal mixtures as well. They consist of molecular explosives and molecular oxidizer crystallites, like HMX and Ammonium perchlorate (AP), metal elements like aluminum (Al) and titanium (Ti), metal oxides like iron oxide, copper oxide, intermetallic elements like carbon, silicon and boron, and plastic binders and resins like HTPB. The mixtures are made from elements, or a composite of components that have been processed and have imperfections and contaminants, such as cracks or inclusions, or have been subjected to surface oxidation, as in propellants. The components in the mixture prior to the composite assembly, all have their own individual mechanical and thermo-chemical identity.

Explosive compounds are pre-mixed at the molecular level, whereas the mixtures of metals, metal oxides and intermetallics compound are initially separated constituents that react in the vicinity of the initial material boundaries, enabled by diffusion of reactants and products through the molecular condensed phase regions. Typically, the individual components are combined to make an agglomerated composite mixture of powders and other ingredients. The powders have a particle size distribution, with dimension that varies from one to several hundreds microns, and characteristic particle morphology. The mixtures are pressed or cast into a mold for applications.

Reactive energetic materials, as defined in a 2004 US National Academy of Sciences report [1], generally combine two or more inert solids, and an ignition source is required to start the chemical reaction at the interfaces of the initially separated reactants. Agglomerated composites can be ignited by shock compression if the components comprising the initial reactive mixture are not highly dense. The conditions required for ignition occur through the collapse of interstitial voids, typically of initial volume fraction in the range of 1–20%. During the void collapse, thermo-mechanical flows and material displacements occur due to the densification caused by the shock confinement, and lead to large strain rates in the reactive material

* Corresponding author. fax: +1 217- 244- 5707.
  *E-mail address:* dss@illinois.edu, dss@uiuc.edu, stewart26@comcast.net
 (D.S. Stewart).

components. The resulting deformations are associated with energy dissipation that cause localized heating (hot spots) which, in turn, generates thermal events that are needed for melting the constituent components and to initiate the reaction at the material interfaces. The localized thermal events in the mixture also lead to local streaming motions and greater species mobility of reactants.

Energetic materials fall generally into two broad classes based on how they are manufactured: (i) agglomerated composite mixtures of powders and other reactive components, and (ii) finely-spaced, structured or layered composites with specified interstitial spacing between the reactive components. The current state of experimental investigations and modeling of finely-spaced multilayered reactive materials has been recently reviewed by Rogachev [2], Weihs [3] and Adams [4]. A typical illustration is described by Weihs [5], where approximately 10 micron layers of foil (of say, nickel and aluminum) are pressed into a laminate ply. The formation of nickel/aluminum products, for example, starts with thermal initiation (heating) of the composite material that first melts the aluminum and allows the chemical reaction to proceed. The modeling effort focuses on the effect of the laminate bilayer thickness on ignition and on the velocity of the self-propagating reactions of a number of reactive material pairs. In general, steady self-propagation of a reacting front in the laminate material moves perpendicular to the normal of the planes of laminate plies. The speed of the steady self-propagation reaction front is found to be dependent on the ply spacing and composition [6]. For example, Sraj [7] studied the response of Ni/Al multilayered composites to shock compression; he used the Sandia CTH hydrocode to simulate the mechanical deformation of layered Ni/Al material to shock compression and investigate the effects of the bilayer thickness and the shock velocity and orientation on the combustion process. When the normal to the plane of the impact that creates the shock is in the same direction as the normal to the plane of the laminate plies, the propagation process is found to be highly unsteady.

An alternative to the well-structured layered composites are agglomerated materials made of a mixture of reactive and inert components. Glumac et al. [8] have recently reported results of shock compaction experiments on porous materials that are initially composed of two reactive components. Systems that have been studied include the aluminum (Al), copper oxide (CuO) thermite, and the metal/intermetallic system composed of titanium, silicon, and titanium, boron. A typical shock compaction experiment is carried out for 80% porous, stoichiometric mixture of components, with the initial mass fractions based on the overall equilibrium products. For the Al, CuO system the stoichiometric reaction is $2\,Al + 3\,CuO \rightarrow Al_2O_3 + 3\,Cu$. The reactive material sample is placed in a striker assembly, and compacted by the action of two metal bars that are shock loaded by the firing of detonators on each end. A sustained heterogeneous front was found to propagate at an average speed of approximately 6–20 cm/sec. High speed microscopic photography was used to record the emitted light seen through a small observation window. On a length scale of 10–20 $\mu$m one observes the sudden formation and disappearance of intense spots of light, corresponding to intense and weak chemical reactions recurring within a time interval of approximately 100 $\mu$s. Similar results were observed for the titanium - silicon system and more extensive experiments are planned for the titanium - boron system. These experiments clearly demonstrate that the overall combustion process is highly unsteady. While the lead reactive front after shock compaction is observed to propagate at a well-defined average velocity, measurable and robust, time-dependent heterogeneous reaction–diffusion processes occur on the micro-scale, corresponding to the initial size of the reactive component particles, before and after the passage of the lead shock. Since the component materials and their reactants are very hot and experience significant thermal expansion, the chemically reacting material experiences a distribution of local flow velocities and strain rates, primarily at the material interface of the reacting components.
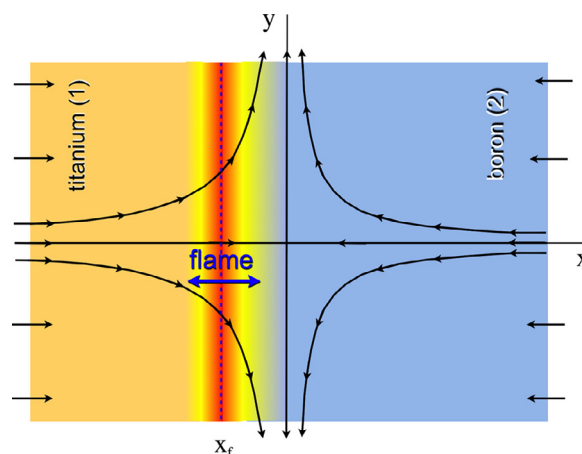


**Fig. 1.** Schematic of the condensed phase counterflow diffusion flame, with titanium entering from the left and boron from the right. The color shades clearly delineate the planar mixing region and reaction zone.

The theoretical modeling approach for the finely-space laminate, or regular structured materials, can be summarily described as an approach that lumps, or relies on cross-sectional averages for all transport phenomena, such as bulk heat transfer and diffusion, and for all material properties of the laminate/arrays [4]. These reduced models seem to appropriately describe observed phenomena that depend on average properties of the system, such as bulk temperature and reaction extent, or the self-propagation speed of a reactive front propagating along the axis of the plane of the plies. They do not explicitly describe the reaction–diffusion phenomena at material interfaces, and cannot delineate separate molecularly distinct reactants. The focus in this work is exactly on the processes taking place on a small-scale of the initially-separated component materials that comprise the mixtures, that are not necessarily layered or structured. Our approach delineates separate molecularly distinct reactants and employs a multicomponent, thermodynamic formulation with separated reactants and products, each with their own properties. While we employ some simplifications, we do not use a lumped, averaged formulation in the same sense of the reduced models found in the analysis of finely-spaced laminates or arrays. Fundamental understanding of these local events will serve as a basis for future modeling of time-dependent reaction processes in both classes of energetic materials, agglomerated composites and finely-spaced, structured or layered composites.

In this paper we examine the reaction–diffusion processes in the mixing region of two opposed streams of distinct reactants, that stagnate on the stream axis as shown in Fig. 1. The flow due to material deformation, local heating, and thermal expansion processes, has been presumably established at the micro-scale by prior shock compaction events that we do not model; such considerations were given, for example, in the studies reported in [7,9]. The flow of opposed streams is characterized by a single strain rate – the ratio of the average displacement speed to the length scale that characterizes the material nonuniformity – or, equivalently, the inverse of a residence time that we presume given. We show that in this counterflow configuration, a balance between advection, diffusion and chemical reaction is possible under steady conditions when the strain rate is not too large. Otherwise, the only possible balance is that of a nearly-frozen or weak burning state (not discussed in this paper). In the larger picture, we envision a cooperative time-dependent mechanism between local reaction sites that experience intense reaction and slow reaction at local interfaces, that depends on the local strain rate distribution in the composite material.

Although our analysis holds for any three-components system, we have chosen the titanium (Ti) and boron (B) system as

a representative example of metal/intermetallic reactive material system. Their overall reaction, to create titanium diboride ($TiB_2$) products,

$$Ti + 2B \rightarrow TiB_2, \tag{1}$$

is considered under nearly-isobaric conditions, such that the pressure is represented by the hydrostatic pressure. The equation of state of the three components and the formulation that defines the equilibrium equation of state of the mixture is based on multicomponent thermodynamics formulations that are similar to those used in the study of metallurgy and materials [10]. As such, the formulation is based on Gibbs thermodynamic potentials where one assumes that at each point of the condensed phase mixture, there is a single stress state and temperature. Each isolated component is assumed to have its own distinct reference density, and we neglect thermal expansion in the components. This is consistent with the notion that the change in composition due to reaction is much larger than changes due to thermal expansion. As a result the mechanical equation of state for the mixture takes a simple form whereby the specific volume of the mixture is simply a sum of the intrinsic densities weighted with the mass fraction of each component. This form of the mechanical equation of state stands in contrast with that for a mixture of reacting gases that is a relation between the specific volume, pressure, temperature and mass fractions. The diffusion model for the components is derived from an effective Fick diffusion formulation as described by Curtiss [11] and Curtiss and Bird [12], whereby a Maxwell–Stefan law formulated in terms of binary diffusivities is expressed as a generalized Fick diffusion law with symmetric diffusion coefficients. The resulting diffusion coefficients used in our model are then chosen to lead consistent results with experimental data reported by Trunov et al. [13].

The governing equations describing the steady burning of initially separated titanium and boron in a counterflow geometry are presented in the next section. These equations are addressed first under the assumption of constant mixture density, which enables the construction of an analytical solution in the fast chemistry limit. The expressions for flame position and temperature are used when compared to experimental data to estimate binary diffusion coefficients that are not well-known, and or measured under restricted conditions. We then address numerically the general case, of finite rate chemistry and when the density of the mixture varies reflecting the local composition of the mixtures. In particular, we derive extinction conditions that differentiate between vigorous and weak burning between titanium and boron. We note that the analytical solution, valid for large Damköhler numbers, is used to validate the numerical solution and calibrate the corresponding strain rates in deriving the extinction conditions.

## 2. Formulation

The counterflow geometry under consideration is shown in Fig. 1, where far to the left (state 1) there is only titanium and far to the right (state 2) there is only boron; the intrinsic densities are denoted by $\hat{\rho}_{1_0}$ and $\hat{\rho}_{2_0}$, respectively. Under steady conditions, the material deformation may be described by a velocity field **v** of the form $\mathbf{v} = \left(u(x), y\,\bar{v}(x)\right)$. This "similarity solution" implies that the pressure gradient in the transverse direction $y$ is necessarily linear and admits planar combustion fronts such that all state variables, the mass fractions $Y_i$, the density $\rho$, and temperature $T$, are functions of $x$ alone. The constituents in the combustion zone include titanium of mass fraction $Y_1$, boron of mass fraction $Y_2$, and titanium diboride products of mass fraction $Y_3$. Overall mass conservation implies that

$$Y_1 + Y_2 + Y_3 = 1. \tag{2}$$

The conductivity $k$ and specific heat (at constant pressure) $c_p$ of the mixture (defined as mass-weighted averages) are, in general,

functions of temperature but for simplicity they will be taken here as constants. Finally, the chemical reaction (1) between Ti and B is assumed to proceed at a rate

$$\omega = \mathcal{B} Y_1 Y_2^2\, e^{-E/\mathcal{R}T} \tag{3}$$

where $E$ is the activation energy, $\mathcal{R}$ is the universal gas constant and $\mathcal{B}$ is an appropriately defined pre-exponential factor. Different reaction orders could be considered without difficulty; the present form that simplifies the reaction to one-step process was made for simplicity.

### 2.1. Conservation equations

The governing equations, describing conservation of mass, momentum, and energy under steady conditions simplify to

$$\frac{d}{dx}(\rho u) + \rho\,\bar{v} = 0 \tag{4}$$

$$\rho u \frac{d\bar{v}}{dx} + \rho\,\bar{v}^2 = C \tag{5}$$

$$\rho u c_p \frac{dT}{dx} - k \frac{d^2 T}{dx^2} = Q\omega \tag{6}$$

$$\rho u \frac{dY_1}{dx} + \frac{d}{dx}(\rho Y_1 V_1) = -W_1 \omega \tag{7}$$

$$\rho u \frac{dY_2}{dx} + \frac{d}{dx}(\rho Y_2 V_2) = -2W_2 \omega \tag{8}$$

where $V_i$, $W_i$ stand for the diffusion velocity and molecular weight of species $i$, and $Q$ is the overall heat release. As noted earlier, the pressure gradient in the transverse $y$-direction is linear, given by $\partial p/\partial y = -Cy$, where $C$ is a constant determined by the far field boundary conditions. Specifically, Eq. (5) implies that there is a relation between the densities and strain rates at the far ends, such that

$$\hat{\rho}_{1_0} \epsilon_1^2 = \hat{\rho}_{2_0} \epsilon_2^2 = C. \tag{9}$$

Hence the motion of the reactants impinging on each other is characterized by a single strain rate $\epsilon$ (in units of 1/s) which we choose as $\epsilon = \epsilon_1/2$; the factor of 2 is introduced solely to facilitate the form of the analytical asymptotic solution described below. The axial dependence of the pressure can be obtained a-posteriori by solving the $x$-component of the momentum equation (not written above).

Eqs. (4)–(8) must be supplemented with constitutive relations for the diffusion velocities and an equation of state for the mixture. Starting with the assumption that the Gibbs free energy of each component of the mixture can be summed, the Gibbs potential for the mixture which is a function of pressure, temperature, and mixture composition is

$$g = \sum_{i=1}^{3} g_i(p, T) Y_i, \tag{10}$$

where the energies related to mixing have been neglected. The specific volume $\upsilon = 1/\rho$ of the mixture and individual components are given by the thermodynamic relation:

$$\upsilon = \left.\frac{\partial g}{\partial p}\right|_{T, Y_i} \quad \text{and} \quad \upsilon_i = \left.\frac{\partial g_i}{\partial p}\right|_T, \tag{11}$$

where $\upsilon_i$ are the partial volumes, or the volume of the components. This leads to

$$\upsilon = \sum_{i=1}^{3} \upsilon_i(p, T) Y_i \tag{12}$$

which is the mechanical equation of state for the mixture. (Note: The symbol $\upsilon$ represents the specific volume and should not be confused with $v$ which represents the y-component of velocity.) If we further

assume that the volume change due to pressure variations is small, and neglect the effect of temperature, the partial volumes $\upsilon_i$ can be approximated by their reference values $\hat{\upsilon}_{i_0}$. The mechanical equation of state (12), when expressed in terms of the densities, then becomes

$$\rho^{-1} = \sum_{i=1}^{3} Y_i \, \hat{\rho}_{i_0}^{-1} \tag{13}$$

where $\hat{\rho}_{i_0}$ is the intrinsic density, and $\hat{\rho}_{i_0}^{-1}$ the intrinsic specific volume, of species $i$. Using (2) the equation of state simplifies to

$$\frac{1}{\rho} = \frac{1}{\hat{\rho}_{3_0}} + \left( \frac{1}{\hat{\rho}_{1_0}} - \frac{1}{\hat{\rho}_{3_0}} \right) Y_1 + \left( \frac{1}{\hat{\rho}_{2_0}} - \frac{1}{\hat{\rho}_{3_0}} \right) Y_2. \tag{14}$$

With the flow specified by the strain rate $\epsilon$ and the material properties far to the left (denoted by subscript 1) and far to the right (denoted by subscript 2) assumed uniform, the boundary conditions are:

$$du/dx \sim -2\epsilon \quad \text{as } |x| \to \infty, \tag{15}$$

$$\rho = \hat{\rho}_{1_0}, \ Y_1 = 1, \ Y_2 = 0, \ T = T_\infty \quad \text{as } x \to -\infty, \tag{16}$$

$$\rho = \hat{\rho}_{2_0}, \ Y_1 = 0, \ Y_2 = 1, \ T = T_\infty \quad \text{as } x \to +\infty. \tag{17}$$

Note that there is no need to specify a condition for $\bar{v}$, because it is obtained from

$$\bar{v} = -\frac{1}{\rho} \frac{d}{dx}(\rho u) \tag{18}$$

by differentiation.

When density variations are small, the equation of state (14) can be effectively replaced by $\rho = $ constant, and the velocity field everywhere is given by

$$u = -2\epsilon x, \quad \bar{v} = 2\epsilon. \tag{19}$$

The problem reduces to the reaction–diffusion system (6)–(8). The constant-density approximation will be used for simplicity in the asymptotic description described below. In general, variations in the density modify the overall velocity field which, in turn, affects the combustion field. In Section 4, numerical computations are carried out in order to assess the importance of density variations in condensed-phase combustion.

### 2.2. Diffusion

The most common expressions used for multi-component diffusion are the Maxwell–Stefan (MS) relations

$$\nabla X_i = \sum_j \frac{X_i X_j}{\mathscr{D}_{ij}} (\mathbf{V}_j - \mathbf{V}_i), \tag{20}$$

with the summation taken over all species present [14]; here $X_i$ is the molar fraction, $\mathbf{V}_i$ is the diffusion velocity vector of species $i$, and $\mathscr{D}_{ij} = \mathscr{D}_{ji}$ is the binary diffusivity of a pair of species $(i, j)$. Although this relation was derived for a dilute ideal gas mixture, it has been often applied to condensed phase media [15].

The use of the Maxwell–Stefan relations is quite complicated because the diffusion velocities $\mathbf{V}_i$ are not expressed explicitly in terms of the concentration gradients. A common practice is to use the generalized Fick equations

$$\mathbf{V}_i = \sum_j \mathbb{D}_{ij} \nabla X_j \tag{21}$$

with coefficients $\mathbb{D}_{ij}$, referred to as *Fick diffusivities*, that are related to the binary diffusivities $\mathscr{D}_{ij}$, but unlike the binary diffusivities they

are concentration dependent and may not necessarily be all positive. They must, however, satisfy the constraints [12]

$$\mathbb{D}_{ij} = \mathbb{D}_{ji}, \quad \text{for all } i, j, \quad \sum_i \mathbb{D}_{ij} Y_i = 0 \quad \text{for all } j.$$

The expressions relating Fick and binary diffusivities for a ternary mixture [16] are listed in the Appendix. Converting Eq. (21) from mole to mass fraction yields:

$$Y_i V_i = a_i \nabla Y_1 + b_i \nabla Y_2, \quad i = 1, 2 \tag{22}$$

where

$$a_1 = \frac{W_1(Y_2 + Y_3)(-Y_2 W_3 - W_2 + Y_2 W_2)\mathscr{D}_{13}\mathscr{D}_{12} + Y_1 Y_2 W_2 (W_1 - W_3)\mathscr{D}_{23}\mathscr{D}_{12}}{Y_1 W_2 W_3 \mathscr{D}_{23} + Y_2 W_1 W_3 \mathscr{D}_{13} + Y_3 W_2 W_1 \mathscr{D}_{12}}$$
$$- \frac{W_3 Y_1 (W_2 - Y_2 W_2 + Y_2 W_1)\mathscr{D}_{23}\mathscr{D}_{13}}{Y_1 W_2 W_3 \mathscr{D}_{23} + Y_2 W_1 W_3 \mathscr{D}_{13} + Y_3 W_2 W_1 \mathscr{D}_{12}}$$

$$b_1 = -\frac{Y_1 W_1 (Y_2 + Y_3)(W_2 - W_3)\mathscr{D}_{13}\mathscr{D}_{12} + Y_1 W_2 (-W_1 + Y_1 W_1 - W_3 Y_1)\mathscr{D}_{23}\mathscr{D}_{12}}{Y_1 W_2 W_3 \mathscr{D}_{23} + Y_2 W_1 W_3 \mathscr{D}_{13} + Y_3 W_2 W_1 \mathscr{D}_{12}}$$
$$+ \frac{Y_1 W_3 (-Y_1 W_2 - W_1 + Y_1 W_1)\mathscr{D}_{23}\mathscr{D}_{13}}{Y_1 W_2 W_3 \mathscr{D}_{23} + Y_2 W_1 W_3 \mathscr{D}_{13} + Y_3 W_2 W_1 \mathscr{D}_{12}}$$

$$a_2 = -\frac{Y_2 W_1 (-W_2 + Y_2 W_2 - Y_2 W_3)\mathscr{D}_{13}\mathscr{D}_{12} + Y_2 W_2 (Y_1 + Y_3)(W_1 - W_3)\mathscr{D}_{23}\mathscr{D}_{12}}{Y_1 W_2 W_3 \mathscr{D}_{23} + Y_2 W_1 W_3 \mathscr{D}_{13} + Y_3 W_2 W_1 \mathscr{D}_{12}}$$
$$- \frac{Y_2 W_3 (-Y_2 W_2 + Y_2 W_1 + W_2)\mathscr{D}_{23}\mathscr{D}_{13}}{Y_1 W_2 W_3 \mathscr{D}_{23} + Y_2 W_1 W_3 \mathscr{D}_{13} + Y_3 W_2 W_1 \mathscr{D}_{12}}$$

$$b_2 = \frac{Y_2 Y_1 W_1 (-W_3 + W_2)\mathscr{D}_{13}\mathscr{D}_{12} + W_2 (Y_1 + Y_3)(-W_1 + Y_1 W_1 - Y_1 W_3)\mathscr{D}_{23}\mathscr{D}_{12}}{Y_1 W_2 W_3 \mathscr{D}_{23} + Y_2 W_1 W_3 \mathscr{D}_{13} + Y_3 W_2 W_1 \mathscr{D}_{12}}$$
$$+ \frac{Y_2 W_3 (-Y_1 W_2 - W_1 + Y_1 W_1)\mathscr{D}_{23}\mathscr{D}_{13}}{Y_1 W_2 W_3 \mathscr{D}_{23} + Y_2 W_1 W_3 \mathscr{D}_{13} + Y_3 W_2 W_1 \mathscr{D}_{12}}.$$

The species Eqs. (7)–(8) can then be written as

$$\rho u \frac{dY_1}{dx} + \frac{d}{dx} \left[ \rho \left( a_1 \frac{dY_1}{dx} + b_1 \frac{dY_2}{dx} \right) \right] = -W_1 \omega, \tag{23}$$

$$\rho u \frac{dY_2}{dx} + \frac{d}{dx} \left[ \rho \left( a_2 \frac{dY_1}{dx} + b_2 \frac{dY_2}{dx} \right) \right] = -2W_2 \omega. \tag{24}$$

A simplification that can be used for analytical convenience results from assuming equal molecular weights $W_1 = W_2 = W_3$, then

$$a_1 = -\mathscr{D}_{13} \frac{\mathscr{D}_{12} + (\mathscr{D}_{23} - \mathscr{D}_{12})Y_1}{(\mathscr{D}_{23} - \mathscr{D}_{12})Y_1 + (\mathscr{D}_{13} - \mathscr{D}_{12})Y_2 + \mathscr{D}_{12}}$$

$$b_1 = \frac{\mathscr{D}_{23}(\mathscr{D}_{12} - \mathscr{D}_{13})Y_1}{(\mathscr{D}_{23} - \mathscr{D}_{12})Y_1 + (\mathscr{D}_{13} - \mathscr{D}_{12})Y_2 + \mathscr{D}_{12}}$$

$$a_2 = \frac{\mathscr{D}_{13}(\mathscr{D}_{12} - \mathscr{D}_{23})Y_2}{(\mathscr{D}_{23} - \mathscr{D}_{12})Y_1 + (\mathscr{D}_{13} - \mathscr{D}_{12})Y_2 + \mathscr{D}_{12}}$$

$$b_2 = -\mathscr{D}_{23} \frac{\mathscr{D}_{12} + (\mathscr{D}_{13} - \mathscr{D}_{12})Y_2}{(\mathscr{D}_{23} - \mathscr{D}_{12})Y_1 + (\mathscr{D}_{13} - \mathscr{D}_{12})Y_2 + \mathscr{D}_{12}}$$

## 3. Asymptotic solution – the Burke–Schumann limit

We first present analytical results in the limit of infinitely fast chemical reaction, known in the literature as the Burke–Schumann limit. The solutions obtained in this limit provide a simple illustration of the flame structure. An appropriate time scale may be defined as the ratio of a representative length associated with the distance between particles and a characteristic microscale velocity associated with material deformation. The inverse of this time is the characteristic strain rate, and the fast chemistry limit corresponds to weak strain rates. The corresponding Damköhler number, or the ratio of the flow-to-chemistry time scales, is therefore large. Although asymptotic methods that accounts for finite rate chemistry and thus span a wider range of strain rates (up to flame extinction) are available for the related gaseous problem [17,18], their extension to energetic materials is nontrivial and will be discussed in a future publication. Here we rely on numerical methods to examine the dependence of the solution on the strain rate for steady combustion.

In the fast chemistry limit the chemical reaction occurs along a sheet, at $x = x_f$ say, where the two reactants are in contact. Elsewhere, the chemical reaction is negligibly small and we are left solving the energy and species equations on either side of the sheet, with $\omega = 0$. The flame sheet separates a region where there is only titanium ($x < x_f$), from a region where there is only boron ($x > x_f$). Since $Y_2 = 0$ for $x < x_f$, we find that

$$a_1 = -\mathscr{D}_{13}, \quad b_1 = \frac{\mathscr{D}_{23}(\mathscr{D}_{12} - \mathscr{D}_{13})Y_1}{\mathscr{D}_{23}Y_1 + \mathscr{D}_{12}(1 - Y_1)},$$

$$a_2 = 0, \qquad b_2 = -\frac{\mathscr{D}_{23}\mathscr{D}_{12}}{\mathscr{D}_{23}Y_1 + \mathscr{D}_{12}(1 - Y_1)}.$$

and, since $Y_1 = 0$ for $x > x_f$, we find that

$$a_1 = -\frac{\mathscr{D}_{13}\mathscr{D}_{12}}{\mathscr{D}_{13}Y_2 + \mathscr{D}_{12}(1 - Y_2)}, \quad b_1 = 0,$$

$$a_2 = \frac{\mathscr{D}_{13}(\mathscr{D}_{12} - \mathscr{D}_{23})Y_2}{\mathscr{D}_{13}Y_2 + \mathscr{D}_{12}(1 - Y_2)}, \qquad b_2 = -\mathscr{D}_{23}.$$

We note parenthetically that the simplification of the coefficients $a_i$, $b_i$ applies even for unequal molecular weights. All variables must be continuous at the flame sheet, but their derivatives are not; the mass and energy fluxes must satisfy the relations

$$\frac{\alpha}{Q/c_p}\left[\frac{dT}{dx}\right] = \frac{1}{W_1}\left[a_1\frac{dY_1}{dx} + b_1\frac{dY_2}{dx}\right] = \frac{1}{2W_2}\left[a_2\frac{dY_1}{dx} + b_2\frac{dY_2}{dx}\right],$$
(25)

where the square brackets $[\cdot]$ denote the jump, namely the difference between the values at $x_f^+$ and $x_f^-$, and $\alpha = k/\rho c_p$ is the thermal diffusivity of the mixture. The conditions (25) imply that the fluxes of titanium and boron towards the flame sheet are in stoichiometric proportions, and they specify the proportion of heat from the total heat released conducted to one or the other side of the sheet.

For simplicity, we have also adopted in this section the constant density approximation. The mathematical problem on either side of the flame sheet then consists of

$$2\epsilon x\frac{dT}{dx} + \alpha\frac{d^2T}{dx^2} = 0 \quad \text{for } x \lessgtr x_f$$
(26)

$$2\epsilon x\frac{dY_1}{dx} + \mathscr{D}_{13}\frac{d^2Y_1}{dx^2} = 0 \quad \text{for } x < x_f$$
(27)

$$Y_1 \equiv 0 \quad \text{for } x > x_f$$
(28)

$$Y_2 \equiv 0 \quad \text{for } x < x_f$$
(29)

$$2\epsilon x\frac{dY_2}{dx} + \mathscr{D}_{23}\frac{d^2Y_2}{dx^2} = 0 \quad \text{for } x > x_f$$
(30)

together with the boundary conditions (16) and (17), with $\rho$ assumed constant, and the jump relations

$$[T] = [Y_1] = [Y_2] = 0$$
(31)

$$\frac{\alpha}{Q/c_p}\left[\frac{dT}{dx}\right] = -\frac{\mathscr{D}_{13}}{W_1}\left[\frac{dY_1}{dx}\right] = -\frac{\mathscr{D}_{23}}{2W_2}\left[\frac{dY_2}{dx}\right]$$
(32)

across $x = x_f$. The solution is readily obtained as

$$T = \begin{cases} T_\infty + (T_f - T_\infty)\dfrac{1 + \text{erf}\left(\sqrt{\epsilon/\alpha}\,x\right)}{1 + \text{erf}\left(\sqrt{\epsilon/\alpha}\,x_f\right)} & x < x_f \\[4mm] T_\infty + (T_f - T_\infty)\dfrac{1 - \text{erf}\left(\sqrt{\epsilon/\alpha}\,x\right)}{1 - \text{erf}\left(\sqrt{\epsilon/\alpha}\,x_f\right)} & x > x_f \end{cases}$$
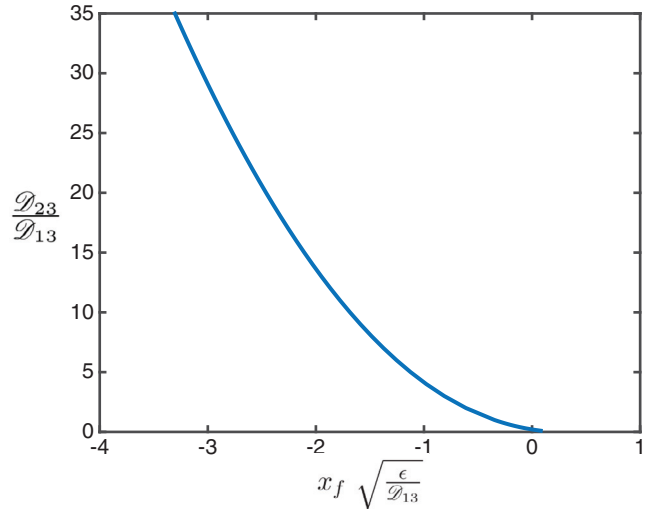
**Fig. 2.** Variation of the flame sheet position with $\mathscr{D}_{23}/\mathscr{D}_{13}$, based on the asymptotic solution.

$$Y_1 = \begin{cases} 1 - \dfrac{1 + \text{erf}(\sqrt{\epsilon/\mathscr{D}_{13}}\,x)}{1 + \text{erf}(\sqrt{\epsilon/\mathscr{D}_{13}}\,x_f)} & x < x_f \\[4mm] 0 & x > x_f \end{cases}$$

$$Y_2 = \begin{cases} 0 & x < x_f \\[4mm] 1 - \dfrac{1 - \text{erf}(\sqrt{\epsilon/\mathscr{D}_{23}}\,x)}{1 - \text{erf}(\sqrt{\epsilon/\mathscr{D}_{23}}\,x_f)} & x > x_f \end{cases}$$

The position $x_f$ of the flame sheet and the adiabatic flame temperature $T_f$, defined as the value of $T$ at the flame sheet, satisfy

$$\frac{1 + \text{erf}(\sqrt{\epsilon/\mathscr{D}_{13}}\,x_f)}{1 - \text{erf}(\sqrt{\epsilon/\mathscr{D}_{23}}\,x_f)} = \nu\sqrt{\frac{\mathscr{D}_{13}}{\mathscr{D}_{23}}}\,\frac{e^{\epsilon x_f^2/\mathscr{D}_{23}}}{e^{\epsilon x_f^2/\mathscr{D}_{13}}}$$
(33)

$$T_f = T_\infty + \frac{1}{2}\frac{Q/c_p}{W_1}\sqrt{\frac{\mathscr{D}_{13}}{\alpha}}\frac{1 - \text{erf}^2(\sqrt{\epsilon/\alpha}\,x_f)}{1 + \text{erf}(\sqrt{\epsilon/\mathscr{D}_{13}}\,x_f)}\frac{e^{\epsilon x_f^2/\alpha}}{e^{\epsilon x_f^2/\mathscr{D}_{13}}}$$
(34)

where $\nu = 2W_2/W_1$ is a mass-weighted stoichiometric ratio. The position $x_f$ is determined from the transcendental Eq. (33) using an iterative process. We note that for a given strain rate $\epsilon$ the position $x_f$ depends only on the binary diffusivities Ti-TiB$_2$ and B-TiB$_2$, and is independent of the diffusivity of Ti-B because there is no boron in the titanium region and vice-versa. Once $x_f$ is determined, the flame temperature can be calculated from (34) by direct evaluation. Evidently, the latter depends on the heat released $Q$ and thermal diffusivity $\alpha$.

For equal diffusivities $\mathscr{D}_{13} = \mathscr{D}_{23} \equiv \mathscr{D}$, Eq. (33) reduces to

$$\text{erf}(\sqrt{\epsilon/\mathscr{D}}\,x_f) = \frac{\nu - 1}{\nu + 1}.$$

For the titanium–boron reaction the mass-weighted stoichiometric ratio $\nu \approx 0.45$, implying that $x_f \approx -0.41\sqrt{\mathscr{D}/\epsilon}$ and the flame sheet lies on the titanium side of the stagnation plane. If the Lewis number is assumed equal to one, i.e., $\mathscr{D} = \alpha$, the flame temperature is given by

$$T_f = T_\infty + \frac{Q/c_p W_1}{1 + \nu}.$$

In the absence of differential (unity Lewis number) and preferential (unequal mass diffusivities) diffusion, the flame temperature results from a simple energy balance.

Figure 2 displays the dependence of the scaled flame sheet location on the ratio $\mathscr{D}_{23}/\mathscr{D}_{13}$, for a fixed $\nu$. This ratio is typically larger than one, since boron atoms have an effectively smaller atomic radius and hence diffuse more readily through titanium-diboride than

does the titanium atom [19,20]. We see that the flame sheet generally resides on the titanium side of the stagnation plane and moves further to the left when the diffusivity of boron into the titanium-diboride products increases relative to the diffusivity of titanium into the titanium-diboride products.

The only explicit results presented here from the asymptotic solution are the expressions for the flame position and temperature. Predictions based on these expressions are used in conjunction with experimental data to extract kinetic parameters that are not well known or were measured under limited conditions. Moreover, the asymptotic solution is used to validate the numerical solution of the governing equations for large values of the Damköhler number (or small strain rates) and to properly calibrate the strain rate, in order to derive extinction conditions.

## 4. Numerical solution – finite-rate chemistry

To examine the effects of finite-rate chemistry, the boundary value problem consisting of Eqs. (4)–(6) and (23)–(24) and boundary conditions (15)–(17) must be addressed. The numerical procedure is described next, followed by results pertaining to titanium-boron combustion.

### 4.1. Numerical procedure

Steady solutions of the aforementioned boundary value problem are obtained numerically as the long time behavior of the time-dependent equations

$$\rho \frac{\partial \bar{v}}{\partial t} + \rho u \frac{\partial \bar{v}}{\partial x} + \rho \bar{v}^2 = C \tag{35}$$

$$\rho \frac{\partial Y_1}{\partial t} + \rho u \frac{\partial Y_1}{\partial x} + \frac{\partial}{\partial x}\left[\rho\left(a_1 \frac{\partial Y_1}{\partial x} + b_1 \frac{\partial Y_2}{\partial x}\right)\right] = -W_1\,\omega \tag{36}$$

$$\rho \frac{\partial Y_2}{\partial t} + \rho u \frac{\partial Y_2}{\partial x} + \frac{\partial}{\partial x}\left[\rho\left(a_2 \frac{\partial Y_1}{\partial x} + b_2 \frac{\partial Y_2}{\partial x}\right)\right] = -2W_2\,\omega \tag{37}$$

$$\rho c_p\left(\frac{\partial T}{\partial t} + u \frac{\partial T}{\partial x}\right) - k \frac{\partial^2 T}{\partial x^2} = Q\omega, \tag{38}$$

with $\bar{v}$ obtained from

$$\rho \bar{v} = -\frac{d}{dx}(\rho u) \tag{39}$$

and $\rho$ from (14). Initially, these equations were solved using an explicit time marching method until the solution converges to its equilibrium state. The integration in time starts with an initial guess, taken here as the asymptotic solution discussed in the previous section. A fourth order approximation was used to compute the first order and second order space derivatives and a fourth order Runge–Kutta (RK4) method was used for time stepping. The extent of the numerical domain depends on the strain rate value, with lower strain rates requiring a larger domain. This, however, can be overcome by normalizing $x$ with the thermal diffusion length $l_d = \sqrt{\alpha/\epsilon}$, as is also evident from the analytical form of the asymptotic solution. Due to large stiffness arising from the Arrhenius exponential in the reaction rate term, we found that the time step, in general, could not exceed $10^{-9}$ and to properly describe the solution at low strain rates where the reaction zone becomes extremely thin, a fine grid is also required. As a result, convergence to the equilibrium state was very slow even after parallelizing the numerical code. Determining the solution over a wide range of strain rate conditions requires a faster converging algorithm.

To overcome the computational stiffness, an implicit time relaxation method was implemented. First and second order spatial derivatives are approximated by second order finite difference

**Table 1**
Property values of representative physical parameters used in the computations.

| Property | Symbol | Value | Reference |
|---|---|---|---|
| Heat release | $Q$ | −323.8 kJ/mol | [23] |
| Molar mass of Ti | $W_1$ | 47.87 g/mol | |
| Molar mass of B | $W_2$ | 10.81 g/mol | |
| Molar mass of TiB$_2$ | $W_3$ | 69.85 g/mol | |
| Averaged molar mass | $W_c$ | 50 g/mol | |
| Intrinsic density of Ti | $\hat{\rho}_{1_0}$ | 4.5 g/cc | |
| Intrinsic density of B | $\hat{\rho}_{2_0}$ | 2.34 g/cc | |
| Intrinsic density of TiB$_2$ | $\hat{\rho}_{3_0}$ | 4.52 g/cc | |
| Averaged density | $\hat{\rho}_{c_0}$ | 3.8 g/cc | |
| Heat capacity | $c_p$ | 900 J/(kg K) | [23] |
| Thermal conductivity | $k$ | 36 W/(m K) | [24–26] |
| Pre exponential factor | $\mathcal{B}$ | 7.6e16 mol/(m³ s) | [27] |
| Activation energy | $E_a$ | 318 kJ/mol | [27] |
| Binary diffusivity of Ti-B | $\mathscr{D}_{12}$ | 0.2 m²/s | [28] |

schemes on a uniform grid, and for time stepping we use a backward Euler method, such that a generic equation of the form $\partial \phi / \partial t = f(t, \phi)$ is approximated by $\phi^{n+1} = \phi^n + \Delta t\, f(t^{n+1}, \phi^{n+1})$, where $n$ denotes the time step and $\Delta t$ the time increment. A damped Newton–Raphson solver is then used for the solution of the resulting nonlinear system at each time step. The stiffness in the governing equations lead to strong fluctuations, and consequently sharp gradients in the Jacobian matrix that may cause the numerical solution to diverge. We have therefore implemented a relaxation parameter during each iterative update to limit the fluctuations; the value 0.1 was found appropriate for our calculations. The PetSC sparse solver [21] was used for the system that arises during the Newton–Raphson iteration. This approach has significantly reduced the time step relative to the explicit scheme from $10^{-9}$ to $10^{-2}$, for the same spatial grid distribution.

In order to generate solutions for increasing values of the strain rate $\epsilon$ and draw response curves of quantities of interest (e.g., flame temperature, mass fraction of unconsumed reactants, etc.) as a function of $\epsilon$, we start with a small strain rate value of $\epsilon = 0.01$ s$^{-1}$ using the asymptotic solution as an initial guess, and advance in time until the incremental changes in the solution at all points in the domain of integration are less than a tolerance error, here taken as $10^{-3}$. Convergence is guaranteed only when the long-time equilibrium solution is stable. This approach, therefore, works well for small-to-moderate values of $\epsilon$, but fails at larger values when the solution of the boundary value problem becomes multi-valued, and the response curve develops a turning point with stable and unstable branches. To construct all steady solutions, stable and unstable, particularly near the turning point, we use the continuation approach proposed by Kurdyumov and Matalon [22]. The time-dependent Eqs. (35)–(39) were solved with an additional constraint that the temperature remains constant at some reference point, say $T(x^*) = T^*$. The constraint is used to iterate on the value of $\epsilon$ until both, the strain rate and the space distribution of solution, do not vary significantly from one time step to the next. By selecting $T^*$ judiciously, this procedure always converges allowing to generate the entire response curve through a turning point. When computing steady states that are expected to be unstable, the time steps must be adaptively changed while keeping the damped newton iterations. It is crucial to start with small time steps, $10^{-6}$ say, and gradually increase $\Delta t$ to $10^{-2}$. Finally, we note that the time $t$ is used in this context only as an iterative parameter.

### 4.2. Physical parameters

Table 1 lists representative values of physical parameters based on a literature survey; some values required by the model are easier to estimate than others and are obtained from standard thermal property measurements. The table lists values for the constant pressure
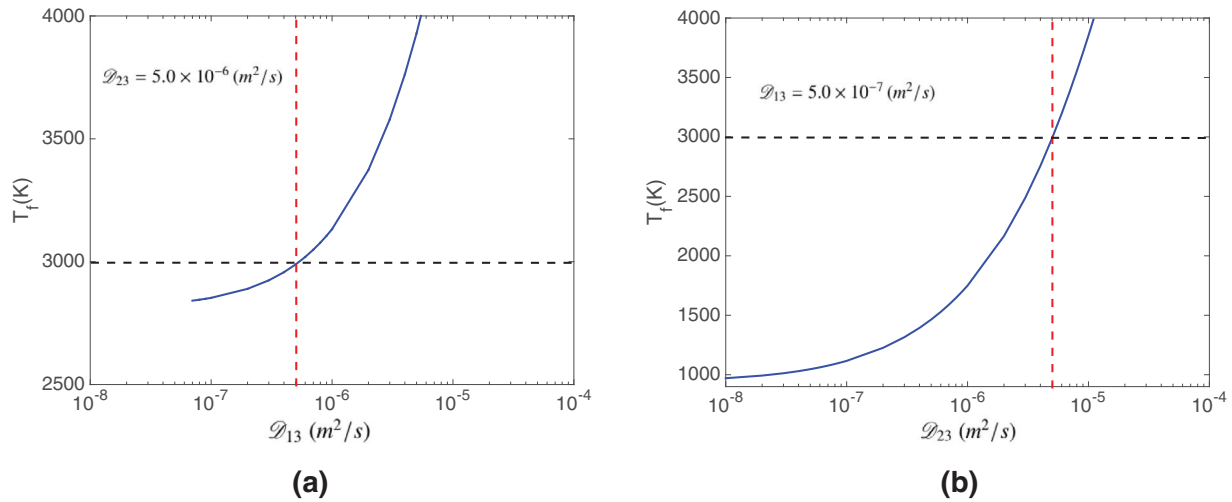
**Fig. 3.** Variation of the adiabatic flame temperature $T_f$ with (a) variations in $\mathscr{D}_{13}$, for given $\mathscr{D}_{23} = 5.0 \cdot 10^{-6}$ m$^2$/s, and (b) variations in $\mathscr{D}_{23}$, for given $\mathscr{D}_{13} = 5.0 \cdot 10^{-7}$ m$^2$/s, relative to base-line values marked by a dashed line.
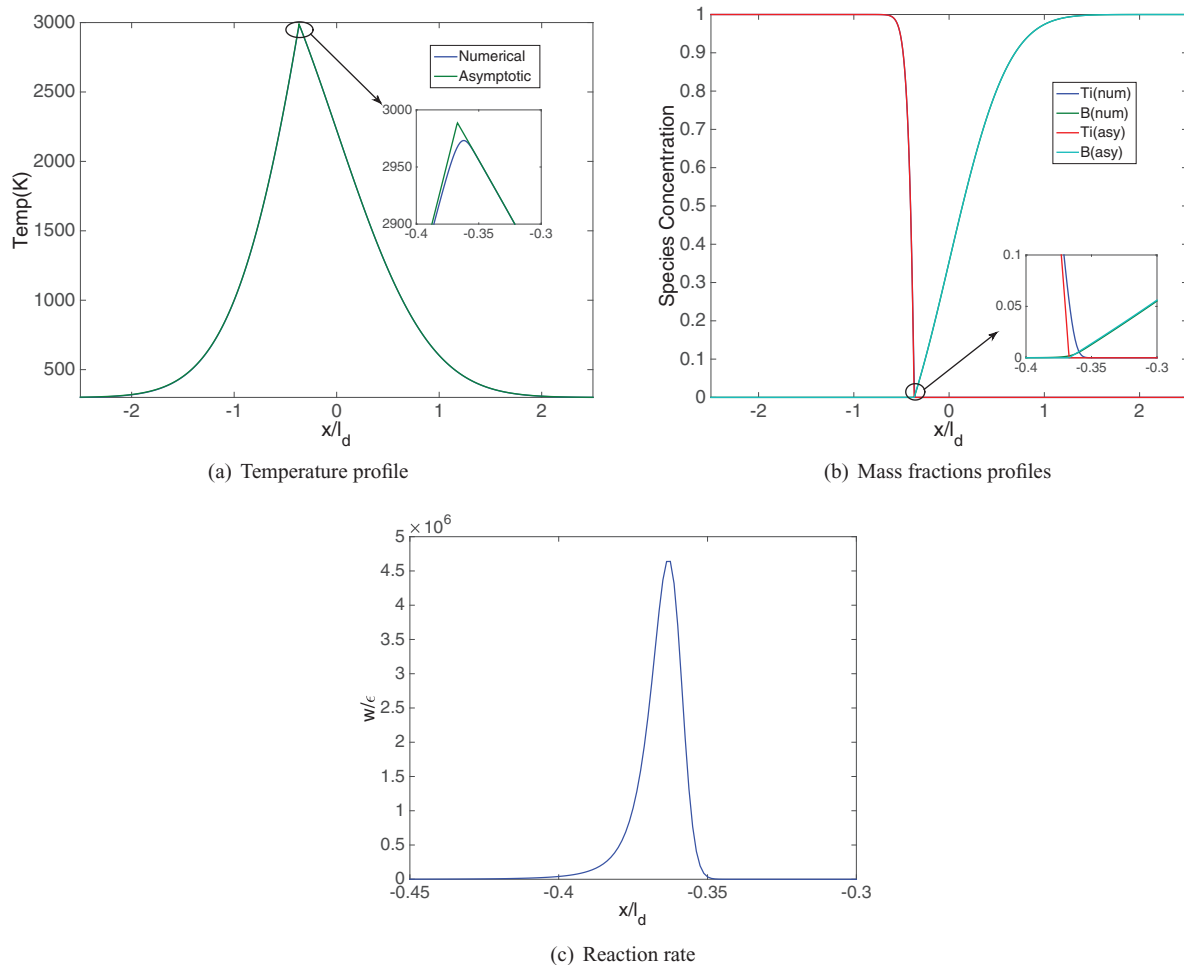


(a) Temperature profile

(b) Mass fractions profiles



(c) Reaction rate

**Fig. 4.** Comparison between the numerical solution and asymptotic solutions for a small strain rate value $\epsilon = 0.01 \, s^{-1}$.

heat capacity, $c_p$, and thermal conductivity, $k$, that represent averaged values for the mixture. However, the determination of the binary mass diffusivities is more problematic. Experimental values for $\mathscr{D}_{13}$ and $\mathscr{D}_{23}$ have been reported [19,20], but not at conditions that are present in the reaction zone. Better estimates could be obtained

from our derived asymptotic expressions, when used in conjunction with experimentally measured flame temperatures.

Trunov et al. [13] measured adiabatic flame temperatures for the titanium–boron reaction of approximately 2400–3300 K. One expects, similar to the values measured experimentally at low
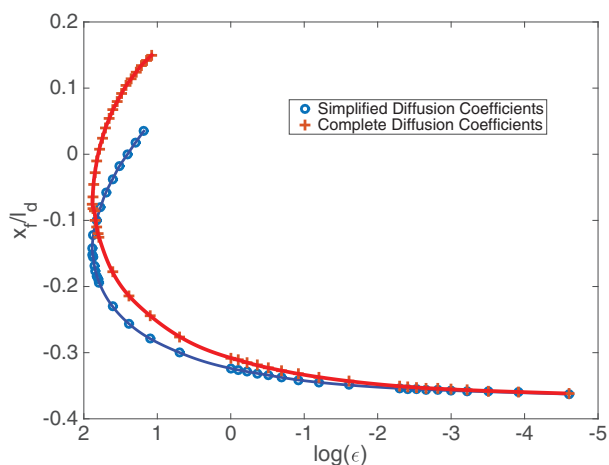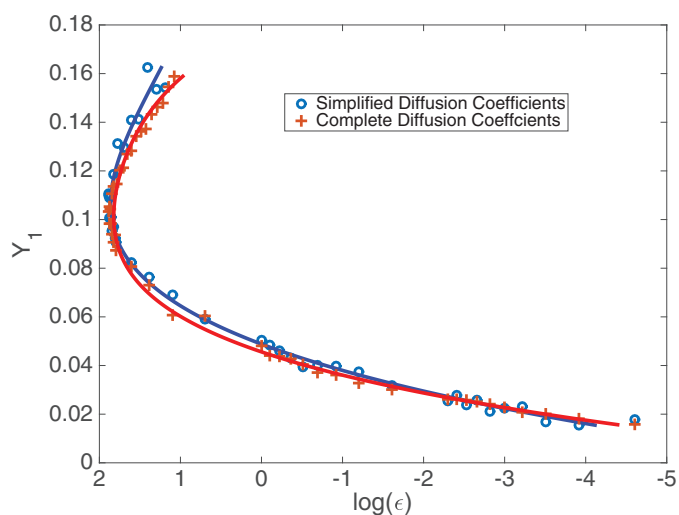
(a) Flame position
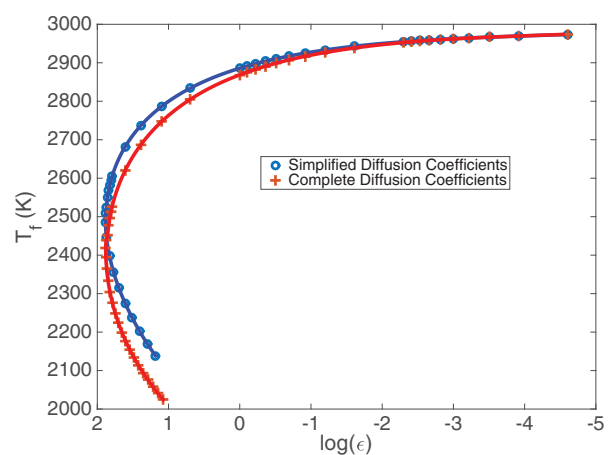


(b) Flame temperature

**Fig. 5.** Response curves of flame position and flame temperature versus strain rate. The two curves (red/blue) correspond to the complete and simplified diffusion formulations. (For interpretation of the references to color in this figure legend, the reader is referred to the web version of this article.)



(a) Unconsumed titanium mass fraction



(b) Unconsumed boron mass fraction

**Fig. 6.** The extent of unconsumed reactants leaking through the reaction zone. The two curves (red/blue) correspond to the complete and simplified diffusion formulations. (For interpretation of the references to color in this figure legend, the reader is referred to the web version of this article.)

temperatures [20], that the binary diffusivities of both, boron and titanium into titanium-diboride, are significantly smaller than the mixture thermal diffusivity, and that $\mathscr{D}_{23} \gg \mathscr{D}_{13}$. Taking $\mathscr{D}_{23}/\mathscr{D}_{13} = 10$ as a base-line model value, and the estimate $T_f = 3000$ K for the flame-sheet temperature, our formulas (33) and (34) yield $\mathscr{D}_{13} \approx 5 \times 10^{-7}$ m$^2$/s and $\mathscr{D}_{23} \approx 5 \times 10^{-6}$ m$^2$/s. Figure 3 shows changes in flame temperature as a result of variations in the binary diffusivities $\mathscr{D}_{13}$ and $\mathscr{D}_{23}$ relative to the base-line values, for the fixed ratio of $\mathscr{D}_{23}/\mathscr{D}_{13}$.
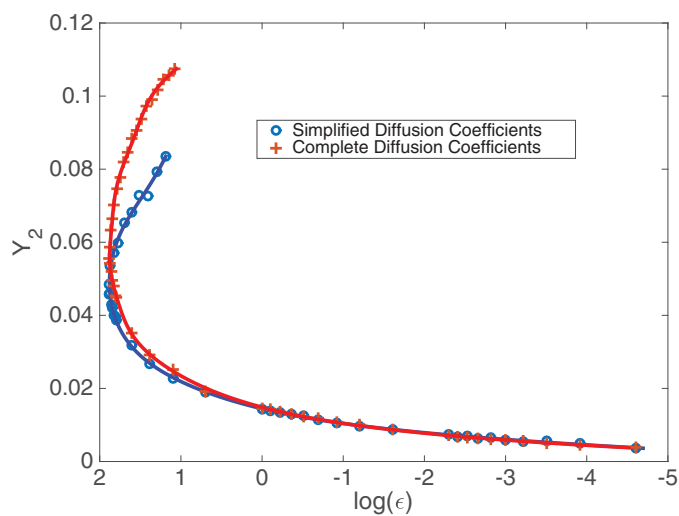
### 4.3. Low strain rates

We start by presenting results pertaining to low strain rates, where the solution can be compared directly to the asymptotic solution discussed above. Since the latter was obtained under the constant density assumption, the average value $\rho = 3.8$ g/cc was selected, abandoning the equation of state (14). The expressions for the diffusion coefficients were used *without* resorting to the approximation of equal molecular weights, since the reduced form of these relations led to nearly identical results.

Figure 4 (a) and (b) shows a comparison of the temperature and mass fraction profiles between the computed solution for $\epsilon = 0.01$ s$^{-1}$ and the corresponding asymptotic expressions. The spatial coordinate is normalized with the thermal diffusion length $l_d = \sqrt{\alpha/\epsilon} = 3.2410^{-4}$ cm. For such low values of strain rate combustion

is nearly complete, with both reactants consumed in a very thin reaction zone. There is excellent agreement between the computed and asymptotic profiles except for very small changes near the reaction zone, as shown in the figure inserts. Evidently, for finite $\epsilon$ however small, the reaction zone has a finite thickness, which is adequately captured by the numerical solution as shown in Fig. 4(c). The excellent agreement between the numerical and asymptotic solutions also serves as a validation of our numerical methodology that properly resolves the stiffness in the governing equations arising from the exponential Arrhenius term.

### 4.4. Moderate strain rates – constant density

Next we consider the entire response of the flame to increasing strain rates, from complete combustion corresponding to low strain rates to flame extinction occurring at significantly higher values of $\epsilon$.

We first examine the solution using two diffusion formulations: the complete expressions for the diffusion coefficients $a_i$, $b_i$, and the simplified form resulting from equal molecular weights. We note that the general diffusion expressions add nonlinearity to an already
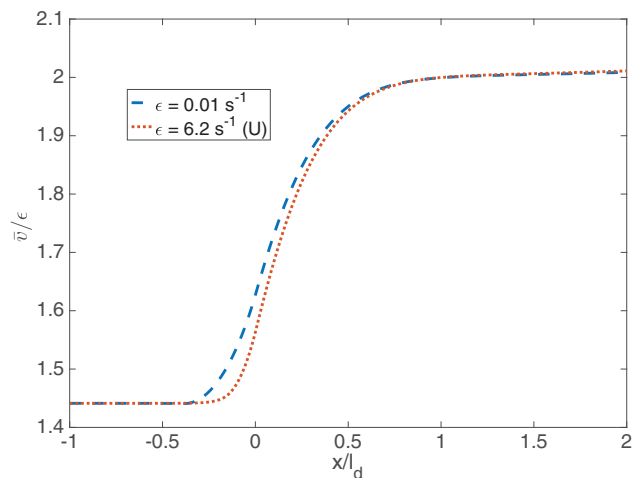
**Fig. 7.** Profiles of the transverse velocity $\bar{v}$ across the combustion zone for two strain rate values.



**Fig. 8.** Density profiles across the combustion zone for two strain rate values.

stiff problem. Therefore, to facilitate the computations we have retained the constant-density approximation in the results presented in this subsection, which effectively decouples the flow and combustion fields; variable density solutions will be presented in the next subsection. Figures 5 and 6 show response curves of various flame characteristics to the imposed strain rate $\epsilon$, based on the two diffusion formulations. These include the flame position $x_f$ (defined as the location where the temperature reaches its maximum value), the flame temperature $T_f$ (the value of $T$ at $x_f$), and the mass fractions of unconsumed titanium and boron (the values of $Y_1$ and $Y_2$ evaluated at $x_f$). We note that the precise evaluation of the flame position, and the temperature and mass fractions evaluated at this location, depend on the step size used in the computations and on the value of the thermal diffusion length $l_d$, which decreases from $3.24 \times 10^{-5}$ cm to $1.3 \times 10^{-6}$ cm as the strain rate increases from $\epsilon = 0.01$ s$^{-1}$ to $\epsilon = 6.5$ s$^{-1}$ (which is very near extinction). A Matlab Curve Fit [29] tool was used to fit the numerical data to a smoothing spline, which was then used for the determination of $x_f$ and for evaluating all properties at this location. The same tool was used to fit smoothing spline curves presented in all the figures, to the discrete data obtained numerically.

From the response curves of Figs. 5 and 6 the following physical picture emerges. Since at low strain rates the chemical reaction time is much shorter than the flow time, the reaction proceeds immediately as titanium and boron get in contact. The reaction occurs in a very thin zone (or a sheet) where both reactants are completely consumed. The flame lies on the titanium side ($x < 0$) and the flame temperature reaches its maximum value. Upon increasing the strain rate, the flow time relative to the chemical reaction time is shortened and a fraction of titanium and boron escape mixing and leaks through the reaction zone. As a result of incomplete combustion, the flame moves towards the boron side and the flame temperature drops. The relatively larger leakage of titanium as opposed to boron stems from the fact that $\mathscr{D}_{13} \ll \mathscr{D}_{23}$, which implies much larger fluxes of boron towards the reaction zone and consequently a more complete consumption of boron. This trend continues until the fraction of unconsumed reactants exceeds a critical threshold and the flame temperature drops significantly from its adiabatic value. For larger values of the strain rate steady burning is no longer possible. The critical state, represented by the turning point on the response curves and corresponding to $\epsilon \approx 6.586$ sec$^{-1}$, identifies conditions associated with flame extinction. The lower branch on the temperature response curve of Fig. 5 and the upper branches in Fig. 6 are typically unstable and therefore physically inaccessible.
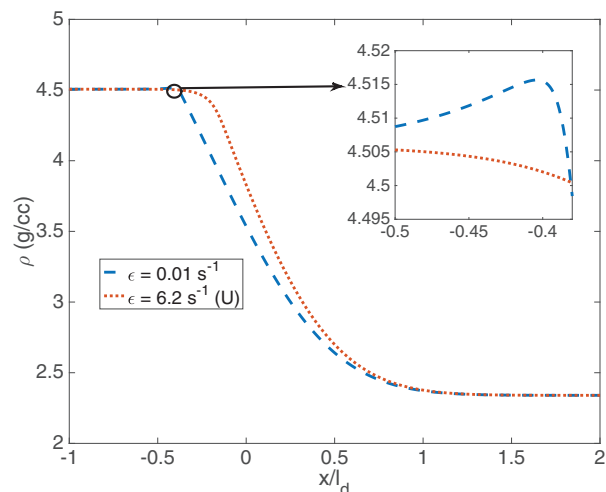


(a) flame psotition
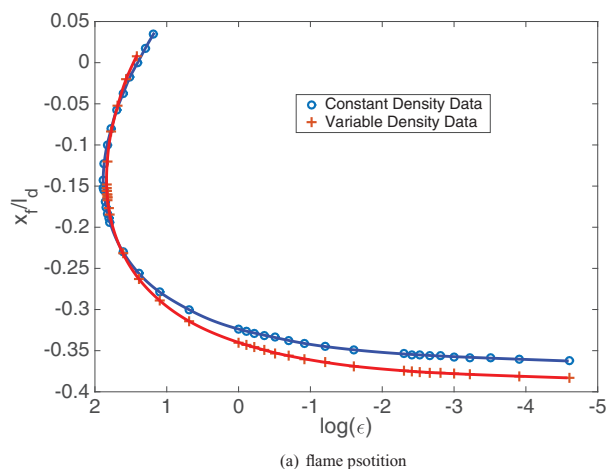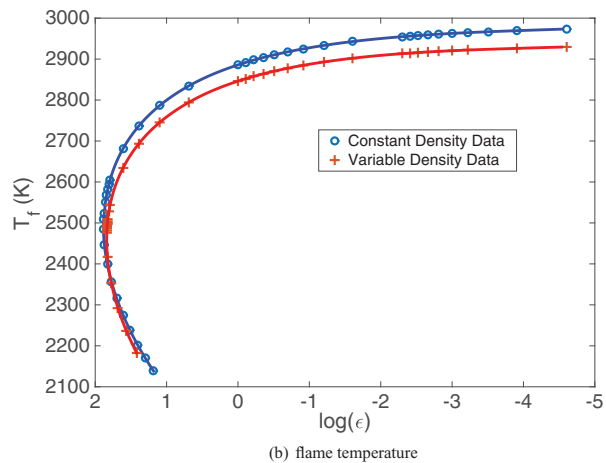


(b) flame temperature

**Fig. 9.** Comparison of flame position and temperature between constant and variable density conditions.

The two diffusion formulations lead to identical results at low strain rates and predict the exact same extinction strain rates. There are small, insignificant differences in flame temperature at and near extinction, which can be traced to the slight difference in flame location. Being influenced primarily by the binary diffusivity $\mathscr{D}_{13} \ll \mathscr{D}_{23}$, the simplified diffusion formulation predicts a flame position that is slightly tilted towards the titanium ($x < 0$) side. Due to the negligible

(a) Unconsumed titanium mass fraction



(b) Unconsumed boron mass fraction

**Fig. 10.** $Y_1$ response curve comparison between constant and variable density approximations.

difference between the two formulations, the simplified diffusion formulation will be used in the following section in order to save computational time.

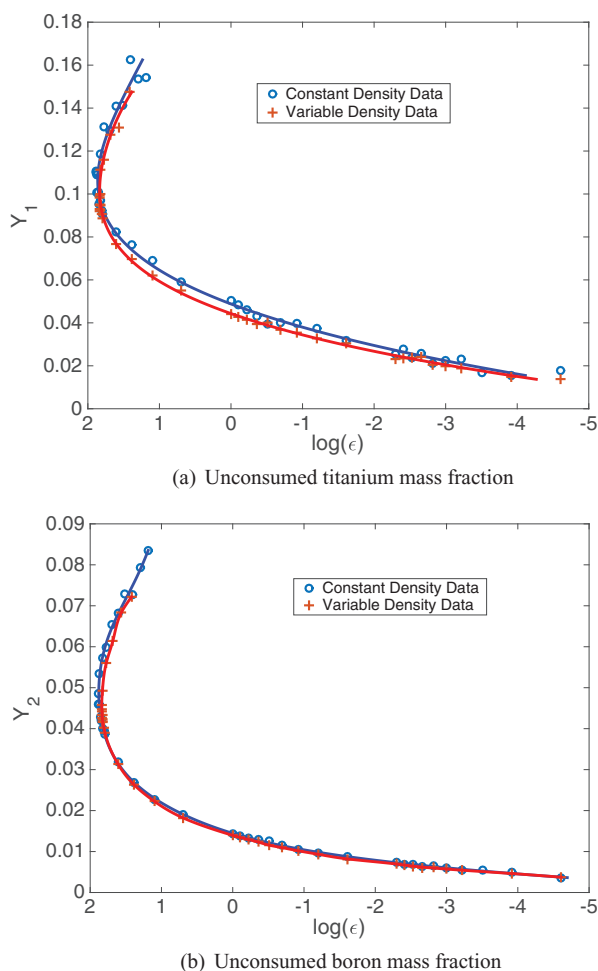### 4.5. Moderate strain rates – variable density

When variations in density are accounted for, the flow field no longer satisfies (19) and must be obtained by solving the momentum Eq. (5) with $\rho$ given by (14). The boundary conditions as $x \to \pm\infty$ imply that $\bar{v}$ tends to a constant on either end, with the asymptotes subject to the constraint (9). Figure 7 shows profiles of $\bar{v}$ computed for two values of $\epsilon$; the low strain rate value corresponding to conditions close to the Burke-Schumann solution and the larger strain rate value corresponding to near-extinction conditions. Variations in $\bar{v}$ across the field are due to density changes, which are more pronounced in the combustion region $-0.5 \lesssim x/l_d \lesssim 0.5$.

Density profiles are shown in Fig. 8 for the same two values of $\epsilon$. Generally, the density would vary from $\hat{\rho}_{1_0} = 4.5$ g/cc on the titanium side to $\hat{\rho}_{2_0} = 2.34$ g/cc on the boron side. Since to the density of TiB$_2$ is slightly higher than that of Ti, there is a noticeable jump in density near the reaction zone at low strain rates (see the figure inset), where the reaction is more vigorous and the production of TiB$_2$ higher. This increase in density diminishes at higher strain rates due to lower TiB$_2$ production and increase of titanium leakage through the reaction zone.

Response curves of flame position and temperature vs strain rates, for constant and variable density conditions, are shown in Fig. 9. The

flame temperature $T_f$ and flame position $x_f$ are consistently higher for the constant density case than for the variable density case, for all values of $\epsilon$. The difference is very small and is of no physical significance, being primarily due to the selected mean density value adopted in the constant density formulation. The small difference between the two solutions indicates that the composition distribution has little effect on the overall density, for practically all strain rate values. The flame temperature at extinction is approximately 2500 K, corresponding to a drop in approximately 500 K from the adiabatic flame temperature $T_f = 2950$ K (or 3000 K for the constant density case). The flame position in the Burke–Schumann limit is determined from the condition that the two separate reactants meet in stoichiometric proportions, with the temperature playing no role in this balance. One may therefore attribute the slight variation in flame position between the constant and variable cases to the dependence of species distribution on the overall density. As with the flame temperature, the predicted values of $x_f$ at extinction by the two formulations is very close, with the difference being less than 0.1%.

In Fig. 10, we show the degree of reactant leakage through the reaction zone for the constant and variable density formulations. In both cases the mass fractions tend to zero at low strain rates, as it should. Elsewhere, the variable density solution shows a slight deviation in the leakage of $Y_1$ and $Y_2$ from the constant density solution. This is more evident for titanium, because the extent of titanium diffusion is much smaller than that of boron causing a sharper response to density variations. The difference between the two solutions at extinction is nearly 0.005 for $Y_2$ and 0.05 for $Y_1$, approximately 10% of the actual extinction values.

### 5. Conclusions

A multi-component mixture theory is used to describe condensed phase diffusive combustion, in particular for titanium-boron reaction in a counterflow geometry. The Maxwell–Stefan model for multi-component mixtures is informed by the binary diffusivities of any pair of species comprising the mixture. Because of the complications arising from the direct use of the Maxwell–Stefan model in combustion studies, a generalized Fick law is often adopted with coefficients, referred to as Fick diffusivities, which are often assumed to be constant. These coefficients, however, are concentration-dependent and could be related to the binary diffusivities via cumbersome expressions. A significant contribution of this work is the derivation of a multi-component diffusion model for a three-component mixture, which reduces to the gaseous model when molecular weights and diffusivities for each species are equal.

The proposed diffusion expressions can be simplified by assuming equal molecular weights. A comparison between the two diffusion models, with equal and unequal molecular weights, has been carried out in the constant density limit (for simplicity of computations). The response curves constructed numerically show that the two diffusion models lead to identical results at large strain rates as expected, and vary by less than 2% near extinction. This suggests that one could safely use the constant molecular weight approximation in the proposed diffusion model with minimal loss in accuracy, while saving computational time and complexity.

Low temperature measurements of the boron-titanium diboride binary diffusivity, $\mathscr{D}_{23}$, fall in the range of $10^{-13}$ to $10^{-20}$ m$^2$/s while the titanium–titanium diboride diffusivity, $\mathscr{D}_{13}$, is three orders of magnitude lower. These diffusivities, however, are unavailable at the combustion temperature of Ti-B nano-composites, measured near 3000 K. The derived expressions of flame position and temperature from the fast-chemistry asymptotic analysis have been used to estimate the aforementioned diffusivities in a manner which is consistent with macroscopically observed adiabatic flame temperatures. These estimates may hold in more general circumstances because, as noted from our simulations the flame temperature drops

only slightly over the entire range of strain rates sustaining steady combustion.

Combustion characteristics at the interface of two condensed phase reactant streams that form an opposed counterflow are represented by a typical S-shaped response curve. In this paper we only address the portion of the S-curve that extends from a vigorous burning state, where the flame temperature reaches its maximum value (the adiabatic flame temperature) and both titanium and boron are completely consumed, down to an extinction state associated with incomplete combustion and with a flame temperature significantly below the adiabatic value. The extinction state is identified when the strain rate reaches a critical value, and for larger strain rates a balance between advection, diffusion and reaction is not possible under steady conditions. The other portion of the S-curve, which extends to exceedingly large values of the strain rate is associated with chemically frozen, or weakly-burning states. Our analysis therefore suggests that in composite materials the distribution of local reaction sites and local frozen sites would depend on the local strain rate distribution.

## Acknowledgments

The relation between the Fick diffusivities $\mathbb{D}_{ij}$ and binary diffusivities $\mathscr{D}_{ij}$ for a ternary mixture are given by

$$\mathbb{D}_{11} = -\frac{\dfrac{(Y_2+Y_3)^2}{X_1\,\mathscr{D}_{23}} + \dfrac{Y_2^{\,2}}{\mathscr{D}_{13}X_2} + \dfrac{Y_3^{\,2}}{X_3\,\mathscr{D}_{12}}}{\dfrac{X_1}{\mathscr{D}_{12}\mathscr{D}_{13}} + \dfrac{X_2}{\mathscr{D}_{12}\mathscr{D}_{23}} + \dfrac{X_3}{\mathscr{D}_{13}\mathscr{D}_{23}}} \tag{40}$$

$$\mathbb{D}_{22} = -\frac{\dfrac{(Y_1+Y_3)^2}{\mathscr{D}_{13}X_2} + \dfrac{Y_3^{\,2}}{X_3\,\mathscr{D}_{12}} + \dfrac{Y_1^{\,2}}{X_1\,\mathscr{D}_{23}}}{\dfrac{X_1}{\mathscr{D}_{12}\mathscr{D}_{13}} + \dfrac{X_2}{\mathscr{D}_{12}\mathscr{D}_{23}} + \dfrac{X_3}{\mathscr{D}_{13}\mathscr{D}_{23}}} \tag{41}$$

$$\mathbb{D}_{33} = -\frac{\dfrac{(Y_2+Y_1)^2}{X_3\,\mathscr{D}_{12}} + \dfrac{Y_1^2}{X_1\,\mathscr{D}_{23}} + \dfrac{Y_2^2}{X_2\,\mathscr{D}_{13}}}{\dfrac{X_1}{\mathscr{D}_{12}\mathscr{D}_{13}} + \dfrac{X_2}{\mathscr{D}_{12}\mathscr{D}_{23}} + \dfrac{X_3}{\mathscr{D}_{13}\mathscr{D}_{23}}} \tag{42}$$

$$\mathbb{D}_{12} = \frac{\dfrac{Y_1(Y_2+Y_3)}{X_1\,\mathscr{D}_{23}} + \dfrac{Y_2(Y_1+Y_3)}{X_2\,\mathscr{D}_{13}} - \dfrac{Y_3^2}{X_3\,\mathscr{D}_{12}}}{\dfrac{X_1}{\mathscr{D}_{12}\mathscr{D}_{13}} + \dfrac{X_2}{\mathscr{D}_{12}\mathscr{D}_{23}} + \dfrac{X_3}{\mathscr{D}_{13}\mathscr{D}_{23}}} \tag{43}$$

$$\mathbb{D}_{13} = \frac{\dfrac{Y_3(Y_2+Y_1)}{X_3\,\mathscr{D}_{12}} + \dfrac{Y_1(Y_2+Y_3)}{X_1\,\mathscr{D}_{23}} - \dfrac{Y_2^2}{X_2\,\mathscr{D}_{13}}}{\dfrac{X_1}{\mathscr{D}_{12}\mathscr{D}_{13}} + \dfrac{X_2}{\mathscr{D}_{12}\mathscr{D}_{23}} + \dfrac{X_3}{\mathscr{D}_{13}\mathscr{D}_{23}}} \tag{44}$$

$$\mathbb{D}_{23} = \frac{\dfrac{Y_2(Y_1+Y_3)}{X_2\,\mathscr{D}_{13}} + \dfrac{Y_3(Y_2+Y_1)}{X_3\,\mathscr{D}_{12}} - \dfrac{Y_1^2}{X_1\,\mathscr{D}_{23}}}{\dfrac{X_1}{\mathscr{D}_{12}\mathscr{D}_{13}} + \dfrac{X_2}{\mathscr{D}_{12}\mathscr{D}_{23}} + \dfrac{X_3}{\mathscr{D}_{13}\mathscr{D}_{23}}} \tag{45}$$

## References

[1] Advanced energetic materials, Committee on Advanced Energetic Materials and Manufacturing Technologies, 2004.
[2] A.S. Rogachev, Exothermic reaction waves in multilayer nanofilms, Russ. Chem. Rev. 77 (1) (2015) 21–37.
[3] T. Weihs, in: K. Barmak, K. Coffey, Fabrication and characterization of reactive multilayer films and foils, in: (eds.) Metallic Films for Electronic, Optical and Magnetic Applications, Structure, Processing and Properties, 2014, pp. 160–243.
[4] D. Adams, Reactive multilayers fabricated by vapor deposition: A critical review, Thin Solid Film 576 (2015) 98–128.
[5] T.P. Weihs, Self-Propogating Reactions in Multilayer Materials, Institute of Physics, 1998.
[6] G.M. Fritz, H. Joress, T.P. Weihs, Enabling and controlling slow reaction velocities in low-density compacts of multilayer reactive particles, Combust. Flame 158 (2011) 1084–1088.
[7] I. Sraj, Numerical simulation of shock initiation of ni/al multilayered composites, J. Appl. Phys. 023515 (2014) 115.
[8] N. Glumac, D.S. Stewart, M.D. Clemenson, S.P. Koundinyan, J.B. Bdzil, J.C. Foster, Shock Actuated Burning of Thermitic and Inter-metallic Reactive Composite Materials in Preparation, Results Presented for Integrated Experimental and Modeling Study of Meso-scale Processes in Reactive Materials, HDTRA-08-10, Defense Threat Reduction Agency Basic Research Technical Review, July 29, 2014.
[9] D. Eakins, N. Thadhani, Mesoscale simulation of the configuration-dependent shock-compression response of Ni + Al powder mixture, Acta Materialia 56 (2008) 1496–1510.
[10] D.R. Gaskell, Introduction to the Thermodynamics of Materials, Introduction to the Thermodynamics of Materials, 5th edition, Taylor and Francis, 2008.
[11] C.F. Curtiss, Symmetric gaseous diffusion coefficients, J. Chem. Phys. 49 (1968) 2917–2919.
[12] C.F. Curtiss, R.B. Bird, Multicomponent diffusion, Ind. Eng. Chem. Res. (1999) 2515–2522.
[13] M.A. Trunov, V.K. Hoffmann, M. Schoenitz, E.L. Dreizin, Combustion of boron-titanium nanocomposite powders in different environments, J. Propuls. Power 24 (2) (2008) 184–191.
[14] J.O. Hirschfelder, C.F. Curtiss, R.B. Bird, Molecular theory of gases and liquids, Molecular Theory of Gases and Liquids, Wiley, 1954.
[15] R. Taylor, R. Krishna, Multicomponent Mass Transfer, Multicomponent Mass Transfer, Wiley, 1993.
[16] R.B. Bird, W.E. Stewart, E.N. Lightfoot, Transport Phenomena, Transport Phenomena, Wiley, 2002.
[17] A. Liñán, The asymptotic structure of counterflow diffusion flames for large activation energies, Acta Astronautica 2 (1974) 1009.
[18] S. Cheatham, M. Matalon, A general asymptotic theory of diffusion flames with application to cellular instability, J. Fluid Mech. 414 (2000) 105–144.
[19] Z. Fan, B. Cantor, The kinetics and mechanism of interfacial reaction in sigma fibre-reinforced ti mmcs, Composites Part A 28A (1997) 131–140.
[20] H. Scmidt, Self-diffusion of boron in titanium diboride, J. Appl. Phys 93 (2) (2003) 907–911.
[21] PETSc, Version 3.4.3, Argonne National Lab, Lemont, IL, 2013.
[22] V. Kurdyumov, M. Matalon, Dynamics of an edge-flame in a mixing layer, Combust. Flame 139 (4) (2004) 329–339.
[23] I. Barin, Thermochemical Data of Pure Substances, Weinheim: VCH, 1995.
[24] O. Madelung, U. Rossler, M. Schulz (Eds.), Boron (b) thermal diffusivity and conductivity, beta-rhombohedral boron, in: Non-Tetrahedrally Bonded Elements and Binary Compounds I, in: Landolt–Bornstein – Group III Condensed Matter, vol. 41C, Springer, Berlin, Heidelberg, 1998, pp. 1–6.
[25] G.K. White, O. Madelung, G.K. White (Eds.), in: Thermal Conductivity of Pure Metals and Alloys, vol. 15c, Springer, 2015.
[26] R. Munro, Material properties of titanium diboride, J. Res. Natl. Inst. Stand. Technol 105 (2000) 709–720.
[27] M. Pacheco, Self-sustained High-temperature Reactions: Initiation, Propagation and Synthesis, Ph.D. thesis, Universidad Carlos III de Madrid, 2007.
[28] N.L. Peterson, Diffusion in Refractory Metals, Technical Report 60-793, Wadd Technical Report, 1960.
[29] MATLAB, version 8.4.0 (R2014b), The MathWorks Inc., Natick, Massachusetts, 2014.
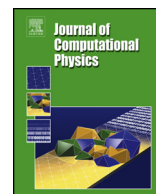
# Modeling of the quenching of blast products from energetic materials by expansion into vacuum

Sungjin Choi [a], D. Scott Stewart [a,*], Sunhee Yoo [b]

[a] *Department of Mechanical Science and Engineering, University of Illinois at Urbana Champaign, IL 60801-2906, USA*
[b] *Jacobs Engineering, Munitions Directorate, Eglin AFB, FL, USA*

## ABSTRACT

Condensed phase energetic materials include propellants and explosives. Their detonation or burning products generate dense, high pressure states that are often adjacent to regions that are at vacuum or near-vacuum conditions. An important chemical diagnostic experiment is the time of flight mass spectroscopy experiment that initiates an energetic material sample via an impact from a flyer plate, whose products expand into a vacuum. The rapid expansion quenches the reaction in the products so that the products can be differentiated by molecular weight detection as they stream past a detector. Analysis of this experiment requires a gas dynamic simulation of the products of a reacting multi-component gas that flows into a vacuum region. Extreme computational difficulties can arise if flow near the vacuum interface is not carefully and accurately computed. We modify an algorithm proposed by Munz [1], that computed the fluxes appropriate to a gas–vacuum interface for an inert ideal gas, and extend it to a multi-component mixture of reacting chemical components reactions with general, non-ideal equations of state. We illustrate how to incorporate that extension in the context of a complete set of algorithms for a general, cell-based flow solver. A key step is to use the local exact solution for an isentropic expansion fan, for the mixture that connects the computed flow states to the vacuum. Regularity conditions (i.e. the Liu–Smoller conditions) are necessary conditions that must be imposed on the equation of state of the multicomponent fluid in the limit of a vacuum state. We show that the Jones, Wilkins, Lee (JWL) equation of state meets these requirements.

© 2015 Elsevier Inc. All rights reserved.

## 1. Introduction

Condensed phase energetic materials include propellants and explosives. They are usually composed of a mixture of granular solids that include explosive or oxidizing crystallites, various metal powders like aluminum, sometimes carbon black, resins and plastics. The performance of the aggregate composite depends on the chemistry and the mechanisms of energy release, which occur in nearly all phases of materials, gas, liquid and solid. Propellant and explosives reactive decomposition produces huge volume expansion. The products start at near solid densities and at high pressures and expand to very low densities and lower pressures. In the case of explosives, the pressure drops from hundreds of kilo-bars to 1 atmosphere or less, which is 5 to 6 orders of magnitude across a reaction zone that is often no more than 1/10 of a
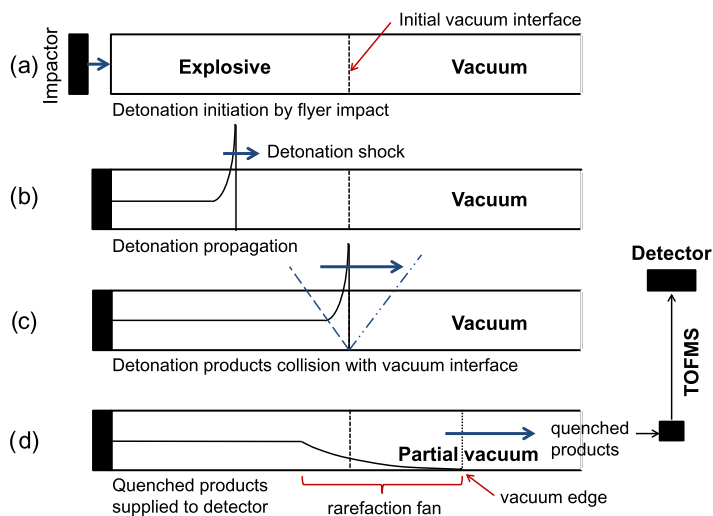
---

**Fig. 1.** The schematic diagram of numerical simulation of initiation, detonation and expansion for an explosive sample in the TOFMS experiment.

millimeter thick. This enormous pressure gradient provides the means to cut materials or drive surrounding materials to large velocities by virtue of this expansion power. Likewise, solid propellants in rocket motors vent gases with pressures that range from 1 to 200 atmospheres, down to vacuum conditions. Many orders of magnitudes of pressure change are realized and the pressure gradient in propellant exhaust stream provides the means to generate thrust. The problem of computing the transition of material states from very high pressure to vacuum or near vacuum states is a generic one for any multi-material simulation where two materials may collide and have individual or shared boundaries, for which one of the materials is adjacent to a region with very low pressure and density or a vacuum. Difficulties generally arise if the region of expansion between the high and low pressure regions is not accurately computed.

A time of flight mass spectrometry (TOFMS) experiment by Fossum et al. [2], initiated small samples of energetic materials by laser flyer plate impact. After impact, the products expanded into a vacuum region where spectroscopic analysis of the products was performed. A larger version of a similar experiment was carried out by Blais et al. [3] that used a large quantity of explosive to drive an ampule of nitromethane, which detonated upon being shocked. The premise of the TOFMS experiments is that the pressure drop caused by the expansion in a long vacuum region freezes/quenches the reaction amongst product species in a sequential manner, ordered by the events in the reaction zone in the material that was established prior to the expansion. In order to interpret TOFMS experiments, accurate model simulations of the gas dynamics of reacting multi-component mixtures are required. The range of thermodynamic states is extreme. The reactants start at standard room pressure and temperature conditions, are raised to high pressure, density detonation or highly shocked states in condensed materials, convert to (mostly) gas species products that expand to a vacuum or near-vacuum state. Such simulations are very challenging to carry out since non-ideal equations of state forms must be used for the reactants and products, and the location of the vacuum/materials boundary must be calculated in a precise manner.

Computational methods and techniques are not widely available for multi-component reactive flow, when the components are subjected such huge ranges in the thermodynamics states. Since we had an interest in finding an accurate and robust way to simulate the TOFMS experiments, we decided to make a modification to the basic vacuum interface tracking algorithm pioneered by Munz [1]. Our extension is used in combination with a (now) standard, higher order, cell-based, totally variation diminishing (TVD) Euler scheme, in a fairly general multicomponent framework. One should be able to use our method to compute the approach to the vacuum in the continuum limit, and combine it with simulations of the Boltzmann equation or with molecular dynamic simulations. The continuum simulations we describe would generate the near vacuum continuum flows as a far-field limit, or be used to establish averaged initial conditions for molecular based simulations. In this paper, we describe these algorithms and implementations in detail, and present worked examples that simulate the flow in the TOFMS experiment as a targeted application.

Fig. 1 shows a sketch of a typical sequence of events that occur in a simulation of the quenching of blast products that expand into a vacuum region on the right. a) The explosive sample and vacuum regions are initially separated, prior to impact by the flyer. b) If the sample detonates, a detonation shock and its supporting reaction zone propagate through the explosive. c) The detonation wave hits the vacuum interface. d) Then a rarefaction travels back into the detonation reaction zone structure. As the pressure and density drop, the reactions amongst product species slow as the products flow into the vacuum section, past the detector which monitors the mass concentration of the products at a fixed probe locations. Since the number density drops in the vacuum region, the species are thought not to undergo significant collisions and hence no further chemical changes occur.

### 1.1. Summary of the algorithms

The original work of Munz [1] proposed an approximation method that computes the fluxes, appropriate to the gas–vacuum interface, and tracked the motion of the gas–vacuum boundary for an inert ideal gas. Our extended algorithm allows for reactive flow with general, non-ideal equation of state (EOS) in Mie–Gruneisen (MG) form for a reacting multi-component mixture, adjacent to a vacuum interface. The formulation can be used to include an arbitrary number of chemical components or other state variables like porosity or particulate density, that could be included in the constitutive description. Our standard multi-component flow model has only one material velocity for the mixture. The corresponding gas dynamics formulations have only forward, backward acoustic characteristic and one material characteristic. The exact form of the vacuum Riemann problem can thus be handled in a standard and familiar way, albeit with complexities associated with the EOS that we describe in some detail. We note that Lee et al. [4] recently considered the Riemann problem for the MG EOS in their analysis of difficulties associated with contact discontinuities.

The extended vacuum tracking algorithm is described in the context of other supporting methods and solver algorithms. We use a cell-based reactive Euler solver that employs local cell-based Riemann problems for general EOS to compute the cell edge fluxes. Roe-average fluxes are used in the manner originally developed by Glaister [5], and extended by Xu [6], and Xu, Aslam and Stewart [7] for chemically reacting species. The reactive Euler equations are solved by source splitting with the first update as a solution to the Euler equations without source term, followed by an update of the (chemical) source terms. We will reference to the first update as the *hydrodynamic update* and the second update as the *source term update*. We have used 5th order Weighted Essentially Non Oscillatory (WENO) with 3rd order Runge–Kutta (RK) for the hydrodynamic update. Updates to the location and velocity of vacuum interface of material, and the special cell boundary flux calculations, use the extensions to the Munz [1] tracking scheme. We have verified our schemes against various examples found in the literature [1,5,8].

Care must be taken to accurately integrate the chemical source terms, because the rates in most kinetics schemes widely vary and can have both fast and slow time scales that are disparate. Colella et al. [9] were amongst the first to point this out for Arrhenius kinetics, applied to the calculation of gas-phase reacting flow. In this case it was advantageous to analytically integrate an approximate form of the source terms across a time step. However source term splitting treatments have been proven to work well (dating back to Colella's original work) and are known to have good stability properties. In his thesis Xu [6] demonstrated that an algorithm of the same type we use here for non-ideal EOS forms, was second order accurate.

If one uses an inaccurate numerical method for the basic hydrodynamic solver, significant problems arise from inaccuracies in the evaluation of the sound speed $c = \sqrt{\partial p / \partial \rho|_s}$ in the vicinity of the vacuum region, in which case tracking the vacuum material interface becomes difficult or breaks down. Therefore in order to compute the flux state and velocity of the vacuum material interface, we work out the exact form of the isentropic expansion fan that vents to the interface. This connects the vacuum state to the state in the adjacent cell, and thus supplies the combined method with a physically accurate value for the vacuum interface velocity. Since we allow for general equation of state, we must insist that the limiting behaviors of the EOS forms are such that the vacuum/material interface problem is well-posed. Fortunately, the conditions that define a well-posed vacuum Riemann problem (VRP) have been considered by Liu and Smoller [10] and they provide criteria on limiting functional form of the EOS as the material expands to the vacuum state of zero mass density. These conditions must be incorporated into the vacuum interface tracking method. We show that the Jones, Lee, Wilkins (JWL) EOS form, commonly used for product components, satisfies these conditions.

### 1.2. Paper outline

Section 2 describes basic model formulations that include the conservation laws, the mixture equation of state for a multi-component mixture with commonly used EOS forms for the components, that include ideal gas EOS forms and Mie–Gruneisen EOS forms. Details are given for the JWL EOS form for reactant and product components. Details for two component mixture closures are given. One is the standard pressure–temperature equilibrium closure (PT-EQB), and the other is an often-used, simpler, pressure equilibrium closure (P-EQB), that specifies a volume ratio between the components (instead of enforcing strict temperature equilibrium). Section 3 describes the numerical methods, with a brief review of basic methods for the compressible Euler equations. A brief description of the Riemann solver for general EOS is given followed by the detailed discussion of the implementation of the vacuum tracking method for a general EOS in a reactive flow. Section 4 presents examples and applications. The first example describes a condensed explosive with ideal gas EOS forms for both the reactants and products. This is followed by a detailed simulation of a facsimile of the TOFMS experiment where a thin sample of PETN is hit by an impactor and whose products are vented into the long vacuum region of the experiment. The components are modeled with non-ideal MG EOS forms. We also discuss the sensitivity of the simulation results to the different mixture closure conditions, pressure, temperature equilibrium (PT-EQB) and pressure equilibrium (P-EQB).

## 2. Basic model formulations

Here we give the formulations for the physical models of interest. The models apply to a mixture of compressible fluids with $N$ distinct species. The fluid mixture is assumed to have a single mixture material velocity $u$, pressure $p$, and generally a single temperature $T$ (although that is not strictly required). Each species will be assumed to be specified by its separate

equation of state, and the mixture energy that is used to define the equilibrium potentials will neglect mixing terms, that can sometime be included in the theory of liquid mixtures. Hence the mixture is ideal, although the equation of state (EOS) forms are not necessarily those of the ideal gases. We assume that the EOS forms provided by the model allow for a continuous and smooth approach to zero density, i.e. to the vacuum state. That will allow us to calculate reasonable mixture velocities and track the location of vacuum material interface. It is understood that the continuum limit breaks down at a true vacuum and the model only predicts some limiting approximation (from the continuum limit side) of the states near the material/vacuum interface. The description of the transition to vacuum on the molecular scale requires the implementation of additional models, that are not the subject of this work. Thus the flow simulations as shown in the section for examples are restricted to extremely low but non-zero densities, where the continuum approximations are still reasonable.

## 2.1. The governing equations

It is useful to present all three forms of the governing equations, the primitive, conservation and characteristic forms. The basic numerical scheme in the body of the fluid uses the conservative form, while the vacuum interface approximation require the characteristic form. The primitive form of the governing conservation laws for mixture mass, momentum, energy, and mass fraction of identified chemical species are respectively

$$\dot{\rho} + \rho \nabla \cdot \boldsymbol{v} = 0 \,, \tag{1}$$

$$\rho \, \dot{\boldsymbol{v}} = -\nabla p \,, \tag{2}$$

$$\rho \dot{e} + p \nabla \cdot \boldsymbol{v} = 0 \,, \tag{3}$$

$$\rho \dot{\lambda}_i = r_{\lambda_i} \,, \tag{4}$$

where we use the "dot" notation is used for the material derivative $\dot{(\,)} = \partial/\partial t + \boldsymbol{v} \cdot \nabla$. The variables $\rho = 1/v$, $e$, $\boldsymbol{v}$ and $\lambda_i$ are the mixture density (its reciprocal, specific volume), specific internal energy, mixture velocity and mass fraction of the $i$th-species respectively. The one-dimensional conservative form of the Euler equations for reactive flow in the multi-component mixture (illustrated for two independent components/reactions, $\lambda_1$, $\lambda_2$) are:

$$\frac{\partial \mathbf{U}}{\partial t} + \frac{\partial \mathbf{F}(\boldsymbol{U})}{\partial x} = \mathbf{S}(\mathbf{U}) \tag{5}$$

$$\mathbf{U} = \begin{bmatrix} \rho \\ \rho u \\ \rho E \\ \rho \lambda_1 \\ \rho \lambda_2 \end{bmatrix} \quad \mathbf{F} = \begin{bmatrix} \rho u \\ \rho u^2 + p \\ (\rho E + p)u \\ \rho u \lambda_1 \\ \rho u \lambda_2 \end{bmatrix} \quad \boldsymbol{S} = \begin{bmatrix} 0 \\ 0 \\ 0 \\ \rho r_{\lambda_1} \\ \rho r_{\lambda_2} \end{bmatrix} , \tag{6}$$

and

$$E = e + \frac{1}{2}u^2 \,. \tag{7}$$

Riemann problems and the methods for solving these hyperbolic equations are based on the characteristic form of the equations which we list below in one spatial dimension, $x$

$$\frac{\partial p}{\partial t} + (u+c)\frac{\partial p}{\partial x} + \rho c \left[ \frac{\partial u}{\partial t} + (u+c)\frac{\partial u}{\partial x} \right] = \rho c^2 (\boldsymbol{\sigma} \cdot \boldsymbol{r}) \,, \tag{8}$$

$$\frac{\partial p}{\partial t} + (u-c)\frac{\partial p}{\partial x} - \rho c \left[ \frac{\partial u}{\partial t} + (u-c)\frac{\partial u}{\partial x} \right] = \rho c^2 (\boldsymbol{\sigma} \cdot \boldsymbol{r}) \,, \tag{9}$$

$$\frac{\partial p}{\partial t} + u\frac{\partial p}{\partial x} - c^2 \left( \frac{\partial \rho}{\partial t} + u\frac{\partial \rho}{\partial x} \right) = \rho c^2 (\boldsymbol{\sigma} \cdot \boldsymbol{r}) \,, \tag{10}$$

$$\frac{\partial \lambda_i}{\partial t} + u\frac{\partial \lambda_i}{\partial x} = r_{\lambda_i} \,. \tag{11}$$

The sound speed $c^2$ and the thermicity $\boldsymbol{\sigma} \cdot \boldsymbol{r}$ are given by

$$c^2 = \frac{(\frac{\partial e}{\partial v}|_{p,\lambda_i} + p)v^2}{\left( \frac{\partial e}{\partial p}|_{v,\lambda_i} \right)} \quad \text{with} \quad \sigma_i = \frac{1}{\rho c^2} \frac{(\partial e/\partial \lambda_i)|_{p,v}}{(\partial e/\partial p)|_{v,\lambda_i}} \quad \text{and} \quad \boldsymbol{\sigma} \cdot \boldsymbol{r} = \sum_i^N \sigma_i r_{\lambda_i} \,, \tag{12}$$

respectively, and where the specific internal energy is of the form $e(p, v, \lambda_i)$. The equations above, written as ordinary differential equations on their respective characteristics, are given by

$$\frac{dp}{dt} + \rho c \frac{du}{dt} = \rho c^2 (\boldsymbol{\sigma} \cdot \boldsymbol{r}) \quad \text{on } C_+ : \quad \frac{dx}{dt} = u + c \,, \tag{13}$$

$$\frac{dp}{dt} - \rho c \frac{du}{dt} = \rho c^2 (\boldsymbol{\sigma} \cdot \boldsymbol{r}) \quad \text{on } C_- : \quad \frac{dx}{dt} = u - c \,, \tag{14}$$

$$\frac{dp}{dt} - c^2 \frac{d\rho}{dt} = \rho c^2 (\boldsymbol{\sigma} \cdot \boldsymbol{r}) \quad \text{on } C_0 : \quad \frac{dx}{dt} = u \,, \tag{15}$$

$$\frac{d\lambda_i}{dt} = r_{\lambda_i} \quad \text{on } C_0 : \quad \frac{dx}{dt} = u \,. \tag{16}$$

## 2.2. Mixture equation of state

We assume that the fluid mixture is comprised of $N$ chemical components. A complete equation of state is supposed to be given for each component (species). One can suppose that a Gibbs free energy form is provided for each component that specifies that energy at a fixed temperature and pressure in the form $g_i(p, T)$, which is a complete equation of state, Callen [11], from which we can write the specific internal energy and pressure, volume temperature equation of states, in the form

$$e_i(p, v_i) \quad \text{and} \quad v_i = v_i(p, T) \,. \tag{17}$$

The internal energy and volume are extensive thermodynamic quantities, so the contribution from each component add in a fixed volume of mixture in proportion to the relative masses of the components. Additional contributions due to the intermolecular mixing are neglected. If the mass fraction of each component is $\lambda_i$, then the specific energies and the volumes of the mixture can be written as the sums

$$e(p, T; \lambda_i) = \sum_{i=1}^{N} e_i(p, v_i(p, T))\lambda_i \quad \text{and} \quad v(p, T; \lambda_i) = \sum_{i=1}^{N} v_i(p, T)\lambda_i \,, \tag{18}$$

with $\sum_{i=1}^{N} \lambda_i = 1$. For fixed mixture energy and volume and internal composition, the first and second equation of Eq. (18) are implicit equations for the pressure and temperature, $(p, T)$.

We require the regularity conditions on the equation of state, called the Liu–Smoller conditions (see [10]), when the density approaches to zero density on an isentrope. The pressure relations modeled by the mixture EOS (18) should satisfy

$$p(0) = 0, \quad \frac{\partial p(0)}{\partial \rho}|_s = 0, \quad \text{and} \quad \frac{\partial p}{\partial \rho}|_s > 0, \quad \frac{\partial^2 p}{\partial \rho^2}|_s > 0 \quad \text{for} \quad \rho > 0 \,. \tag{19}$$

In order to model a particular energetic or explosive material, one must identify all the components and their EOS forms for each component. The ideal gas EOS form is often used in detonation theory, [12], and is also the EOS form that was used by Munz to establish his original vacuum tracking algorithm. We describe those common EOS forms next.

### 2.2.1. Ideal gas EOS forms for the components

When all the components are specified by the ideal EOS form with constant specific heats of formation, we write

$$e_i = \frac{1}{\gamma_i - 1} p v_i + e_{i0} \,, \tag{20}$$

where $\gamma_i = c_{pi}/c_{vi}$ (the ratio of specific heats) and $e_{i0}$ is the heat of formation of the $i$-th component. We also use the notation $\omega_i \equiv (\gamma_i - 1)$. The component gas constant is $R_i = c_{vi}(\gamma_i - 1)$, and the $p$, $v_i$, $T$ EOS is given by

$$p v_i = R_i T \tag{21}$$

The mixture energy and mixture volume are given by

$$e = p \sum_i \frac{v_i}{\gamma_i - 1} \lambda_i + \sum_i e_{i0} \lambda_i \,, \quad \text{and} \quad v = \frac{T}{p} \sum_i R_i \lambda_i \,. \tag{22}$$

The first part of Eq. (22) can also be written as

$$e = \left( \sum_i c_{vi} \lambda_i \right) T + \sum_i e_{i0} \lambda_i \,. \tag{23}$$

### 2.2.2. A Mie–Gruneisen EOS form for components

A $e(p, v)$ form of Mie–Gruneisen (MG) EOS for components is explicitly linear in the pressure $p$ and generally nonlinear in the specific volume, and can be written (dropping the $i$-subscript temporarily) as

$$e(p, v) = e^s(v) + \frac{v}{\Gamma}(p - p^s(v)) \equiv A(v) + G(v)p \tag{24}$$

The functions $e^s(v)$, $p^s(v)$, and $v/\Gamma$ are functions that are determined from EOS calibration experiments. Often $e^s(v)$ and $p^s(v)$ are identified as the internal energy and pressure at reference states on some specified, well-identified and measurable thermodynamic process, such as the states on a $p, v$ expansion isentrope, or a shock Hugoniot. Here they are simply regarded as known functions of the specific volume, $v$. The Mie–Gruneisen coefficient $\Gamma$ is often assumed to be a constant or simply a function of $v$. We note that the ideal EOS forms are in this MG class, so the MG forms are inclusive of the ideal EOS forms.

### 2.2.3. The Jones, Lee, Wilkins (JWL) EOS form for components

The Jones, Lee, Wilkins (JWL) EOS form for components is in the MG class, and is probably the most commonly used EOS form for engineering studies of reactive flow in explosives. For example, the chemical equilibrium code Cheetah [13] automatically generates JWL equation of state for reaction products. The JWL EOS forms are often paired with the "Ignition and Growth" reaction rate models that were pioneered by Lee and Tarver [14]. Many highly used explosive compounds such as HMX, RDX, PETN, TATB, TNT, etc. are modeled with MG EOS forms, paired with Ignition and Growth kinetic rate models that describe the rate of overall decomposition from reactants to products.

A standard convention is to use a lower case letter for specific internal energy (as in $e$) and a upper case letter for energy per unit volume $E$. An upper case $V$ to represent the specific volume ratio relative to a reference volume (as in $V = v/v_0$). Then for each component the JWL and thermal EOS is given by

$$p = A_i \exp^{-R_{1i} V_i} + B_i \exp^{-R2i V_i} + \frac{\omega_i C_{vi}}{V_i} T \quad \text{with} \quad V_i = \frac{v_i}{v_0}, \tag{25}$$

and the JWL EOS form are given by the $e(p, v_i)$ mechanical EOS given by

$$E_i = E_i^s(V_i) + \frac{V_i}{\omega_i}\left[p - p_i^s(V_i)\right] + E_{0i}, \tag{26}$$

with

$$E_i^s(v) = \left(\frac{A e^{-R_{1i} V_i}}{R_{1i}} + \frac{B e^{-R_{2i} V_i}}{R_{2i}}\right) \quad \text{and} \quad p_i^s(V_i) = \left(A_i e^{-R_{1i} V_i} + B_i e^{-R_{i2} V_i}\right). \tag{27}$$

With $e_i = E_i v_0$ one has

$$e_i = e_i^s(v_i) + \frac{v_i}{\omega_i}\left[p - p_i^s(v_i)\right] + e_{0i}, \tag{28}$$

with $e_i^s(v_i) = E_i^s v_0$. The constants $A_i$, $B_i$, $R_{1i}$, $R_{2i}$, $\omega_i$ and $C_{vi} \equiv c_{vi}/v_0$ are the JWL component EOS constants; $e_{0i}$ is the reference energy and $v_0$ is a standard reference volume of the original, unshocked mixture.

### 2.2.4. A mixture EOS of reactant and product components for the JWL EOS forms

Next suppose we specify that the mixture is composed of only two species/components reactants (R) and products (P). Both are assumed to be modeled by the JWL EOS forms. The material decomposes by the reaction $R \rightarrow P$, during which the reactant and product are assumed to be in pressure and temperature equilibrium. The product mass fraction is taken be $\lambda$ while the reactant mass fraction be $1 - \lambda$. An $R$ subscript is used to denote reactant and $P$ for product. Given the energy $e$ and a mixture volume $v$, the constraints (18) become

$$e = \lambda e_P(p, v_P(p, T)) + (1 - \lambda) e_R(p, v_R(p, T)), \tag{29}$$

$$v = \lambda v_P(p, T) + (1 - \lambda) v_R(p, T). \tag{30}$$

Since the JWL forms (25) and (26) are not generally linear in the specific volume, the volume dependence is implicit in $p, T$. Given specified values for $e$, $v$, $\lambda$, Eqs. (30) and (29) are two equations for $p$ and $T$. The solution completes the EOS description for the mixture, and defines the PT-EQB closure. There are many ways to find the roots but all involve an iteration to find roots of a pairs (or $n$-tuples) of equations. For the specific choice of the MG, JWL EOS forms for two components, the problem of finding the $(p, T)$ root pairs can be reduced to a single scalar unknown. Next we present a simple robust algorithm that can be used to find the roots.

### 2.2.5. Determination of the $(p, T)$ (Gibbs) equilibrium states

We present a simple way to compute the PT-EQB for JWL EOS forms, that can be used for $N$ components; illustrated for three that can be extended simply to $N$. The mechanical and thermal EOS forms can be represented as

$$e_i(p, v_i) \quad \text{and} \quad p = p(v_i, T),$$

for some fixed temperature and pressure, where $e_i$, $v_i$ are the specific energy and volume for that component. The mixture energy and volume are represented as a sum over the components

$$e = \lambda_1 e_1 + \lambda_2 e_2 + \lambda_3 e_3, \quad \text{and} \quad v = \lambda_1 v_1 + \lambda_2 v_2 + \lambda_3 v_3. \tag{31}$$

Use $v_1$ as a reference volume and define the component volume ratios

$$\Phi_2 = v_2/v_1 \quad \text{and} \quad \Phi_3 = v_3/v_1 , \tag{32}$$

which combined with the second equation in Eq. (31) solves for the component volumes in term of the mixture volume and the ratios, to obtain

$$v_1 = \frac{v}{\lambda_1 + \lambda_2\Phi_2 + \lambda_3\Phi_3} , \quad v_2 = \frac{v\Phi_2}{\lambda_1 + \lambda_2\Phi_2 + \lambda_3\Phi_3} , \quad v_3 = \frac{v\Phi_3}{\lambda_1 + \lambda_2\Phi_2 + \lambda_3\Phi_3} . \tag{33}$$

Using the forms (28) for $e_i$ in (31) obtains

$$e = p \sum_i \frac{v_i}{\omega_i}\lambda_i + \sum_i [e_i^s(v_i) - \frac{v_i}{\omega_i}p_i^s(v_i)]\lambda_i + \sum_i e_{i0}\lambda_i . \tag{34}$$

Solving for $p$ gives

$$p = \left[ e - \sum_i [e_i^s(v_i) - \frac{v_i}{\omega_i}p_i^s(v_i)]\lambda_i - \sum_i e_{i0}\lambda_i \right]/[\sum_i \frac{v_i}{\omega_i}\lambda_i] . \tag{35}$$

The pressure is now explicitly determined by direct evaluation once the mixture energy $e$ and the volume ratios $\Phi_2$, $\Phi_3$ are known. Thus one needs two (2) residuals to determine the correct values of $\Phi_2$ and $\Phi_3$. Those residuals come from setting the temperature of the component (species) equal. For the case of three components there are two such equivalences, i.e. $T \equiv T_1 = T_2$, and $T_2 = T_3$. For $N$ components there are $N-1$ volume ratios and, likewise $N-1$ temperature equivalences. For the 3-component case, with the JWL, MG forms, these equivalences are

$$T = \frac{1}{C_v^1}\frac{V_1}{\omega_1}\left[p - \left(A_1 e^{-R_1^1 V_1} + B_1 e^{-R_2^1 V_1}\right)\right] = \frac{1}{C_v^2}\frac{V_2}{\omega_2}\left[p - \left(A_2 e^{-R_1^2 V_2} + B_2 e^{-R_2^2 V_2}\right)\right] , \tag{36}$$

$$T = \frac{1}{C_v^3}\frac{V_3}{\omega_1}\left[p - \left(A_3 e^{-R_1^3 V_3} + B_3 e^{-R_2^3 V_3}\right)\right] = \frac{1}{C_v^2}\frac{V_2}{\omega_2}\left[p - \left(A_2 e^{-R_1^2 V_2} + B_2 e^{-R_2^2 V_2}\right)\right] , \tag{37}$$

recast as the pair

$$\frac{1}{C_v^1}\frac{V_1}{\omega_1}\left[p - p_1^s(V_1)\right] = \frac{1}{C_v^2}\frac{V_2}{\omega_2}\left[p - p_2^s(V_2)\right] , \quad \frac{1}{C_v^3}\frac{V_3}{\omega_3}\left[p - p_3^s(V_3)\right] = \frac{1}{C_v^2}\frac{V_2}{\omega_2}\left[p - p_2^s(V_2)\right] , \tag{38}$$

that defines the two residuals. For a two component case only one residual is required.

The roots are determined by the following steps. 1) Specify the mixture values of $v$ and $e$ and the reaction progress variables, $\lambda_i$. 2) Make an initial guess for $\Phi_2$ and $\Phi_3$ (say) and then the values of the component volumes (for the example: $v_1$, $v_2$ and $v_3$ are computed. 3) Then the residuals defined by Eq. (38) can be evaluated. 4) Iterate using the residuals to find the root. Any reasonable root procedure can be used. Newton–Raphson works well and converges in a few steps. In special cases direct searches can be used. The initial guess for the volume ratios are usually determined from the previous (time step) physical state, so good quality initial guesses are in abundance. The convergence of the root finding procedure then determines all the component ratios, which in turn can be used to directly compute the pressure from (35) and temperature from (36) or (37).

## 3. Numerical methods

### 3.1. The Euler solver

A typical numerical solution of our equations would use operator splitting that updates a discrete approximation to the source free Euler equations, followed by an update of the source terms. The latter generally requires a stiff ODE solver that can handle the stiff reaction terms. In our implementation we used the splitting methods described by Toro [8]. A Roe-type solver is used to update the source free Euler equations, and a stiff ODE package, Livermore Solver of Ordinary Differential Equations (LSODE) [15], is used to update the source terms for interior points in the domain. The first update takes the initial data at the current time $t^n$ and solves the source free Euler equations and returns the updated states at $t^{n+1}$. Thus

CYCLE 1: The Hydrodynamic update: Solve

$$\mathbf{U}_t + \mathbf{F}(\mathbf{U})_x = 0 , \tag{39}$$

subject to the initial condition $\mathbf{U}(x, t^n) = \mathbf{U}^n$, and return the solution at $t^{n+1}$ so that $\mathbf{U}^{hydro} \equiv \mathbf{U}(x, t^{n+1})$.

The second source term update uses the first update as the initial conditions at $t^n$, and then solves just the temporal ODES with the source terms, to generated the final update at $t^{n+1}$. Thus

CYCLE 2: Source term update: Solve

$$\frac{d\mathbf{U}}{dt} = \mathbf{S}(\mathbf{U}),$$ (40)

subject to the initial condition $\mathbf{U}(x, t^n) = \mathbf{U}^{hydro}$, and return the solution at $t^{n+1}$, $\mathbf{U}(x, t^{n+1}) = \mathbf{U}^{n+1}$.

The hydrodynamics updates $\mathbf{U}^{hydro}$ obey (39) and their cell state averages $\bar{\mathbf{U}}^n_{i+1/2}$, centered at $i + 1/2$, are advanced in the standard way as

$$\bar{\mathbf{U}}^{n+1}_{i+1/2} = \bar{\mathbf{U}}^n_{i+1/2} - \frac{\Delta t}{\Delta x}[\mathbf{F}_{i+1} - \mathbf{F}_i],$$ (41)

where $\mathbf{F}_{i+1}$ and $\mathbf{F}_i$ are numerical fluxes at the cell boundaries. The numerical flux is computed by using Roe's approximation as follows:

$$\mathbf{F}_{i+1} = \frac{1}{2}(\mathbf{F}(\mathbf{U}_L) + \mathbf{F}(\mathbf{U}_R)) - \frac{1}{2}\sum_i \left|\tilde{\mathbf{\Lambda}}_i\right| \tilde{\boldsymbol{\alpha}}_i \tilde{\boldsymbol{R}}_i.$$ (42)

The vectors $\mathbf{U}_L$ and $\mathbf{U}_R$ in Eq. (42) are the state vectors at cell interface at $i$th grid point and these two vectors were obtained by using WENO scheme, which were first introduced by Harten et al. (see [16]). The details of WENO reconstruction are found in [7,17,18] for example. The other quantities $\tilde{\alpha}_i$, $\tilde{\Lambda}_i$, $\tilde{R}_i$ in Eq. (42) are the vector $\boldsymbol{\alpha}$, matrices functions $\mathbf{\Lambda}$, and $\boldsymbol{R}$ applied at Roe averaged state $\tilde{\mathbf{U}}$. Those computations require the Jacobian of the exact system given by

$$\mathbf{J}(\mathbf{U}) = \frac{\partial \mathbf{F}}{\partial \boldsymbol{U}} = \begin{bmatrix} 0 & 1 & 0 & 0 & 0 \\ c^2 - u^2 - \frac{p_{,e}}{\rho}(H - u^2) - \frac{\lambda_1 p_{,\lambda_1}}{\rho} - \frac{\lambda_2 p_{,\lambda_2}}{\rho} & 2u - \frac{up_{,e}}{\rho} & \frac{p_{,e}}{\rho} & \frac{p_{,\lambda_1}}{\rho} & \frac{p_{,\lambda_2}}{\rho} \\ u\left(c^2 - H - \frac{p_{,e}}{\rho}(H - u^2) - \frac{\lambda_1 p_{,\lambda_1}}{\rho} - \frac{\lambda_2 p_{,\lambda_2}}{\rho}\right) & H - \frac{u^2 p_{,e}}{\rho} & u\left(1 + \frac{p_{,e}}{\rho}\right) & u\frac{p_{,\lambda_2}}{\rho} & u\frac{p_{,\lambda_2}}{\rho} \\ -u\lambda_1 & \lambda_1 & 0 & u & 0 \\ -u\lambda_2 & \lambda_2 & 0 & 0 & u \end{bmatrix},$$ (43)

where

$$H = e + \frac{1}{2}u^2 + \frac{p}{\rho} \quad \text{and} \quad c^2 = p_{,\rho} + \frac{p}{\rho^2}p_{,e},$$ (44)

and the comma notation subscript denotes the partial derivative with respect to thermodynamics argument.

The Jacobian can be diagonalized and has real eigenvalues (the characteristic wave speeds) and real eigenvectors according to

$$\mathbf{J} = \boldsymbol{R}\mathbf{\Lambda}\boldsymbol{R}^{-1},$$ (45)

where $\boldsymbol{R}$ is identified as the matrix composed the right eigenvectors of $\mathbf{J}$ (columns)

$$\boldsymbol{R}(\mathbf{U}) = \begin{bmatrix} 1 & 1 & 1 & 0 & 0 \\ u - c & u & u + c & 0 & 0 \\ H - uc & H - p/\rho - \rho\frac{p_\rho}{p_{,e}} & H + uc & -\frac{p_{,\lambda_1}}{p_{,e}} & -\frac{p_{,\lambda_2}}{p_{,e}} \\ \lambda_1 & \lambda_1 & \lambda_1 & 1 & 0 \\ \lambda_2 & \lambda_2 & \lambda_2 & 0 & 1 \end{bmatrix},$$ (46)

and $\mathbf{\Lambda}$ is the diagonal matrix corresponding to the eigenvectors

$$\Lambda = \text{diag}\left[(u - c), u, (u + c), u, u\right].$$ (47)

The Roe averaged states are defined by

$$\tilde{\mathbf{U}} = [\tilde{\rho}, \tilde{u}, \tilde{e}, \tilde{\lambda}_1, \tilde{\lambda}_2],$$ (48)

where

$$\tilde{\rho} = \sqrt{\rho_R \rho_L},$$ (49)

$$\tilde{u} = \frac{\sqrt{\rho_L}u_L + \sqrt{\rho_R}u_R}{\sqrt{\rho_L} + \sqrt{\rho_R}},$$ (50)

$$\tilde{e} = \frac{\sqrt{\rho_L}e_L + \sqrt{\rho_R}e_R}{\sqrt{\rho_L} + \sqrt{\rho_R}},$$ (51)

$$\tilde{\lambda_1} = \frac{\sqrt{\rho_L}\lambda_{1L} + \sqrt{\rho_R}\lambda_{1R}}{\sqrt{\rho_L} + \sqrt{\rho_R}},$$ (52)

$$\tilde{\lambda_2} = \frac{\sqrt{\rho_L}\lambda_{2L} + \sqrt{\rho_R}\lambda_{2R}}{\sqrt{\rho_L} + \sqrt{\rho_R}}.$$ (53)
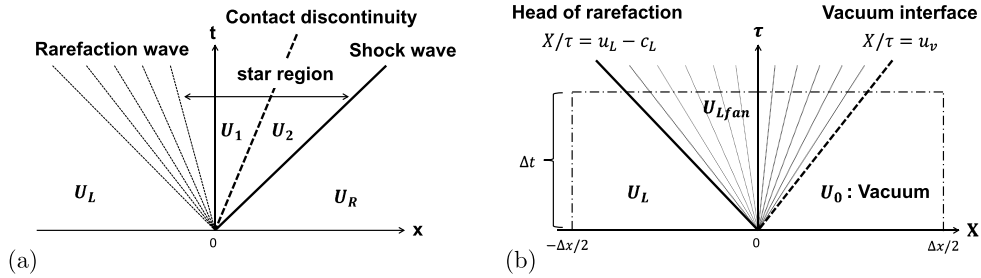
**Fig. 2.** (a) A solution of Vacuum Riemann Problem: This solution is not possible if $\mathbf{U}_R$ is a vacuum state. (b) A possible solution of a Vacuum Riemann Problem.

The enthalpy $H$ in $\mathbf{J}(\mathbf{U})$ is also computed in the same way,

$$\tilde{H} = \frac{\sqrt{\rho_L}\, H_L + \sqrt{\rho_R}\, H_R}{\sqrt{\rho_L} + \sqrt{\rho_R}}. \tag{54}$$

Detailed derivations of Roe average and the pressure derivatives of the averages can be found in Roe [19,20], Glaister [5], Xu [6] and elsewhere.

### 3.2. Vacuum Riemann problem (VRP) and vacuum tracking method for non-ideal EOS

The vacuum Riemann problem (VRP) is by definition a Riemann problem with vacuum initial condition on one side and a constant state at another side of a computational domain. The vacuum is defined such that the mass density in the geometrical domain of the vacuum is zero, i.e. there is an absence of material. Consider the situation with the presence of vacuum in the right state ($x > 0$). In the vacuum region, the conserved variables are zero so that the sound velocity and pressure will also be zero. The VRP for the source free Euler equations can be written as

$$\frac{\partial \mathbf{U}}{\partial t} + \frac{\partial \mathbf{F}(\mathbf{U})}{\partial x} = \mathbf{0}, \tag{55}$$

and the initial condition is

$$\mathbf{U}(x,0) = \begin{cases} (\rho_L, u_L, e_L, \lambda_{L1}, \lambda_{L2}) & \text{for} \quad x < 0, \\ (0, 0, 0, 0, 0) & \text{for} \quad x > 0. \end{cases} \tag{56}$$

The vacuum Riemann problem has a solution structure that is different from a conventional Riemann problem, but it can be obtained as a limit of the conventional Riemann problem [21,8].

We start with a brief description of the vacuum Riemann problem and Munz's tracking method and then extend the algorithm for a general EOS of the form $p = p(v, e, \lambda_1, \lambda_2)$. Fig. 2(a) shows a Riemann problem that consists of constant left state $\mathbf{U}_L$, that is connected to a left-going fan, that terminates on a constant state $\mathbf{U}_1$ that has a particle velocity that defines a contact line in $x, t$ space. The right state $\mathbf{U}_R$ is connected by a right going shock to another constant state $\mathbf{U}_2$ whose pressure and particle velocity (but not necessarily the density) must match across the contact discontinuity to the constant state $\mathbf{U}_1$. Fig. 2(b), shows a left state $\mathbf{U}_L$, that is connected by a single (left-going) rarefaction fan that terminates on the vacuum state denoted, $\mathbf{U}_0$. In what follows, the velocity of the material vacuum interface (MVI) is $u_v$.

Next we recount the argument that the scenario shown in Fig. 2(a), cannot be used as a solution to the VRP (or rather its analysis collapses the configuration to that shown in Fig. 2(b)). Given the configuration shown in Fig. 2(a), the jumps in the state across the right-going shock with speed $S$ (say) must obey the standard Rankine–Hugoniot conditions for fixed composition,

$$\rho_2 u_2 - \rho_0 u_0 = S(\rho_2 - \rho_0), \tag{57}$$

$$\rho_2 u_2^2 + p_2 - (\rho_0 u_0^2 + p_0) = S(\rho_2 u_2 - \rho_0 u_0), \tag{58}$$

$$u_2(\rho_2 E_2 + p_2) - u_0(\rho_0 E_0 + p_0) = S(\rho_2 E_2 - \rho_0 E_0). \tag{59}$$

The state on the left side of the shock as shown is the state $\mathbf{U}_2$. In this case we have $\rho_0 = 0$, and this leads to the conclusion that

$$u_2 = u_0 = S, \quad p_2 = p_0. \tag{60}$$

But if $\mathbf{U}_R$ is the vacuum state $\mathbf{U}_0$, then $p_0 = 0$, hence $p_2 = 0$. The conditions across the contact discontinuity show that $p_1 = 0$. The solution scenario shown in Fig. 2. If the regularity conditions (19) are imposed, then the zero pressure state is a zero density state. Hence both states $\mathbf{U}_1$ and $\mathbf{U}_2$ are vacuum states, now connected to a left-going rarefaction fan. Therefore the solution of VRP with vacuum right state consists of left rarefaction wave and the tail of the rarefaction merges at the vacuum interface as shown in Fig. 2(b).
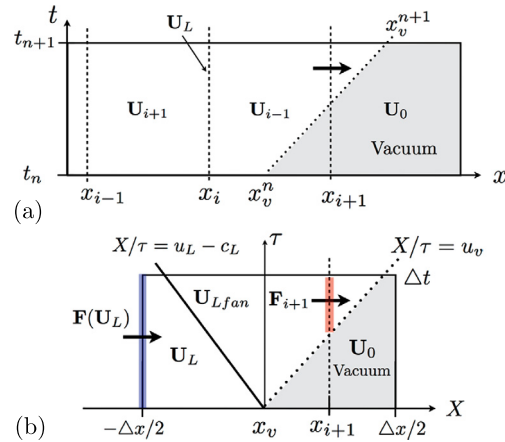
**Fig. 3.** (a) Tracking of vacuum interface boundary in the case that the MVI moves across the cell interface $x_{i+1}$. (b) The case of non-zero flux across the grid interface $x_{i+1}$, denoted by $\mathbf{F}_{i+1}$.

Thus Riemann problem for vacuum right state has the left non-vacuum constant states $\mathbf{U}_L = (\rho_L, u_L, p_L)$ and the right vacuum state

$$\mathbf{U}_0 = (\rho_0, u_0, p_0) \equiv (0, 0, 0), \tag{61}$$

where $u_v$ is the velocity of the material vacuum interface (MVI). One elementary wave (isentropic, rarefaction fan) connects the left non-vacuum and the right vacuum state.

### 3.2.1. Numerical flux approximation

Numerical approximation of gas flow near the gas–vacuum boundary can give rise to severe difficulties in the numerical scheme, associated with zero or near-zero density used in mathematical model of the equation of state. The Munz approximation scheme [1] computes the flux at the gas–vacuum interface and simultaneously tracks the vacuum material interface. The original algorithm was developed for the case of inert, perfect gas. We use the Munz flux approximations and extend the algorithm updates to multi-component reacting flow uses non-ideal EOS forms that are commonly used in explosive modeling. First, we briefly describe the Munz flux formula, for completeness and to clarify the original presentation.

Let $x_v^n$ be the location of the material vacuum interface, with velocity $u_v^n$ at the current time $t = t^n$. The location of the MVI at time $t_{n+1}$ is estimated by the advance

$$x_v^{n+1} = x_v^n + (t_{n+1} - t_n) u_v^n. \tag{62}$$

The numerical flux $\mathbf{F}_{i+1}$ at the $(i+1)$th cell boundary is computed based on the estimated position of the MVI, see Fig. 3(a). If the MVI does not cross the cell interface at $x_{i+1}$ at time $t_{n+1}$, such that $x_v^{n+1} \leq x_{i+1}$, then the interface lies in the vacuum during the time step and the flux $\mathbf{F}_{i+1}$ is zero. If the MVI does cross the cell interface at $x_{i+1}$ at time $t_{n+1}$ (as shown), such that $x_v^{n+1} > x_{i+1}$ then the flux is computed by means of solving a local Vacuum Riemann Problem (VRP) centered at $x = x_v^n$. The initial data for the VRP (for a right going MVI) is

$$\mathbf{U}(x, 0) = \begin{cases} \mathbf{U}_L & \text{for} \quad X < 0 \\ \mathbf{U}_0 & \text{for} \quad X > 0 \end{cases} \tag{63}$$

where $\mathbf{U}_0$ is the vacuum state and $\mathbf{U}_L$ is a non-vacuum left state.

The VRP has the vacuum state on $\mathbf{U}_R = \mathbf{U}_0$ on the right. For the left state $\mathbf{U}_L$, Munz proposed an average that is weighted between the cell-centered states on the left and right of the $x_i$ interface

$$\mathbf{U}_L = \alpha \bar{\mathbf{U}}_{i+1/2}^n + (1 - \alpha) \mathbf{U}_{i-1/2}^n \quad \text{with} \quad \alpha = \frac{x_v^n - x_i}{x_{i+1} - x_i}. \tag{64}$$

The cell between $x_i$ and $x_{i+1}$, has vacuum in the interval $[x_v^n, x_{i+1}]$, with value $\bar{\mathbf{U}}_{i+1/2}^n$ in that region. The average of the non-vacuum state over the entire cell is $\mathbf{U}_{i+1/2}^n$ is defined by $\bar{\mathbf{U}}_{i+1/2}^n(x_v^n - x_i) = \mathbf{U}_{i+1/2}^n(x_{i+1} - x_i)$ such that

$$\mathbf{U}_L = \mathbf{U}_{i+1/2}^n + \frac{x_{i+1} - x_v^n}{x_{i+1} - x_i} \mathbf{U}_{i-1/2}^n \tag{65}$$

is used for the left state.

Munz' approximate solution to this VRP is

$$\mathbf{U}(x, t) = \begin{cases} \mathbf{U}_L & \text{for} \quad X/\tau < u_L - c_L \\ \mathbf{U}_{Lfan} & \text{for} \quad u_L - c_L < X/\tau < u_v \\ \mathbf{U}_0 & \text{for} \quad X/\tau > u_v \end{cases} \tag{66}$$

where all the states are constants. The constant state $\mathbf{U}_{Lfan}$ is obtained by using the integral form of the conservation law, by integrating the conservation law over the region bound by $X = -\Delta x/2$, $X = u_v \tau$ and $\Delta t$. See Fig. 3(b), gives

$$\int_{-\Delta x/2}^{u_v \Delta t} \mathbf{U}(x, \Delta t) dX = \frac{\Delta x}{2} \mathbf{U}_L + \mathbf{F}(\mathbf{U}_L) \Delta t . \tag{67}$$

The state $\mathbf{U}(x, \Delta t)$ has the value $\mathbf{U}_{Lfan}$ for $x \in [(u_L - c_L)\Delta t, u_v \Delta t]$.

The state in that fan region is approximated with an averaged value $\mathbf{U}_{Lfan}$. If one applies the integral conservation law to the region, $x \in [-\Delta x/2, x_{i+1}]$ and $t \in [t_n, t_{n+1}]$ one obtaines

$$\int_{-\Delta x/2}^{(u_L - c_L)\Delta t} \mathbf{U}(x, \Delta t) dX + \int_{(u_L - c_L)\Delta t}^{u_v \Delta t} \mathbf{U}(x, \Delta t) dX = \frac{\Delta x}{2} \mathbf{U}_L + \mathbf{F}(\mathbf{U}_L) \Delta t , \tag{68}$$

or

$$(u_L - c_L)\Delta t \mathbf{U}_L + \frac{\Delta x}{2} \mathbf{U}_L + [u_v - (u_L - c_L)]\Delta t \mathbf{U}_{Lfan} = \frac{\Delta x}{2} \mathbf{U}_L + \mathbf{F}(\mathbf{U}_L) \Delta t , \tag{69}$$

which obtains the formula for $\mathbf{U}_{Lfan}$

$$\mathbf{U}_{Lfan} = \frac{\mathbf{F}(\mathbf{U}_L) - (u_L - c_L)\mathbf{U}_L}{u_v - u_L + c_L} . \tag{70}$$

This approximation is subject to the standard restriction that the waves generating from an interface do not interact within the cell by waves from adjacent cell interfaces, which implies the CFL condition

$$\Delta t \leq \frac{\Delta x/2}{S_{max}} , \tag{71}$$

where $S_{max}$ is the maximum wave velocity, i.e. $\max[|u_L - c_L|, |u_v|]$.

The next step is to use the approximate solution (66), (70) to calculate the flux at $x_{i+1}$, when $x_v^{n+1} > x_{i+1}$, see Fig. 3(a). The left non-vacuum states lie in the interval $[-\Delta x/2, 0]$ and the vacuum takes place in the shifted interval $[0, \Delta x/2]$. Integrating the integral conservation law across the box from $[-\Delta x/2, x_{i+1} - x_v^n]$, and $[0, \Delta t]$, leads to

$$\int_{-\Delta x/2}^{x_{i+1} - x_v^n} \mathbf{U}(x, \Delta t) dX = \frac{\Delta x}{2} \mathbf{U}_L + \mathbf{F}(\mathbf{U}_L^r) \Delta t - \mathbf{F}_{i+1} \Delta t . \tag{72}$$

This can be recast as

$$\int_{-\Delta x/2}^{(u_L^r - c_L^r)\Delta t} \mathbf{U}(x, \Delta t) dX + \int_{(u_L^r - c_L^r)\Delta t}^{x_{i+1} - x_v^n} \mathbf{U}(x, \Delta t) dX = \frac{\Delta x}{2} \mathbf{U}_L^r + \mathbf{F}(\mathbf{U}_L^r) \Delta t - \mathbf{F}_{i+1} \Delta t , \tag{73}$$

and on the timeline $t = t^{n+1}$ we use

$$\mathbf{U}(x, \Delta t) = \begin{cases} \mathbf{U}_L & \text{for} \quad -\Delta x/2 < X < (u_L - c_L)\Delta t \\ \mathbf{U}_{Lfan} & \text{for} \quad (u_L - c_L)\Delta t < X < (x_{i+1} - x_v^n) \end{cases} . \tag{74}$$

From the approximate solution (66), and Eq. (72), we obtain

$$(u_L - c_L)\Delta t \mathbf{U}_L + \frac{\Delta x}{2} \mathbf{U}_L + [x_{i+1} - x_v^n - (u_L - c_L)\Delta t]\mathbf{U}_{Lfan} = \frac{\Delta x}{2} \mathbf{U}_L + \mathbf{F}(\mathbf{U}_L) \Delta t - \mathbf{F}_{i+1} \Delta t . \tag{75}$$

By separate consideration of the cases when the left rarefaction boundary is such that $u_L^r - c_L^r > 0$ or $u_L^r - c_L^r \leq 0$, the flux $\mathbf{F}_{i+1}$ at $x_{i+1}$ computed from (75) is written concisely as

$$\mathbf{F}_{i+1} = \mathbf{F}(\mathbf{U}_L^r) - \frac{1}{\Delta t} \min\left[(u_L^r - c_L^r)\Delta t, x_{i+1} - x_v^n\right] \mathbf{U}_L^r$$
$$- \frac{1}{\Delta t} \max\left[0, x_{i+1} - x_v^n - (u_L^r - c_L^r)\Delta t\right] \mathbf{U}_{Lfan}^r . \tag{76}$$

In summary, the method updates the interface location and determines approximate fan states in the MVI adjacent cell, consistent with the integral conservation law, then updates the flux at the vacuum interface boundary. The tracking method is only activated when the density of left (or right) local Riemann problem has a neighboring vacuum state. If any neighboring state is not a vacuum state, the algorithm computes the flux using the general Riemann solver (in our case the Roe-solver for general equation of state). A simple criterion is required to establish a vacuum (or extremely low pressure state). In our case a density cut off is used, and for the applications discussed in the following section sets the vacuum criteria to $10^{-9}$ g/cm$^3$. When the ideal equation of state is used and no reaction occurs, the velocity $x_v$ of vacuum interface can be computed analytically as shown by Munz. However when non-ideal EOS for reactive flow is used, the computation of vacuum interface is not simple and depends on how the reaction quenches during the isentropic expansion. Furthermore an expression for the pressure in the isentropic fan cannot be obtained in closed form and numerical integration is required. We describe these essential considerations in the next section.

### 3.3. Considerations and the limiting conditions near the vacuum edge for multi-component reacting flow

In previous section, we described the basic tracking algorithm. Here we add the considerations required to employ the algorithm for a multi-component reacting flow with mechanical and thermal mixture EOS form expressed as of the form $p = p(v, e, \lambda_i)$ and $p = p(v, T, \lambda_i)$. Menikoff [22] worked the details for a complete MG EOS, which we choose to model the component EOS forms for the discussion in this section. We assume that

$$e_i(p, v_i) = e_i^s(v_i) + \frac{v_i}{\Gamma_i}(p - p_i^s(v_i)) + e_{0i}, \tag{77}$$

where we assume that $p_i^s(v_i)$ and $e_i^s(v_i)$ are specified reference functions, and in the case when an isentrope is used as a reference curve, $e_i^s$ is such that $\partial e_i^s / \partial v_i = -p_i^s(v_i)$. Both $\Gamma_i$ and $e_{0i}$ are assumed constants. If the specific heat is constant and the reference curve is an isentrope, Menikoff shows that the thermal equation of state is given by

$$p = p_i^s(v_i) + \frac{c_{vi}\Gamma_i}{v_i}\left[ T - T_0 \left(\frac{v_0}{v_i}\right)^{\Gamma_i} \right]. \tag{78}$$

The volume $v_0$ is a reference volume. One can also work out the form for the component entropies, to obtain

$$s_i(p, v_i) = s_{0i} + c_{vi} \ln \left[ 1 + \frac{v_0}{\Gamma_i c_{vi} T_0}[p - p_i^s(v_i)] \left(\frac{v_i}{v_0}\right)^{1+\Gamma_i} \right]. \tag{79}$$

The mixture energy and volume and entropy are given by

$$e = \sum_i e_i \lambda_i, \quad v = \sum_i v_i \lambda_i \quad \text{and} \quad s = \sum_i s_i \lambda_i. \tag{80}$$

In the region near the vacuum edge the flow is highly rarefied, and nearly collisionless so it is reasonable to assume that the reaction rates are zero (as is the basic premise of the TOFMS experiments), and hence isentropic. The task of working out the structure of the flow in the fan is the task of finding the isentrope in the vacuum fan solution. We briefly discuss the nature of that calculation using these non-ideal EOS forms, without further assumption, except that of isentropic expansion.

The analysis of the left rarefaction fan at the right edge of the domain then requires an expression for the $p, v$ isentropes for the mixture. In turn this requires finding expressions (or numerically calculating) the values for the partial volumes $v_i(p, v)$ of components in the mixture. The mixture entropy is then given by

$$s = \sum_i s(v_i(p, v), p)\lambda_i \tag{81}$$

and is found as a function of $p, v$ and $\lambda_i$, in general. The determination of $v_i(p, v)$ depends on the forms of the mixture closure. If the mixture closure uses the PT-EQB, an iterative numerical solution is required even for a simplified version of the MG form. But that can always be done in principle, as the formulation is complete. The sound speed squared on the isentrope is given by $c^2 = \partial p / \partial \rho|_s$, and can be calculated

$$c^2 = v^2 \left( p + \frac{\partial e}{\partial v}\Big|_{p,\lambda_i} \right) \Big/ \frac{\partial e}{\partial p}\Big|_{v,\lambda_i} \tag{82}$$

to obtain $c^2(p, v, \lambda_i)$. The constant entropy in the left state $s_L$ (say) can be used in (81) to generate the $p, v$ isentrope that applies in the rarefaction of the form $s_L = s(p, v, \lambda_i)$. In turn this can be used to construct the solution and compute the MVI velocity.

An equivalent and computationally simple procedure is available by a directly integrating states through the fan as follows. From the consideration of the Generalized Riemann Invariants for the system (46) for the rarefaction wave $\mu_1 = u - c$ we have

$$d\rho = \frac{d(\rho u)}{u - c} = \frac{d(\rho e)}{H - uc}.$$  (83)

The first equality in Eq. (83) gives a formula for the MVI velocity, $u_v$ where $\rho_R = 0$ and $u_R = u_v$ as shown in Fig. 2(b).

$$u_v = u_L + \int_0^{\rho_L} \frac{c}{\rho} d\rho.$$  (84)

The second equality from Eq. (83), obtains the isentropic change of the internal energy in the isentropic expansion and is written as

$$de = \frac{p}{\rho^2} d\rho.$$  (85)

This equation can be used to derive a differential equation for $p(\rho, \lambda_i)$. As an example, consider the equation of state defined by using the JWL EOS forms for two components as defined by Eq. (29). Using the form (34) the energy can be written as

$$e(p, v, \lambda) = A + G p$$  (86)

where

$$A(v_R, v_p, \lambda) = (1 - \lambda) \left( e_R^s(v_R) - \frac{v_R}{w_R} p_R^s(v_R) \right) + \lambda \left( e_P^s(v_P) - \frac{v_P}{w_P} p_P^s(v_P) \right),$$  (87)

and

$$G(v_R, v_p, \lambda) = \lambda \frac{v_P}{\omega_P} + (1 - \lambda) \frac{v_R}{\omega_R}.$$  (88)

The closure condition is used to determine the component specific volumes $v_P$ and $v_R$. The PT-EQB condition for the thermal EOS form is

$$T \equiv T_R(v_R, p) = T_P(v_P, p),$$  (89)

where $T_R$ and $T_P$ are obtained from the thermal EOS for the components. With $\Phi = v_P/v_R$, and Eq. (30) leads to

$$v_R = \frac{v}{1 - \lambda + \lambda \Phi}, \quad v_P = \frac{v \Phi}{1 - \lambda + \lambda \Phi}$$  (90)

Eq. (89) determines a value of $\Phi(p, v)$ for fixed $\lambda$. Given a value $\lambda$, the functions $A$ and $G$ are functions of $v$ and $p$. Then if we substitute Eq. (86) in (85) one obtains a differential equation for the pressure as a function of density for fixed composition, that holds in the rarefaction wave

$$\frac{dp}{d\rho} = \frac{1}{G + \frac{\partial A}{\partial p} + p \frac{\partial G}{\partial p}} \left[ \left\{ \frac{1}{\rho^2} - \left( \frac{\partial G}{\partial \rho} \right) \right\} p - \frac{\partial A}{\partial \rho} \right], \quad \text{subject to} \quad p(\rho_L) = p_L.$$  (91)

Note that the $c^2 = dp/d\rho$ on the isentrope. The interface velocity is then computed from (84) as

$$u_I = u_L + \int_0^{\rho_L} \frac{1}{\rho} \sqrt{\frac{1}{G + \frac{\partial A}{\partial p} + p \frac{\partial G}{\partial p}} \left[ \left\{ \frac{1}{\rho^2} - \left( \frac{\partial G}{\partial \rho} \right) \right\} p - \frac{\partial A}{\partial \rho} \right]} d\rho.$$  (92)

The pressure $p$ in the integrand of Eq. (92) is the solution of the ODE (91).

Generally the ODE for $p$ and the integral for $u_v$ must be computed numerically. However if the simpler P-EQB closure is used to compute the component volumes as in Stewart et al. in [23], then $\Phi$ does not depend on pressure and the ODE (91) simplifies to

$$\frac{dp}{d\rho} = \frac{1}{G} \left[ \left\{ \frac{1}{\rho^2} - \left( \frac{dG}{d\rho} \right) \right\} p - \frac{dA}{d\rho} \right], \quad \text{subject to} \quad p(\rho_L) = p_L,$$  (93)

and can be integrated analytically to obtain the solution for $p$

$$p(\rho) = p_1 \left( \frac{\rho}{\rho_1} \right)^{\Gamma + 1} + \Gamma \rho^{\Gamma + 1} \left( A(\rho_1) \rho_1^{-\Gamma} - A(\rho) \rho^{-\Gamma} + \Gamma \int_\rho^{\rho_1} A \rho^{-\Gamma - 1} d\rho \right),$$  (94)

where

$$\Gamma = (1 - \lambda + \lambda \Phi) / \left( \frac{\lambda}{\omega_p} + \frac{(1 - \lambda) \Phi}{\omega_R} \right),$$  (95)

so that $G = \frac{v}{\Gamma}$.

At the limit of zero density, one must check the Liu–Smoller conditions (19) to make sure that the pressure and sound speed vanish as the density vanishes. The solution satisfies the end condition $p(0) = 0$. The derivative is given by

$$\frac{dp}{d\rho} = (\Gamma + 1)\left(\frac{p_L}{\rho_L^{\Gamma+1}} + \Gamma\frac{A(\rho_L)}{\rho_L^{\Gamma}} + \Gamma^2\int_{\rho}^{\rho_L}\frac{A}{\rho^{\Gamma+1}}d\rho\right)\rho^{\Gamma} - \Gamma\rho\frac{dA}{d\rho} - \Gamma(\Gamma+1)A(\rho),$$ (96)

and the solution satisfies the Liu–Smoller conditions (19) if $A = o(\rho^{\Gamma+1})$ and $A' = o(\rho^{\Gamma+1})$ as $\rho \to 0$.

Physical consideration of the near collision limit of a vacuum would admit the reasonable approximation that each EOS for each gaseous component of the mixture limits to an ideal gas form. For each component in the limit of infinite volume, or zero density we would require that

$$e_i^s(v_i) \to 0, \quad p_i^s(v_i) \sim \frac{c_{vi}\Gamma_i}{v_i}\left[T_0\left(\frac{v_0}{v_i}\right)^{\Gamma_i}\right] \to 0 \quad \text{as} \quad \rho_i = 1/v_i \to 0,$$ (97)

so that in the limit of low densities the ideal EOS forms apply

$$e_i(p, v_i) \sim \frac{pv_i}{(\gamma_i - 1)} + e_{0i}, \quad \text{and} \quad p \sim \frac{R_i T}{v_i},$$ (98)

where $c_{vi}\Gamma_i \to R_i$ (the ideal gas constant weighted by the molecular weight of the component) and $\Gamma_i \to \gamma_i - 1$. One can view these additional requirements as a modeling statement that reflects the correct physics or simply a physically-based regularization for the model that is used only near the MVI. In either case the additional requirement that each gaseous component EOS form limits to ideal EOS form when PT-EQB is used as the mixture closure model, will guarantee that the Liu–Smoller conditions are met which we show next.

For the conditions near the MVI, the state will be such that the EOS forms of the components of the mixture limit to the ideal EOS forms. For fixed pressure and temperature, we can take the expression for the partial volumes and sum them over the components to obtain

$$v = \sum_i v_i\lambda_i = \left(\sum_i R_i\lambda_i\right)\frac{T}{p} = \frac{RT}{p}$$ (99)

where $R = \sum_i R_i\lambda_i$ is the mass weight ideal gas constant. Then specific energy of the multi-component mixture limits to

$$e \sim \frac{pv}{\gamma - 1} + \sum_i e_{i0}\lambda_i, \quad \text{with} \quad \frac{1}{\gamma - 1} \equiv \left(\sum_i \frac{\lambda_i}{(\gamma_i - 1)}\frac{R_i}{R}\right)$$ (100)

and where we have used $T \sim pv/R$ and identified, and $\gamma$ is a function of the composition. Then the standard formula for sound speed squared

$$c^2 = \gamma pv$$ (101)

and the isentrope in the fan expansion is given by

$$\frac{p}{\rho^{\gamma}} = \kappa,$$ (102)

where the constant $\kappa$ is also a function of the frozen composition, which determines $\gamma$. If these limiting forms for the EOS are used then the Liu–Smoller conditions are satisfied since $p/\rho^{\gamma} = \kappa = p_L/(\rho_L^{\gamma}) > 0$ and $c^2 = \gamma p/\rho$ implies $c = \sqrt{\gamma\kappa}\,\rho^{(\gamma-1)/2}$ with the properties that

$$c(\rho) > 0 \quad \text{for} \quad \rho > 0 \quad \text{and} \quad c(0) = 0,$$ (103)

and

$$\int_0^{\rho_L}\frac{c}{\rho}d\rho = \frac{2\sqrt{\gamma\kappa}}{\gamma - 1}\rho_L^{(\gamma-1)/2} \quad \text{bounded}.$$ (104)

It is important to compute the integral (92) carefully, since there is often an abrupt change in the states through the rarefaction, especially when a shock wave first hits the MVI. To avoid singularity occurring from lower limit of the integrand in (92), we always split the integration into two pieces as shown in Fig. 4. We define a cut-off density $\epsilon$ that is small enough to ensure that the ideal gas limiting form is a good physical approximation to the flow, and write the integral

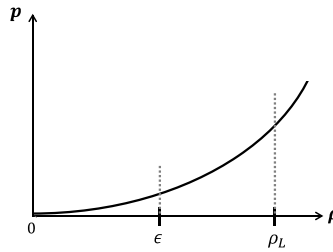$$\int_0^{\rho_L}\frac{c}{\rho}d\rho = \int_0^{\epsilon}\frac{c}{\rho}d\rho + \int_{\epsilon}^{\rho_L}\frac{c}{\rho}d\rho.$$ (105)

**Fig. 4.** Two ranges of integration of Eq. (105).

For a given specified value of $\epsilon$, with $0 < \epsilon << 1$, the first term of (105) is evaluated with Eq. (104)

$$\int_0^{\epsilon} \frac{c}{\rho} d\rho = \frac{2\sqrt{\gamma \kappa}}{\gamma - 1} \rho_L^{(\gamma-1)/2},$$

(106)

and the second integral is computed numerically using the Romberg's method [24].

As an example, the JWL EOS forms are MG forms that are commonly used to model explosives and they have the property that they limit to ideal EOS forms as the component densities vanish. A JWL EOS for a component takes the form

$$p_i^s = A_i e^{-R_{1i}(v_i/v_0)} + B_i e^{-R_{2i}(v_i/v_0)} + \frac{R_i T_0}{v_0} \left( \frac{v_0}{v_i} \right)^{\gamma_i},$$

$$e_i^s = \frac{A_i}{R_{1i}} e^{-R_{1i}(v_i/v_0)} + \frac{B_i}{R_{2i}} e^{-R_{2i}(v_i/v_0)} + \frac{R_i T_0}{(\gamma_i - 1)} \left( \frac{v_0}{v_i} \right)^{(\gamma_i-1)}$$

(107)

and as $\rho_i = 1/v_i \to 0$, it follows that (97) holds. Thus the JWL EOS behaves like the ideal gas near vacuum region or density is very small, which is a feature built into the JWL EOS calibration.

If the non-ideal EOS forms for the components do limit to the ideal EOS forms in the limit of vanishingly small density, then the classic fan analysis will hold at the extreme edge of the fan. Even then we make the observation that the computed MVI velocity can be very sensitive to the limiting values of the flow near the fan when the reaction ceases, since the composition of the frozen/quenched products determines the mass fraction weighted value of $\gamma$ of the mixture.

Close to the MVI assume that the expansion to vacuum occurs by a left-going isentropic fan seeded by a constant left state that lies in a region a nonzero density, but where the ideal EOS forms are applicable. This would be a point close to the MVI edge, but to the left of it (say). Then the particle velocity and speed relation hold between the defined left state and any state to the right toward the MVI, i.e.

$$u + \frac{2c}{\gamma - 1} = u_L + \frac{2c_L}{\gamma - 1}.$$

(108)

Eq. (108) can be used to illustrate why the tracking of vacuum interface numerically can be very difficult if done without knowledge of the analytical character of the fan solution.

Since the fan boundary at the MVI is characteristic, then $u_v = X/\tau$, and this is consistent with setting $u = u_v$ and $\rho = c = 0$ at the vacuum interface. Then (108) becomes

$$u_v = X/\tau = u_L + \frac{2c_L}{(\gamma - 1)}.$$

(109)

Eq. (109) could be used to compute $u_v$ near the interface, but since the Liu–Smoller requirement insists that in a (computationally) small neighbor of the interface $c_L \to 0$, under resolution, then this relation is simply the identity $u_v = X/\tau = u_L$.

But now consider Eq. (108) in the same small neighborhood, and consider another neighboring state to the right of the same left state in the left fan. We identify this state with a vacuum cut-off density $d$ (say) to designate being close enough to the MVI. Replace $u_v = X/\tau$, as before, but estimate the sound speed which is a function of $\rho$ at the vacuum cut off as

$$c(d) = c_L \left( \frac{d}{\rho_L} \right)^{(\gamma-1)/2}$$

(110)

in which case (108) becomes

$$u_v = u_L + \frac{2c_L}{\gamma - 1} - \frac{2c_L}{\gamma - 1} \left( \frac{d}{\rho_L} \right)^{(\gamma-1)/2}.$$

(111)

There are clearly many ways to go wrong if the local approximations near the vacuum interface are not accurate, inconsistent with the Liu–Smoller conditions or inconsistent with the fan structure. The greatest sensitivity in the formulas are
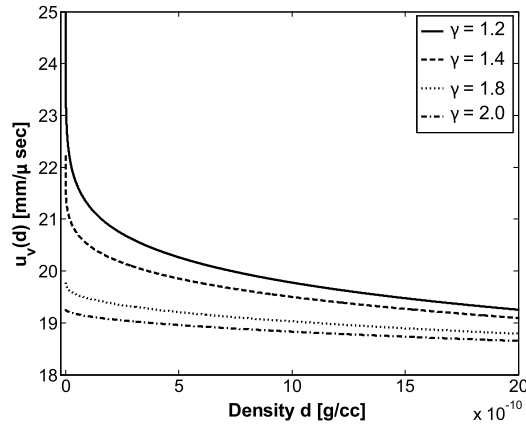
**Fig. 5.** The plot of interface velocity function $u_v(d)$ shown in Eq. (111) with $\rho_L = 3.0e-8$ [g/cm$^3$], $p_L = 3.6e-8$ [GPa], $u_L = 16.5$ [mm/μs].

illustrated by the dependence on the local value of $\gamma$. As $\gamma \rightarrow 1$ the interface velocity function (111) becomes singular, and thus is very sensitive to $\gamma$. Fig. 5 shows the plot of velocity $u_v(d)$ of Eq. (111) as a function of density $d$ for different values of $\gamma$; i.e. $\gamma = 1.2, 1.4, 1.8$, and 2.0. The left state variable $\rho_L$, $p_L$ and $u_L$ shown in Eq. (111) was set to actual computational values at time $t = 1.5$ μs used in the PETN problem in Section 4.2. As shown in the figure, the interface velocity increases rapidly and the slope of $u_v(d)$ becomes very large as $\gamma$ decreases toward one. Also it is clear from the dependence of $\rho_L$ in the denominator of Eq. (111) that if the monotonically decreasing ratio of $(d/\rho_L)$ is not maintained correctly in the approximation scheme, even for fixed $c_L$ that the prediction of the interface velocity can be made highly inaccurate. Since $\gamma$ is a function of the mass fraction as seen in Eq. (100), it is dependent on the composition of the products near the vacuum edge. Thus the details of the kinetic rate law and how the reactions quench, does matter in the calculation of the MVI velocity $u_v$.

The conclusions from the simple considerations above are independent of the grid resolution. The vacuum tracking algorithm uses the fan solution that maintains the correct limiting forms, derived from the EOS forms of the underlying model as the vacuum state is approached. The requirement that the EOS forms limit to the ideal EOS forms and that the reaction stops, is easy to implement and is physically consistent. The JWL EOS form is an example of a non-ideal form that has the correct properties and the Liu–Smoller condition are automatically satisfied. Any vacuum tracking scheme that would work similarly, must employ consideration of the EOS forms used for the mixture in the vicinity of the vacuum, otherwise large and likely catastrophic inaccuracies will occur that will destroy any simulation that has a vacuum or extremely low pressure regions. In the next section, we demonstrate application of the algorithms with examples that explicitly uses ideal and nonideal EOS forms for the mixture of reactants and their products.

## 4. Examples and applications

In this section, we demonstrate the applicability of our algorithm through two representative numerical simulations. The first example uses the ideal equation of state. The second example is representative of the TOFMS experiments which uses the non-ideal JWL EOS forms for reactants and products.

### 4.1. Example 1: An explosive modeled by the ideal gas EOS form whose products expand into a vacuum

In many theoretical studies of high explosives (that are condensed solids at their initial state), the flows are modeled with the ideal EOS forms for a mixture of reactants and products. The reader is referred to Fickett and Davis [12]. We used values listed in their text for this example [12, Chapter 2, C2, p. 46]. The EOS is given by

$$e(p, v, \lambda) = \frac{pv}{\gamma - 1} - Q\lambda. \tag{112}$$

The density in the unreacted explosive is assumed to be $\rho_0 = 1.6$ g/cm$^3$. For the choices $\gamma = 3.0$, and $Q = 4.5156$ MJ/kg, the Chapman–Jouguet (CJ) detonation velocity and pressure are $D_{CJ} = 8.5$ mm/μs and $p_{CJ} = 28.9$ GPa, respectively.

The computational domain is taken to be 50 mm long. The boundary at $x = 0$ is an outflow boundary that enforces zero gradients. The material in the region $0 \le x < 20$ mm is assumed to be a uniform, completely reacted, CJ detonation state with the state vector as $\mathbf{U}_{CJ} = (\rho, u, p, \lambda) = (\rho_{CJ}, u_{CJ}, p_{CJ}, 1)$. In the strong shock approximation, the CJ states are $\rho_{CJ} = (\gamma + 1)/\gamma)\rho_0$, $u_C = D_{CJ}/(\gamma + 1)$, and $p_{CJ} = \rho_0 D_{CJ}^2/(\gamma + 1)$. The material between $20 \le x < 30$ mm is assumed to be at a uniform, completely unreacted, motionless state at an initial density $\rho_0$, but at zero pressure with $\mathbf{U}_{HE} = (\rho, u, p, \lambda) = (\rho_0, 0, 0, 0)$. The region to the right of $x = 30$ mm is assumed to be the vacuum state $\mathbf{U}_0 = (0, 0, 0, 0)$. Thus the initial values are given by

**Table 1**
Initial conditions for the simulation in Example 1.

| State | Reacted CJ state | Unreacted CJ state | Vacuum state |
|---|---|---|---|
| **U** | $0 < x < 20$ | $20 < x < 30$ | $20 < x < 30$ |
| $\rho$ | 2.133 g/cm$^3$ | 1.6 g/cm$^3$ | 0 |
| u | 2.125 mm/$\mu$s | 0 | 0 |
| p | 28.9 GPa | 0 | 0 |

$$\mathbf{U}(x) = \begin{cases} \mathbf{U}_{CJ} \text{ (reacted CJ)} & \text{if } x < 20 \\ \mathbf{U}_{HE} \text{ (unreacted HE)} & \text{if } 20 \leq x < 30 \\ \mathbf{U}_0 \text{ (vacuum)} & x > 30 \end{cases} \tag{113}$$

and listed in Table 1. The reaction rate in the explosive is taken as

$$\dot{\lambda} = (5.0)(1-\lambda)^{0.5}\left(\frac{p}{p_{CJ}}\right)^3 \ \mu s^{-1}, \tag{114}$$

The initial high pressure, density, particle velocity state, $\mathbf{U}_{CJ}$ introduces a shock into the unreacted HE at the $x = 20$ mm interface and initiates a detonation wave, that builds up and runs in the unreacted HE towards the vacuum interface initially at $x = 30$ mm. Since the pressure in the unreacted HE is zero, there is no initial expansion into the vacuum, so the MVI at $x = 30$ mm is motionless until the detonation shock hits the interface and the detonation products start to vent into the vacuum region. The initiated detonation becomes nearly steady, with a von Neumann spike shock pressure of about 55 GPa pressure at approximately $t = 1.3$ μs. At that time it encounters the previously static vacuum interface. After the detonation shock and the following flow in the detonation reaction zone hits the vacuum interface at $x = 30$ mm, the detonation shock disappears and a rarefaction wave is sent backwards to the left into the gas flow. Since reaction rate in the explosive is a function of the pressure, the reaction rate in the fan region drops as the pressure drops. Figs. 6 and 7 show the state variables at different times and show the formation of a detonation, followed by the expansion of products as they vent into the vacuum region. The simulation uses 5000 grid points for the entire domain, and exhibits cleanly defined, well-resolved features and a sharply defined MVI motion.

### 4.2. Example 2: detonation of pentaerythritol tetranitrate (PETN) whose products vent to vacuum

Next we describe a simulation of the expansion of PETN products into a vacuum, that represents a facsimile of TOFMS experiments. The JWL EOS parameters for reactants and products are chosen to match experimental data obtained from macroscopic detonation experiments on PETN [26]. These experiments include those that determine: a) the unreacted shock Hugoniot or $U_p$–$U_s$ relation, b) the overdriven detonation shock Hugoniot for the products, and c) the products expansion experiments that determine constants for the products JWL EOS [27,25,28,26]. The reaction rate parameters are determined from shock initiation experiments that determine the distance and time to detonation as a function of the shock input pressure into the sample. The reader can find details on how the equation of state and rate law parameters are fit to explosives in recent review papers [29,30].

We use model parameters reported by Tarver et al. in [26]. The calibrated parameters of the JWL EOS forms for the reactant and product are given in Table 2. The reference density is given by $\rho_0 = 1.778$ g/cm$^3$. The JWL product equation of state parameters determines the CJ states which are found to be

$$D_{CJ} = 8.23 \text{ mm}/\mu s, \ v_{CJ} = 0.42 \text{ [cm}^3/\text{g]}, \ p_{CJ} = 31.5 \text{ GPa} \tag{115}$$

The distance to detonation for full density PETN is reported as

$$\log_{10} p = a - b \log_{10} x^* \tag{116}$$

where $p$ [GPa] is the shock input pressure and $x^*$ [mm] is observed distance to detonation from the explosive edge, and parameters $a = 1.1767$ [GPa], $b = 0.2432$. We used a simple, pressure dependent reaction rate model with rate parameters chosen so that our PETN model reproduces the reported the run to detonation data, (116). The rate is given by

$$\frac{d\lambda}{dt} = 80 \, (1-\lambda)^{0.5}\left(\frac{p}{p_{CJ}}\right)^5 \ \mu s^{-1}. \tag{117}$$

Fig. 1 shows a schematic of the setup for a simulation of motionless PETN that has vacuum on the right side, and is struck by a impact piston on the right side. Initial states $(p, \rho, \lambda)$ at initial time $t = 0$ are divided into three regions and are shown in Table 3. Through impact on the left side, a shock is introduced into the unreacted material. If the shock is strong enough and the sample is thick enough, then a steady state detonation forms in the PETN sample in the region $x_I < x < x_v$ before the detonation shock strikes the vacuum interface, after which the venting at the interface occurs. In PETN, the steady CJ detonation structure has a reaction complements of approximately 99% in 0.02 mm, and the final 1% of the energy that relaxes to the CJ state, is released in a reaction zone tail that is approximately 0.2 mm. Therefore the
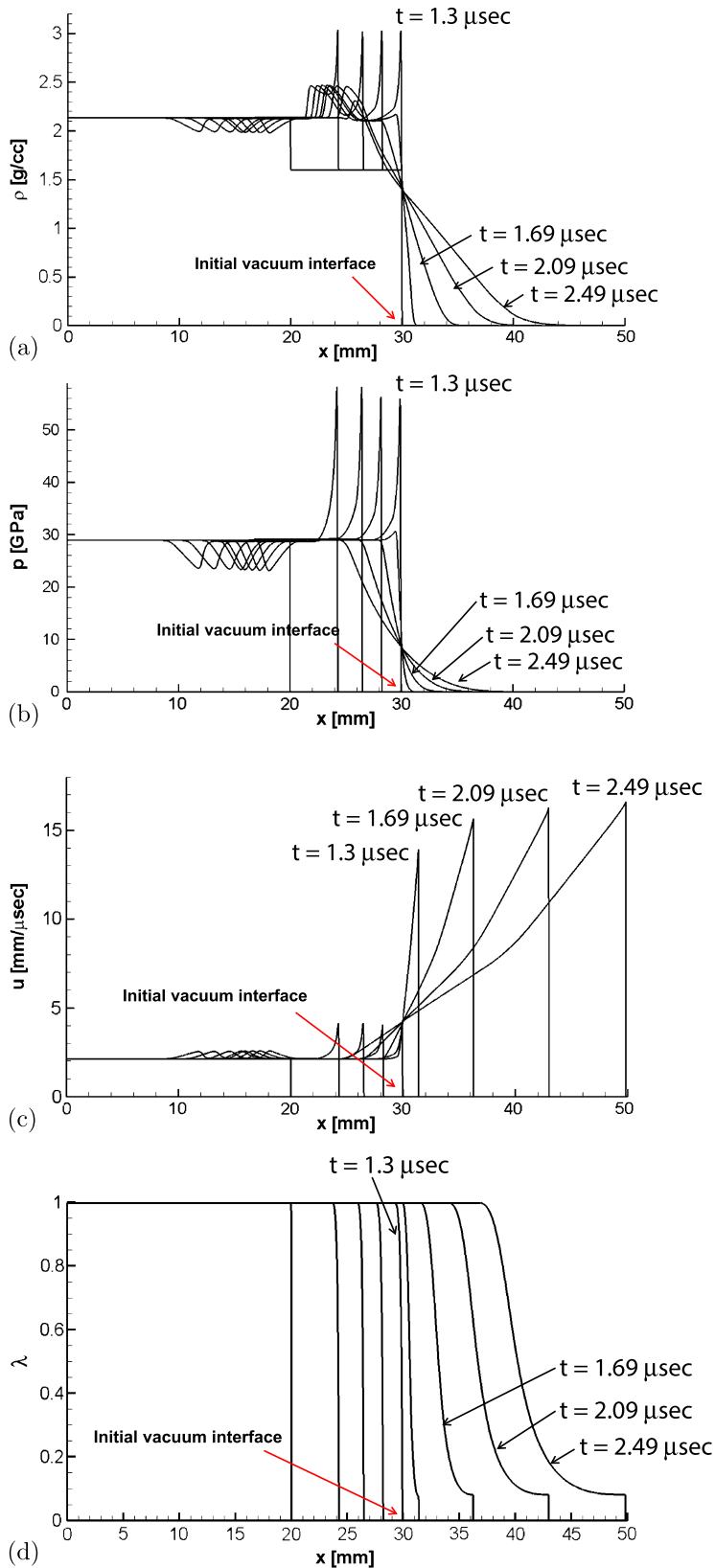
**Fig. 6.** Sequence showing the detonation hitting the MVI and the expansion of products into the vacuum region: (a) density, (b) pressure, (c) velocity, (d) reaction progress.
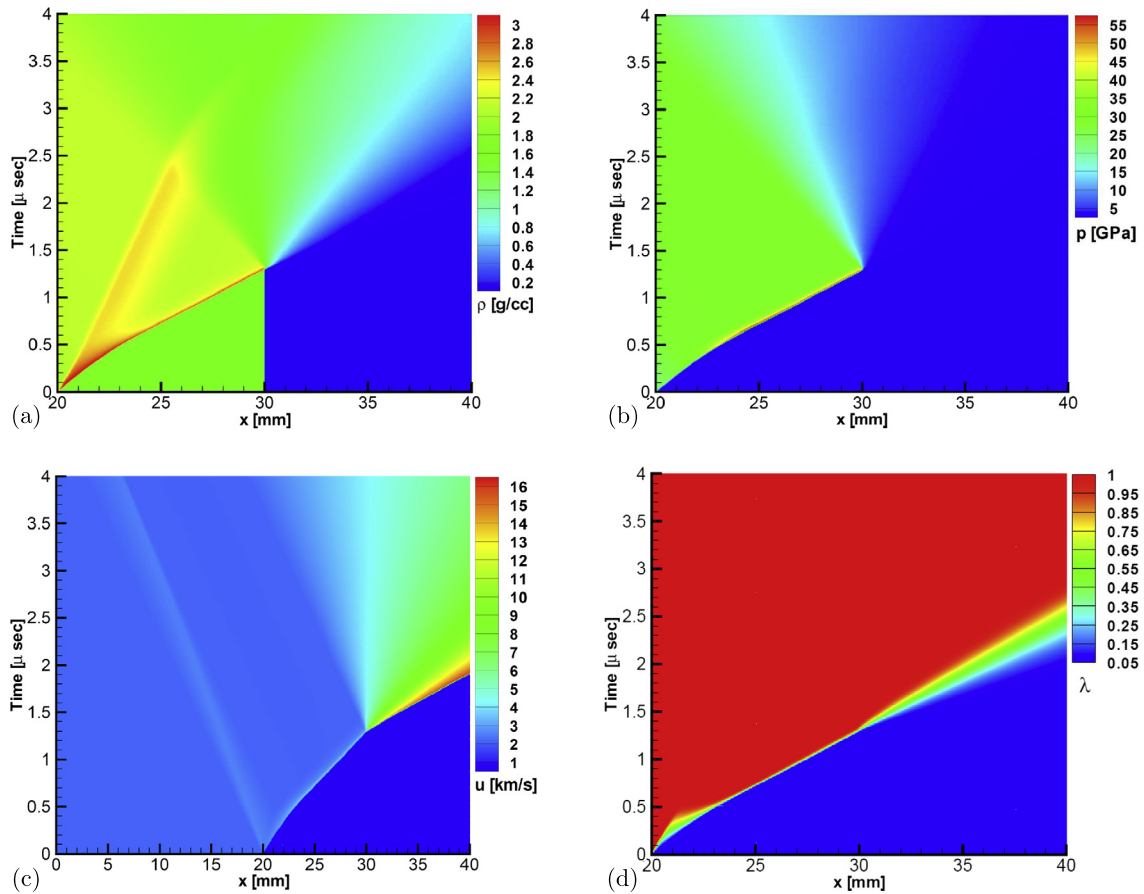
**Fig. 7.** Space time contour plots that show the same sequence as Fig. 6 showing the detonation hitting the MVI and the expansion of products into the vacuum region: (a) density, (b) pressure, (c) velocity, (d) reaction progress field in space and time domain.

**Table 2**
The calibrated parameters of JWL EOS of PETN.

| | $A_i$ [GPa] | $B_i$ [GPa] | $C_i$ | $w_i$ | $R1_i$ | $R2_i$ | $e_{0i}$ [KJ/g] |
|---|---|---|---|---|---|---|---|
| Product JWL ($i = R$) | 1032.158 | 90.57 | 0.0 | 0.57 | 6 | 2.6 | 6.074 |
| Reactant JWL ($i = P$) | 1280.0 | −27.058 | 0.0 | 0.6 | 6 | 2 | 0.0 |

**Table 3**
Initial data for impact simulation Example 2.

| Material | $p$ [GPa] | $\rho$ [g/cm$^3$] | $u$ [mm/μs] | Range |
|---|---|---|---|---|
| Piston | 0.0 | 2.14 | $u_{in}$ | $x \leq x_I$ |
| PETN | 0.0 | 1.778 | 0.0 | $x_I \leq x \leq x_v$ |
| Vacuum | 0 | 0 | 0.0 | $x > x_v$ |

computation requires high resolution, and the spatial grid size must be no more than one micrometer with approximately 20 points in the rapidly changing detonation shock structure. Note that a multi-material solver, described in [31], was used to properly model the flyer impact (of a different material, specifically a plastic KEL-F) and transmission of the impact shock into the PETN sample. But the interior algorithms and the algorithms near the MVI are identical to what is discussed in this paper.

Experimental detection of product species flying through vacuum depends on many factors, that include the thickness of sample and how the sample is shock initiated. A premise of the experiment is that a steady detonation is established by the time the detonation shock hits the vacuum interface and the reactants are quenched by the subsequent rarefaction. When the PETN sample is initiated with an input shock strength of 5 GPa in pressure, matched to the experimental pop-plot shows a steady state detonation is established in about 0.16 μs at around 0.5 mm away from the edge of the sample. In this
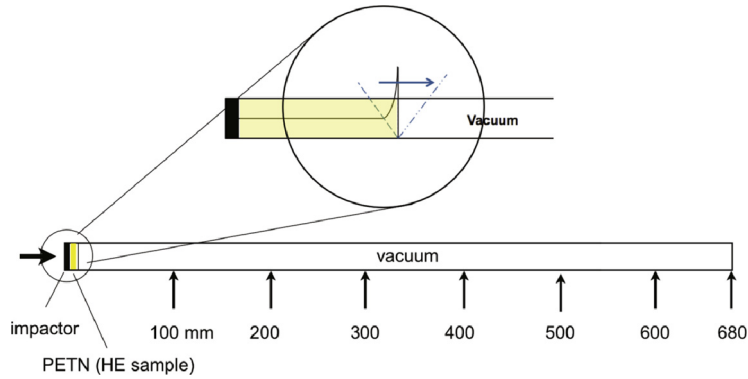
**Fig. 8.** The location of impactor, PETN sample, vacuum and seven probe locations of measurement for simulation in Example 2.

scenario, any sample thicker than 0.5 mm is sufficiently thick to observe steady state detonation. Once the steady state detonation on PETN hits the vacuum interface and the vented products expand at a very high speed, faster than 16 mm/μs.

Next we discuss a set of cases in which the thickness of the sample, i.e. $x_v - x_I$ and the impactor velocity $u_{impactor}$ (i.e. related to the input shock pressure) are varied. In each case the density $\rho$, pressure $p$ and reaction progress $\lambda$ are sampled at a designated point far away from the original vacuum interface locations and the time histories are recorded, similar to what would be recorded at a sampling probe at a fixed point in space in the TOFMS experiment. The three different cases are

- Case I:   $x_v - x_I = 3.0$ mm,   $u_{impactor} = 2.963$ mm/μs
- Case II:   $x_v - x_I = 1.0$ mm,   $u_{impactor} = 2.963$ mm/μs
- Case III:   $x_v - x_I = 3.0$ mm,   $u_{impactor} = 2.563$ mm/μs

Fig. 8 shows the locations of the impactor, PETN (HE sample) and vacuum and probe locations where measurements are recorded. The probe locations are set to $x = 100, 200, 300, 400, 500, 600$ [mm] and $x = 680$ [mm] measured from the initial vacuum interface.

Figs. 9 and 10 plot the state variables in the region $0 < x < 10$ mm. They show the formation of a detonation, followed by the initial expansion of products as they start to vent into the vacuum interface. Fig. 9 shows the solution profiles of the state variables for Case I at the indicated times from $t = 0$ to $t = 0.69$ μs. The solution profiles at $t = 0.39$ μs corresponds to a nominally steady CJ detonation wave that is established in the PETN sample, just prior to the detonation shock hitting the vacuum interface $x_v$ that is initially located at 4 mm. Once the detonation shock wave hits the vacuum interface, the products expand into the vacuum via the action of a rarefaction wave. Fig. 10 shows the corresponding contours of the state variables plotted in the $x$–$t$ (space and time) for Case I. Figs. 9(d) and 10(d), clearly show the region of interest for the experimental study where quenching of the reaction occurs and that would be the region where reactions of the intermediate species would likely cease, since the pressure in the rarefaction fan region drops rapidly.

Next we discuss the observations in the full length of the vacuum region $x \le 680$ mm. After the sample is detonated, the products expand toward the vacuum and spread evenly in the entire vacuum region of the experiment. Fig. 11(a) shows the density profiles in vacuum expanding process from times $t = 5$ μs to $t = 270$ μs for Case I. The density was monitored at various locations. Fig. 11(b) shows the monitored density at the end of the vacuum region at $x = 680$ mm for Cases I, II and III. The density and time of arrival of the density is different for all three cases, and is affected by different sample thicknesses and impact velocities associated with each case. Fig. 12 shows the pressure and particle velocity plotted in the $x$–$t$ (space, time) plane for the entire vacuum regions, for Case I. The velocity of vacuum interface can be estimated to be about 19 mm/μs.

For all three cases at each probe location, we recorded the time of arrival (TOA) that corresponds to a time when specified density value was first sensed. The densities ranged from a low monitoring value of $10^{-8}$ g/cm$^3$, to a maximum of $10^{-3}$ g/cm$^3$. The probes first senses the low values and later sense the higher values and the results for all three cases are shown in Fig. 13. Case II has a smaller explosive sample thickness than Case I, but is subjected to the same impact velocity. In Case II, the detonation wave is not a steady state, CJ detonation when it hits the initial vacuum interface. Fig. 11(b) shows that a smaller peak density is attained and that TOA at the monitoring locations has larger values. Thus the recorded velocity of a constant density front, measured by sampling the products expansion in the vacuum region is slower for Case II than for Case I. Case III has the same sample thickness of the PETN sample as Case I, but the sample is subject to a lower impact velocity. In Case III, the sample is thick enough so that a steady state CJ occurs, and the peak pressure and density observed at the probes is quite similar to Case I, but very slight shift of TOA of fixed density value at the probes is observed.

These results can be summarized by computing the phase velocity of a constant density front as the products encounter each probe. The results are listed in Table 4. The table shows that the velocity of the front, for a given monitored density,
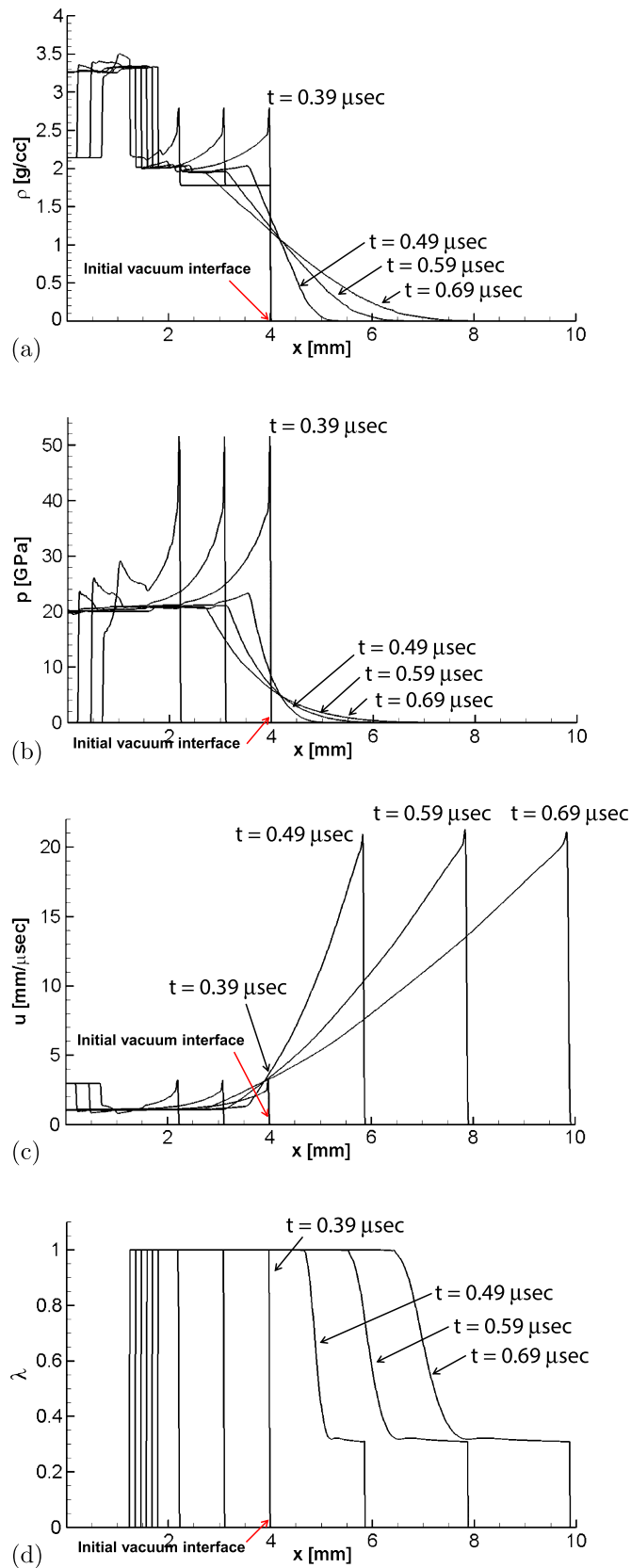
**Fig. 9.** Time sequences of detonation and expansion processes for Case I: (a) density [g/cm³], (b) pressure [GPa], (c) velocity [mm/µs], (d) reaction progress.
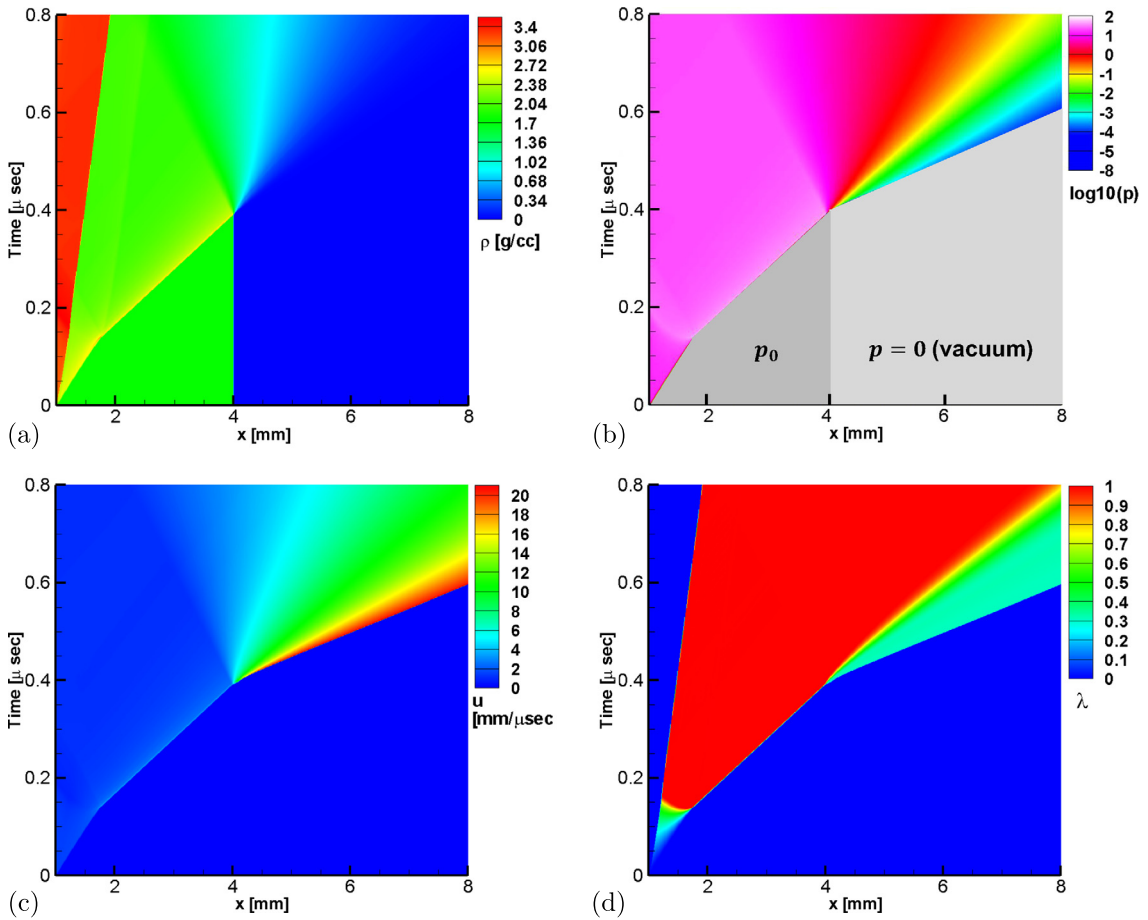
**Fig. 10.** (a) Density, (b) pressure ($\log_{10}(p)$), (c) velocity, (d) reaction progress field in space and time domain for Case I.
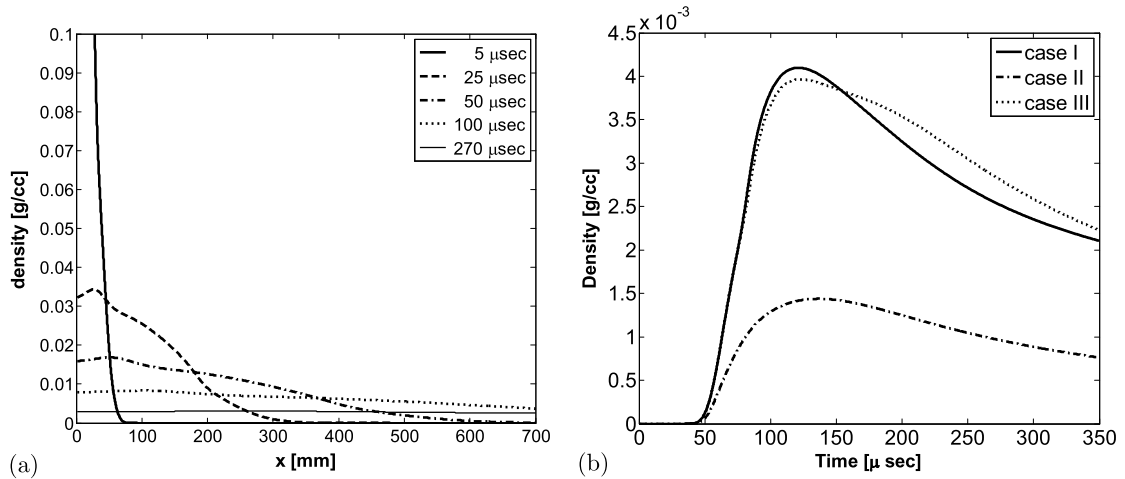


**Fig. 11.** (a) Density profile expanding toward the vacuum region, (b) monitoring density at $x = 680$ mm for the Cases I–III.

ranges from 8 to 19 mm/μs and is a function sample thickness and impact velocity. Experiments by Thomas et al. [32] showed that the detonation products expanding toward vacuum achieve terminal velocities in the range of 8 to 12 mm/μs. Fajardo et al. [33], reported the leading-edge velocities of species through the vacuum approximately ≈ 10 mm/μs in their experiments on aluminum ablation. Lundborg [34] measured the velocity of the shock front of TNT evacuating from chambers and the velocity increased from 10 mm/μs to 20 mm/μs with decreasing pressure. So our simulations easily fall in
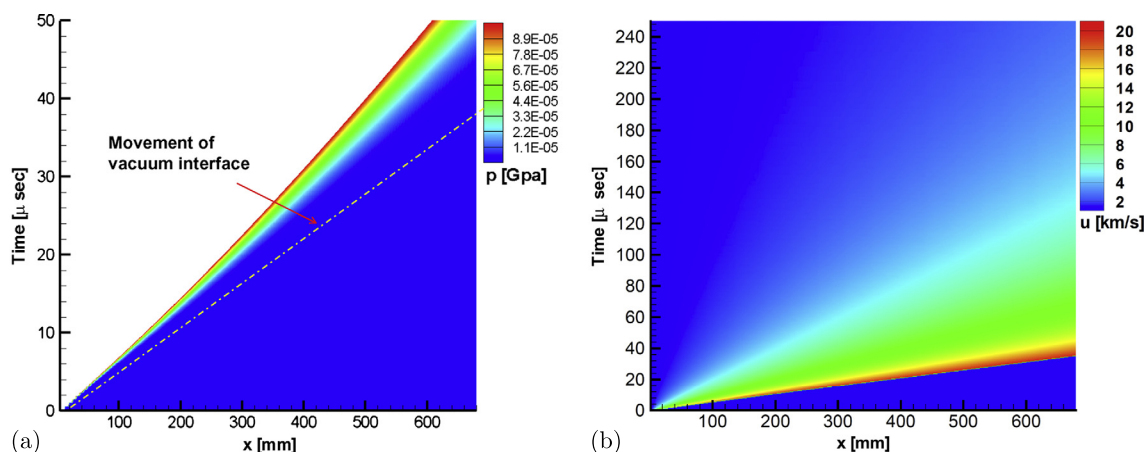
**Fig. 12.** Pressure (a) and particle velocity (b) fields for Case I in *x*–*t* domain.

the range reported in related experiments, and is a reasonable check of the applicability of these algorithms and simulation techniques for the TOFMS experiments.

### 4.3. Comparison of two different closure models that are used to define the mixture EOS

The vacuum tracking interface algorithms described in this paper can be generally used for simulating the propagation of products from the reaction of multi-component mixtures and can be modeled with any EOS that obeys the Liu–Smoller conditions for the mixture. However when a multi-component formulation is used for the mixture, one must provide some closure conditions that are in essence the statements of local equilibrium between components within the mixture. For a Gibbs formulation one posits a single pressure and temperature ($p, T$) for the mixture, denoted as (PT-EQB). This means that the component EOS forms must also share the same mixture pressure and temperature. But one can close the mathematical formulation by proposing slightly different statements. A common one is that while there a common pressure (P-EQB), the ratio of the volumes of components is either constant or is a function of the composition, in which case the component volume are not pressure dependent.

This model (P-EQB) enforces only pressure equilibrium and specifies the volume component ratios as a closure condition. It is attractive since it uses EOS forms that are linear in the pressure and the EOS forms are closed explicitly. This type of closure eliminates the need for an iterative cycle to determine the temperature, and might be considered if one has two (or multi-) temperature model for reactants and products that are in pressure equilibrium but not temperature equilibrium. However our purpose here is simply to illustrate that changing the mixture closure condition does have an effect on the simulated results, since closure really represents a different model of the mixture EOS. We note that as we changed the closure models, the qualitative features of the simulated flow are quite similar but the computed values, that are important when interpreting chemical measurements made at the probes, do change.

To examine the dependencies of the simulation results on the mixture closure models, we implemented the pressure equilibrium (P-EQB) closure for the mixture equation of state in our PETN model and carried out the simulations for Cases I and II. Comparisons of simulated results for Cases I and II, that use the two closures (PT-EQB) and (P-EQB) are shown in Figs. 14 and 15. The TOA in Fig. 14 is plotted versus the probe locations. The detection velocities of the fixed density of $10^{-8}$ g/cm$^3$ for Case I are listed in Table 5. The velocities for the two closures, range respectively from 8 to 19 mm/μs and 9 to 13.5 mm/μs.

Fig. 15 shows a comparison of the density recorded at $x = 680$ mm for the two closure models. Both models show the same tendencies and approximately the same densities, however there are noticeable differences in the time shift and peak density at a fixed monitoring point. The pressure equilibrium (P-EQB) model shows higher peak density but slower time of arrival for Cases I and II. These differences are entirely attributed to the differences in the closure models. Thus careful physical chemistry-based considerations must be taken into account to make accurate quantitative predictions for this class of simulations.

## 5. Conclusions

We have illustrated how the original Munz's vacuum tracking algorithm for a single ideal gas can be extended to a general multi-component reacting flow, with an Euler solver method that uses a linearized Riemann solver for a Mie–Gruneisen EOS form. Our implementation uses a fairly standard, cell based TVD scheme with source splitting to solve the reacting Euler equations. We have shown that for a non-ideal EOS model, our method can be implemented with different mixture closure models for pressure and temperature equilibrium, or just pressure equilibrium that uses an auxiliary condition such
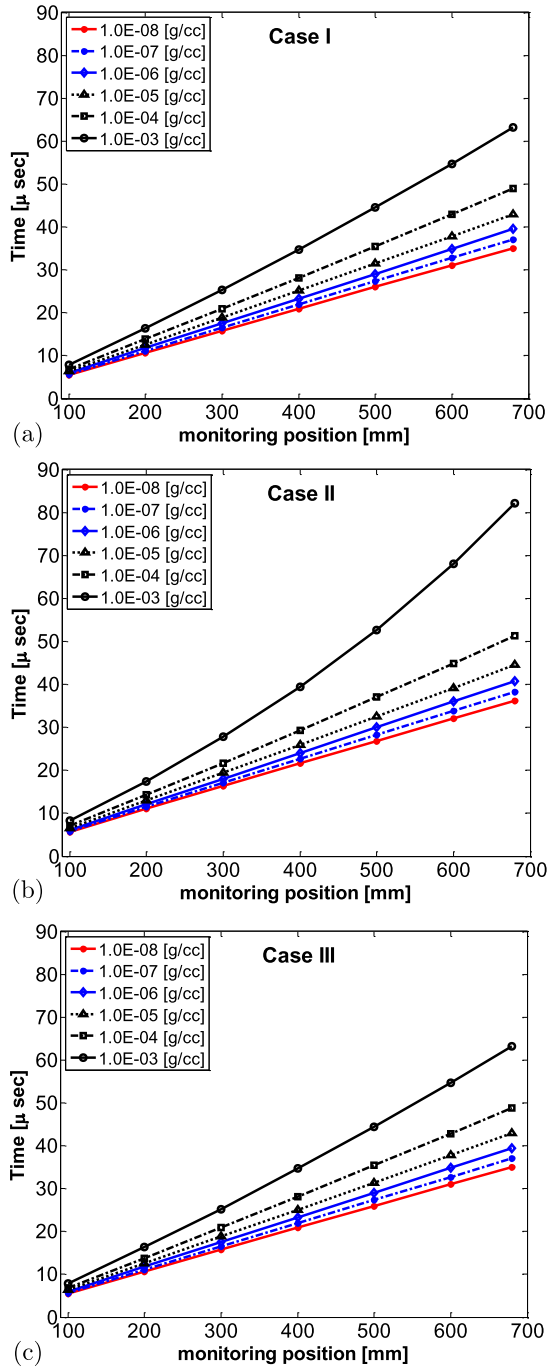
**Fig. 13.** Time of arrival of quenched products at a specified density as a function of monitoring position for (a) Case I, (b) Case II, (c) Case III.

**Table 4**
Velocity [mm/µsec] of monitored (specified) density front observed in the vacuum region for each Cases I, II and III.

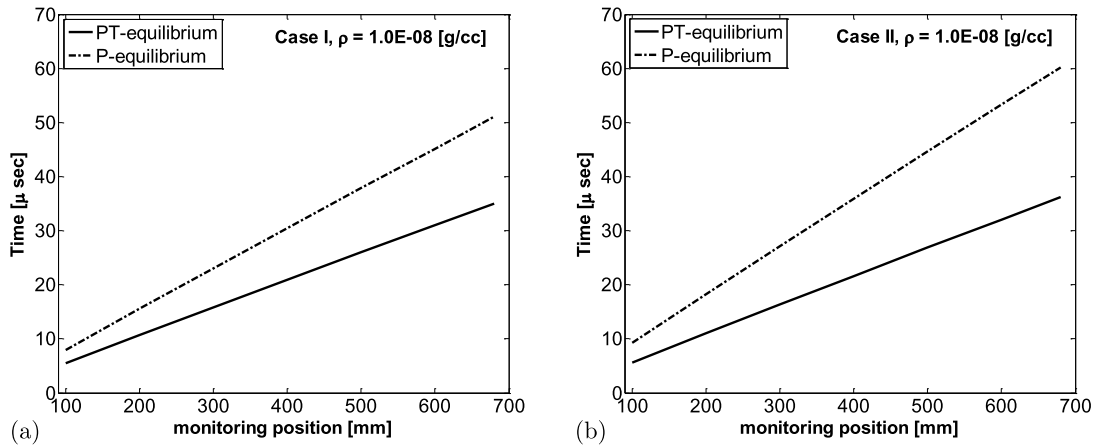| Monitoring density | Case I | Case II | Case III |
|---|---|---|---|
| $10^{-8}$ g/cm$^3$ | 19.64343 | 18.99816 | 19.67554 |
| $10^{-7}$ g/cm$^3$ | 18.46885 | 17.87125 | 18.49775 |
| $10^{-6}$ g/cm$^3$ | 17.31006 | 16.73676 | 17.34145 |
| $10^{-5}$ g/cm$^3$ | 15.81749 | 15.27493 | 15.85946 |
| $10^{-4}$ g/cm$^3$ | 13.76884 | 13.13290 | 13.82020 |
| $10^{-3}$ g/cm$^3$ | 10.50874 | 8.14376 | 10.50174 |

**Fig. 14.** Comparison of the two different closures at probe locations: Monitoring TOA of front of density $10^{-8}$ g/cm$^3$ of (a) Case I and (b) Case II.
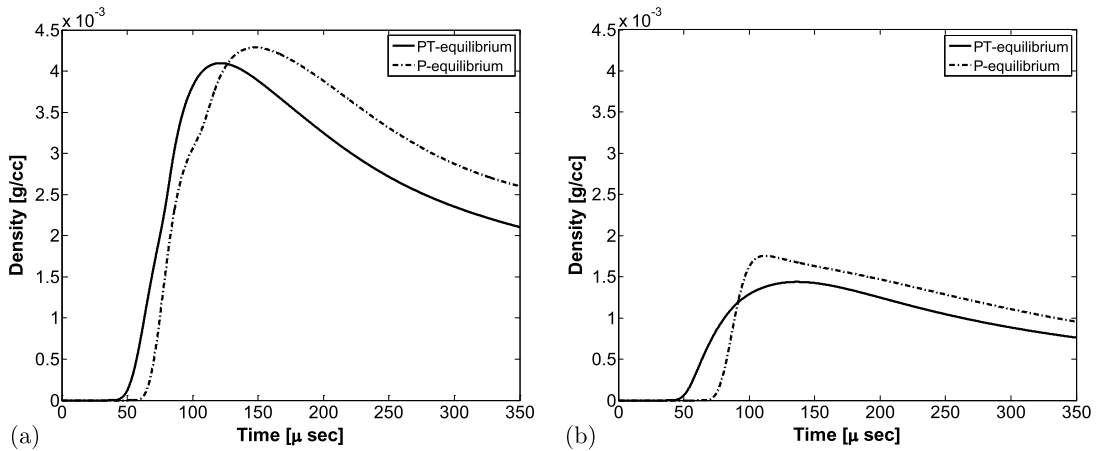


**Fig. 15.** Comparison of the two different closures: the density at $x = 680$ mm versus time for (a) Case I and (b) Case II.

**Table 5**
Comparison of the velocity determined by a monitoring density for closures, PT-EQB and PEQB [mm/µs] for Case I.

| Monitoring density | PT-Equilibrium | P-Equilibrium |
|---|---|---|
| $10^{-8}$ g/cm$^3$ | 19.64343 | 13.47709 |
| $10^{-7}$ g/cm$^3$ | 18.46885 | 12.90323 |
| $10^{-6}$ g/cm$^3$ | 17.31006 | 12.28501 |
| $10^{-5}$ g/cm$^3$ | 15.81749 | 11.54734 |
| $10^{-4}$ g/cm$^3$ | 13.76884 | 10.57082 |
| $10^{-3}$ g/cm$^3$ | 10.50874 | 8.952551 |

as a specified volume ratio to define the mixture equation of state. One must ensure that the Liu–Smoller conditions hold for the mixture EOS in the limiting case of a vacuum. The methods illustrated here are fairly robust and are easy to implement in any cell-based finite difference code framework. We feel that this is a welcome addition to a set of basic methods in an existing simulation code framework for interactions between multiple materials that are subjected to extreme pressure gradients. In cases where there is a violent expansion of material into vacuum or near vacuum regions it is essential to compute sensible and physically defined fluxes, as defined by the underlying models in order to avoid severe computational difficulties. Thus we believe the methodology presented here will have widespread applications and extensions to a much larger class of problems.

## Acknowledgements

## References

[1] C.D. Munz, A tracking method for gas flow into vacuum based on the vacuum Riemann problem, Math. Methods Appl. Sci. 17 (8) (1994) 597–612.
[2] E. Fossum, C. Molek, W. Lewis, M. Fajardo, Benchtop energetics: detection of hyperthermal species, Bull. Am. Phys. Soc. 56 (2011).
[3] N.C. Blais, H.A. Fry, N.R. Greiner, Apparatus for the mass spectrometric analysis of detonation products quenched by adiabatic free expansion, Rev. Sci. Instrum. 64 (1) (1993) 174–183.
[4] B.J. Lee, E.F. Toro, C.E. Castro, N. Nikiforakis, Adaptive Osher-type scheme for the Euler equations with highly nonlinear equations of state, J. Comput. Phys. 264 (2013) 165–183.
[5] P. Glaister, An approximate linearised Riemann solver for the Euler equations for real gases, J. Comput. Phys. 74 (2) (1988) 382–408.
[6] S. Xu, Modeling and numerical simulation of deflagration-to-detonation transition in porous energetic materials, PhD dissertation, Theoretical and Applied Mechanics, University of Illinois, 1996.
[7] S. Xu, T. Aslam, D.S. Stewart, High resolution numerical simulation of ideal and non-ideal compressible reacting flows with embedded internal boundaries, Combust. Theory Model. 1 (1997) 113–142.
[8] E.F. Toro, Riemann Solvers and Numerical Methods for Fluid Dynamics: A Practical Introduction, Springer-Verlag, 2009.
[9] P. Colella, A. Majda, V. Roytburd, Theoretical and numerical structure for reacting shock waves, Shock Waves 7 (4) (1986).
[10] T. Liu, J. Smoller, On the vacuum state for the isentropic gas dynamics equations, Adv. Appl. Math. 1 (1980) 345–359.
[11] H.B. Callen, Thermodynamics and an Introduction to Thermostatistics, John Wiley & Sons, New York, 1985.
[12] W. Fickett, W.C. Davis, Detonation: Theory and Experiment, Dover Pubns, 2011.
[13] L.E. Fried, W.M. Howard, P.C. Souers, P.A. Vitello, Cheetah 6.0 User Manual, LLNL-SM-416166 Lawrence Livermore National Laboratory, Livermore, CA, 2010.
[14] E.L. Lee, C.M. Tarver, Phenomenological model of shock initiation in heterogeneous explosives, Phys. Fluids (1958–1988) 23 (12) (2008) 2362–2372.
[15] A.C. Hindmarsh, Lsode and lsodi, two new initial value ordinary differential equation solvers, ACM Signum Newslett. 15 (4) (1980) 10–11.
[16] A. Harten, B. Engquist, S. Osher, S.R. Chakravarthy, Uniformly high order accurate essentially non-oscillatory schemes. III, J. Comput. Phys. 71 (2) (1987) 231–303.
[17] H. Deconinck, T.J. Barth, High-Order Methods for Computational Physics, vol. 9, Springer-Verlag, 1999.
[18] X.D. Liu, S. Osher, T. Chan, Weighted essentially non-oscillatory schemes, J. Comput. Phys. 115 (1) (1994) 200–212.
[19] P.L. Roe, The use of the Riemann problem in finite difference schemes, in: Seventh International Conference on Numerical Methods in Fluid Dynamics, Springer, 1981, pp. 354–359.
[20] P.L. Roe, Approximate Riemann solvers, parameter vectors, and difference schemes, J. Comput. Phys. 43 (2) (1981) 357–372.
[21] E. Halter, E. Martensen, A fast solver for Riemann problems, Math. Methods Appl. Sci. 7 (1) (1985) 101–107.
[22] R. Menikoff, Complete Mie–Gruneisen equation of state, Los Alamos Technical Report LA-UR-12-22592, Los Alamos National Laboratory, May 2012.
[23] D.S. Stewart, S. Yoo, W.C. Davis, Equation of state for modeling the detonation reaction zone, in: 12th Symp. (Intl.) on Detonation, 2002, pp. 1–11.
[24] W. Romberg, Vereinfachte numerische integration, Det Kong. Norsk. Vidensk. Selsk. Forhandl. 28 (7) (1955) 30–36.
[25] W.L. Ng, J.E. Field, H.M. Hauser, Thermal, fracture, and laser-induced decomposition of pentaerythritol tetranitrate, J. Appl. Phys. 59 (12) (1986) 3945–3952.
[26] C.M. Tarver, R.D. Breithaupt, J.W. Kury, Detonation waves in pentaerythritol tetranitrate, J. Appl. Phys. 81 (11) (1997) 7193–7202.
[27] D. Stirpe, J.O. Johnson, J. Wackerle, Shock initiation of XTX-8003 and pressed PETN, J. Appl. Phys. 41 (9) (Aug. 1970) 3884–3893.
[28] V.I. Korepanov, V.M. Lisitsyn, V.I. Oleshko, V.P. Tsypilev, PETN detonation initiated by a high-power electron beam, Tech. Phys. Lett. 29 (2003) 669–671.
[29] J.B. Bdzil, D.S. Stewart, The dynamics of detonation in explosive systems*, Annu. Rev. Fluid Mech. 39 (2007) 263–292.
[30] J.B. Bdzil, D.S. Stewart, Theory of detonation shock dynamics, in: Shock Waves Science and Technology Library, vol. 6, 2012, pp. 373–453.
[31] D.S. Stewart, S. Yoo, B.L. Wescott, High-order numerical simulation and modelling of the interaction of energetic and inert materials, Combust. Theory Model. 11 (2) (2007) 305–332.
[32] R.L. Kovach, T.J. Ahrens, C.F. Allen, Explosive gas blast: the expansion of detonation products in vacuum, J. Appl. Phys. 42 (2) (1971) 815–829.
[33] M. Fajardo, E.C. Fossum, C.D. Molek, W.K. Lewis, Benchtop energetics progress, AIP Conf. Proc. 1426 (1) (2012) 217–222.
[34] N. Lundborg, Front and mass velocity at detonation in evacuated chambers, Ark. Fys. 25 (6) (1964) 541.

**DEPARTMENT OF DEFENSE**


DEFENSE THREAT REDUCTION
AGENCY
8725 JOHN J. KINGMAN ROAD
STOP 6201
FORT BELVOIR, VA 22060
    ATTN: A. DALTON

DEFENSE TECHNICAL
INFORMATION CENTER
8725 JOHN J. KINGMAN ROAD,
SUITE 0944
FT. BELVOIR, VA  22060-6201
    ATTN: DTIC/OCA

**DEPARTMENT OF DEFENSE**
**CONTRACTORS**

QUANTERION SOLUTIONS, INC.
1680 TEXAS STREET, SE
KIRTLAND AFB, NM  87117-5669
    ATTN: DTRIAC